GSK3b in brain metabolism and aging

By

Dylan C. Souder

A dissertation submitted in partial fulfillment of

the requirements for the degree of

Doctor of Philosophy

(Nutritional Sciences)

at the

UNIVERSITY OF WISCONSIN-MADISON

2020

Date of final oral examination: August 7th, 2020

The dissertation is approved by the following members of the Final Oral Committee:

Rozalyn M. Anderson, Associate Professor, Medicine
Luigi Puglielli, Professor, Medicine
Brian Parks, Assistant Professor, Nutritional Sciences
Barbara Bendlin, Associate Professor, Medicine
Richard Eisenstein, Professor, Nutritional Sciences

ACKNOWLEDGEMENTS

I'd like to start by thanking my advisor Dr. Rozalyn Anderson. She has been incredibly invested in my success as a scientist, which is the best attribute I could hope for in an advisor. Her mentorship has allowed me to grow creatively and intellectually in my path as a researcher, and her enthusiasm for my projects played a huge role in my graduate school success.

Thank you to my thesis committee: Drs. Luigi Puglielli, Barb Bendlin, Rick Eisenstein, and Brian Parks. Their insights and expertise have allowed me to think about my research from multiple perspectives. This has improved the breadth of my work, and contributed to my development as a well-rounded scientist.

I'd specifically like to thank some past and present lab members: Steve Martin for his patience in guiding me when I first joined the lab. Karl Miller and Porsha Howell for serving as outstanding examples of successful and productive graduate students. Josef Clark and Tim Rhoads for contributing their time and expertise towards the completion of my projects.

Thank you to the undergraduate students who contributed both directly and indirectly to my research. I've gained valuable experience as a mentor working with all of you. Especially Izzy Dreischmeier, whose competence and skill greatly contributed to my productivity.

Finally, I'd like to thank my friends and family for their support over the years. Whether it was running the Glacial Drumlin trail, hanging out at the terrace, or visiting some of you across the country for much-needed vacation time, my graduate school experience was made all the better with you in my life.

GSK3b in brain metabolism and aging

Dylan C Souder

Under the supervision of Dr. Rozalyn M Anderson

at the University of Wisconsin-Madison

ABSTRACT

Aging has emerged as the greatest risk factor for a wide range of chronic diseases. One of the main objectives of aging biology research is to identify the common mechanisms of these diseases so that the underlying vulnerability can be targeted. Caloric restriction (CR) is the most robust and reproducible intervention to extend lifespan and delay the incidence of disease in diverse organisms. Importantly, growth-repression and reprogramming of mitochondrial metabolism are conserved features of the response to CR that are shared among tissues and conserved among species, and are likely involved mechanistically in the longevity-promoting effect of the intervention. Glycogen synthase-kinase 3-beta (GSK3b) is a growth-sensitive kinase that has been implicated in brain aging and CR. Evidence from cell culture studies places GSK3b upstream of the key mitochondrial regulator, peroxisome proliferation-activated receptor gamma coactivator 1 alpha (PGC1a); however, it is unclear if GSK3b regulates mitochondrial metabolism and PGC1a in the diverse cell populations of the central nervous system. Work in this thesis demonstrates that GSK3b inhibition increases mitochondrial function in neurons and glia by a mechanism linked to PGC1a stability and activity. The ability of GSK3b to influence metabolism was conserved in the brains of mice treated with the GSK3b-inhibitor lithium. Moreover, we show that age-related increases in GSK3b protein are associated with metabolic and growth pathway alterations, consistent with a role for GSK3b in the metabolism of the aging brain. We define the mechanisms of PGC1a upregulation by lithium in cultured neurons, and characterize the expression and differential regulation of a neuron-specific PGC1a transcript variant. Finally, we show

amyloid plaque-associated changes in mitochondrial function as a potential contributor to Alzheimer's disease (AD) that is conserved from transgenic mice to aged monkeys and humans. This body of work demonstrates that mitochondrial metabolism is regulated by GSK3b in the central nervous system, and that a change in metabolism is a shared feature of brain aging and AD neuropathology. We conclude that GSK3b is a key factor in shaping metabolic adaptation in the brain, that it contributes to age-related changes in brain metabolism, and may even be involved in creating disease vulnerability in the aging brain.

TABLE OF CONTENTS **PAGE**

LIST OF FIGURES **PAGE**

Chapter 1: An expanding GSK3 network: implications for aging research

Taken from the following published works:

An expanding GSK3 network: implications for aging research
Dylan C Souder, Rozalyn M Anderson
Geroscience. 2019 Aug;41(4):369-382

ABSTRACT

The last few decades of longevity research have been very exciting. We now know that longevity and health-span can be manipulated across species, from unicellular eukaryotes to nonhuman primates, and that while aging itself is inevitable, how we age is malleable. Numerous dietary, genetic, and pharmacological studies now point to links between metabolism and growth regulation as a central aspect in determining longevity and, perhaps more importantly, health with advancing age. Here, we focus on a relatively new player in aging studies GSK3, glycogen synthase kinase, a key factor in growth and metabolism whose name fails to convey the extensive breadth of its role in cellular adaptation. First, we provide a brief overview of GSK3, touching on those aspects that are likely relevant to aging. Then, we outline the role of GSK3 in cellular functions including growth signaling, cell fate, and metabolism. Next, we describe evidence demonstrating a direct role for GSK3 in a range of age-related diseases, despite the fact that they differ considerably in their etiology and pathology. Finally, we discuss the role that GSK3 may play in normative aging and how GSK3 might be a suitable target to oppose age-related disease vulnerability.

INTRODUCTION

Aging is the greatest risk factor for a range of chronic diseases and disorders including cancer, diabetes, and neurodegenerative disease, and significant effort is being invested to identify casual aspects in morbidity and loss of resilience as a function of age [1]. Dietary excess and a sedentary lifestyle appear to increase vulnerability to diseases and disorders traditionally viewed as age-related [2], potentially linking the pace of aging to metabolic dysfunction. Caloric restriction (CR) without malnutrition prolongs lifespan and health-span in a wide range of species including non-human primates, and although the mechanisms yet to be established, a growing literature points to a central role for metabolism in the beneficial effects of CR [3]. A prevailing theme in genetic studies of aging is that repression of growth and growth signaling is also strongly linked to longevity [4]. Evidence from yeast, worms, flies, and rodents links lifespan extension to insulin and IGF-1 signaling pathway components [5]. Pathways regulating growth signaling and metabolism are known to be highly interconnected, raising the possibility that this integrated network is what is intrinsically linked to the increase in disease vulnerability that accompanies age. Factors that coordinate growth signaling and metabolism are strong candidates as targets in the treatment of age-related diseases and in development of preventative interventions to prolong good health with advancing age. One such effector of growth signaling is glycogen synthase-kinase 3 (GSK3), a broad specificity serine-threonine kinase that has been linked to insulin resistance, systemic inflammation, and several aspects of Alzheimer's disease (AD) pathology [6].

There are two isoforms of GSK3 enzyme, GSK3a and GSK3b, collectively referred to as GSK. The genes encoding these two isoforms reside on separate chromosomes and are ubiquitously expressed [7]. Loss of function mutants have revealed that they have partially overlapping functions; GSK3a knockout (KO) mice are viable due to compensatory activity from GSK3b, but GSK3b KO is embryonically lethal [8-10]. Genetic studies place GSK3 as a critical regulator of growth and development that also impinges on metabolic homeostatic mechanisms (Table 1.1). GSK3 is

constitutively active and can be inhibited through phosphorylation or by sequestration in a cytosolic complex that includes beta catenin [11,12]. Signaling through insulin and WNT pathways appears to regulate distinct pools of GSK3 (Fig.1.1): AKT activation leads to GSK phosphorylation and inhibition but does not affect beta catenin, while WNT causes dislocation of GSK3 from its beta catenin targeting destruction complex, leading to stabilized and active beta catenin [13]. Despite these differences in mechanistic detail, both WNT and insulin pathways share GSK3b as an effector in signaling and both converge on cell growth and metabolism. Over 70 GSK3 substrates have been validated, representing diverse roles in cellular function. Many GSK3b targets have established relevance to aging, including PI3K, mTOR complex 1 (mTORC1), AMP kinase (AMPK), and peroxisome proliferator-activated receptor gamma co-activator 1alpha (PGC1a), among others. This breadth of influence implies that GSK3 may be a central coordinator of the cellular response to growth stimulus or repression [14]. Genetic studies have revealed general details of GSK3 function at the cellular level, including signaling downstream of growth and inflammation, and modulation of cell cycle [15,16]. GSK3b in particular is enriched in the brain where it has brain-specific roles and is required for neurogenesis, regulation of synaptic plasticity, and neurotransmission [6]. These aspects of GSK3b have been particularly well studied in the context of psychiatric disorders, where the GSK3b inhibitor lithium has been used for over a century as a mood stabilizing agent [17]. Intriguingly, GSK3b has also been identified as a major tau kinase implicated in the formation of neurofibrillary tangles, making it a potential target for AD therapeutics [18]. As outlined below, recent evidence implicates GSK3b in models of delayed and accelerated aging, and interesting new roles for GSK3b in cellular function have been discovered. The goal of this review is to shed light on GSK3b as a factor that links metabolism and growth signaling, and to discuss how it might play a role in aging as a driver of age-related pathology.

LITERATURE REVIEW

GSK3 and Cell Signaling

Upstream mechanisms controlling GSK3 activity, including protein complex formation, sequestration, and autoregulation, have been thoroughly reviewed elsewhere [6]. Briefly, inhibitory phosphorylation of GSK3b occurs at the serine-9 position in response to growth stimulus, subsequently impacting GSK3 target proteins involved in glycogen synthesis, translation, and cell survival [19,20]. Many GSK3 substrates require priming phosphorylation four residues C-terminal to the GSK3 consensus site (S/TXXXS/T) and serine-9 phosphorylation of GSK3 only prevents the binding of the kinase to primed substrates [20]. Both AKT and S6K have been shown to phosphorylate GSK3b at the serine 9 site (serine X in SK3a) in response to growth signaling, while phosphatases including PP2A result in de-phosphorylation at this site [11,19,21]. Interestingly PI3K and mTOR Complex 1 are key nodes that regulate longevity, and significant cross-talk between these pathways has been heavily implicated in upstream regulation of GSK3 activity [22]. More recent evidence also places both mTOR Complex 1 and PI3K signaling downstream of GSK3, revealing a complex network of signals that impacts cellular function and health [23].

GSK3 phosphorylates and activates TSC2 resulting in inhibition of the GTPase Rheb with subsequent inhibition of the mTOR Complex 1 pathway. Interestingly, expression of TSC2 lacking the GSK3b phosphorylation sites resulted in persistent activation of mTOR Complex 1 and apoptosis in response to nutrient deprivation [24]. This potentially places GSK3b upstream of other mTORC1 functions, including lipid and protein biosynthesis, nucleotide metabolism, and glycolysis; however, the role of GSK3 in controlling cell activity at the functional level has not been very well defined. Glucose uptake and coincident GLUT1 expression is increased in response to GSK3 inhibition in vascular smooth muscle [25]. Translation is reportedly blocked by GSK3b activity, but it is unclear whether this effect is mediated by mTOR Complex 1 inhibition or by direct phosphory-

lation of eIF2B, another GSK3b substrate [26]. More recently, GSK3 has been implicated as a negative regulator of mTOR Complex 2 function, where the Complex 2 binding partner Rictor was identified as a GSK3 substrate that is subsequently targeted for proteasomal degradation [27]. GSK3 itself has also been implicated as a target downstream of mTOR Complex 1. TSC2 deficiency in cells results in persistent S6K dependent inhibition of GSK3b, although this regulatory mechanism may only be relevant in the context of insulin resistance, since in these cells signaling through insulin pathways was blunted and AKT, the usual dominant kinase for GSK3, was inhibited [28]. Altogether, these complex interactions with insulin and mTOR demonstrate that GSK3b is important in redirecting cellular growth and synthetic pathways in response to changes in nutrient availability (Fig.1.1).

In addition to controlling aspects of mTOR signaling GSK3 has multiple interactions within the insulin/IGF1 signaling pathway. Although GSK3 is canonically inhibited through insulin signaling, it also exerts feedback control on this pathway. GSK3 was shown to phosphorylate IRS-1 and suppress insulin signaling activity in cells [29]. Inhibitory phosphorylation by GSK3 has also been extended to IRS-2 in the stress response [30]. In another study, GSK3 was found to target IRS-1 for proteasomal degradation under conditions of insulin resistance, demonstrating that GSK3 controls both the stability and activity of this protein [31] (Fig.1.2). The stability of the insulin-signaling antagonist PTEN is also regulated by GSK3 phosphorylation, although the functional consequences of this interaction are unclear [32]. These data collectively implicate GSK3 as a regulator of insulin sensitivity that may be mechanistically important in conditions such as type 2 diabetes. This concept is supported by data showing that GSK3 can impact key aspects of glucoregulatory health and is discussed in more detail below.

GSK3 and Cell Fate

Downstream of its involvement in growth and nutrient signaling, GSK3b directly impacts cell survival and proliferation (Fig.1.3). Early work demonstrated that GSK3b activation was necessary for growth-factor withdrawal induced apoptosis, and has since been extended to a wide

variety of toxicities, including oxidative stress, ER stress, and neuronal excitotoxicity [33]. MCL-1 (myeloid leukemia cell differentiation protein) is targeted for degradation by GSK3b in response to both inflammatory stimuli and growth factor withdrawal, resulting in activation of the intrinsic apoptotic pathway [34]. GSK3 additionally phosphorylates VDAC1, which blocks its interaction with hexokinase II. The loss of interaction disrupts mitochondrial localization and anti-apoptotic function of hexokinase II and increases the vulnerability of cells to apoptosis [35]. It was subsequently shown that GSK3 is a positive regulator of the mitochondrial permeability transition pore (mPTP). GSK3b association with VDAC2 is necessary for maximal permeability of the mPTP under conditions of oxidative stress [36]. Intriguingly, GSK3b also upregulates activity of the tumor suppressor TP53, resulting in cell cycle arrest and apoptosis [37]. In contrast to the pro-apoptotic effects of GSK3b activity, GSK3b inhibition through WNT and growth signaling promotes cell survival and proliferation. The effect of GSK3b on cell proliferation has been demonstrated in stem cells, where inhibition of GSK3b promotes self-renewal and blocks differentiation [38]. Deletion of both GSK3a and GSK3b in neural progenitor cells resulted in a massive expansion of progenitor cells; however, these progenitors showed compromised differentiation. GSK3 directed deregulation of stem cells was linked to beta-catenin, although stabilization of c-myc and c-jun that are also direct substrates of GSK3 could reasonably play a role too [14]. Expression of constitutively active GSK3 mutants resistant to N-terminal phosphorylation (mutated at S21A and S9A for GSK3a and GSK3b respectively), results in blockage of neural precursor cell proliferation [39]. The ability of GSK3 to control cell fate has significant implications for the aging field: stem cell and progenitor cell renewal declines with age resulting in a diminished capacity of tissues to regenerate [40]. Taken together, these multiple interactions ensure that GSK3b can rapidly induce changes in cell survival in response to extracellular stimuli or when conditions are appropriate can stimulate renewal through stem cell recruitment. Therapeutic inhibition of GSK3 has the potential to counteract age-related decline in cellular renewal and stem cell recruitment; however, given the role of GSK3 in

the balance of growth and cell survival, the risks of such a therapy would need to be thoroughly evaluated.

GSK3 and Inflammation

Chronic inflammation increases with age and growth signaling pathways intersect with inflammation through GSK3. The regulation of inflammation by GSK3 is best characterized through its differential control of CREB and NF-kB transcriptional activity (Fig.1.4). GSK3 is required for the integrity of Toll-like receptor (TLR) signaling [41]. Downstream of TLR activation, the status of GSK3 tips the balance between pro- and anti-inflammatory cytokine production. GSK3 activity is required for production of pro-inflammatory IL-6, IL-1B, and IFNy following TLR stimulation, and inhibition of GSK3 during TLR activation favors IL-10 production. Mechanistically these outcomes are linked to increased nuclear CREB activity and lower NFkB activity in GSK3 inhibited TLR activated monocytes, where CREB competes and sequesters CPB, a binding partner it shares with NFkB. Inhibition of GSK3 with lithium has also been shown to elevate CREB activity in neuronal cells [42], supporting a model of GSK3 as a regulator of neuroinflammation. This concept is supported by in-vivo evidence showing that adult onset neuron-specific overexpression of GSK3b (CamKII Tet) induces astrogliosis. Intriguingly, this effect appears to be cell non-autonomous as glia do not express the transgene [43](Table 1.1). Both CREB and NFkB have been identified as direct substrates of GSK3b. Phosphorylation of CREB occurs after priming phosphorylation by PKA, preventing CREB DNA binding and activity thus ensuring that CREB activity is temporally controlled [42,44]. NEMO is an indirect NFkB regulator that along with IKK targets NFkB inhibitor IkB for proteasomal degradation. NEMO interacts with and is phosphorylated by GSK3b at multiple sites resulting in its stabilization [45]. Importantly, neuroinflammation has been linked to peripheral metabolic dysfunction in mice [46], and it is not unreasonable to think it could also contribute to pathological aging through this same IKK/NFkB axis. Cross-talk between growth and inflammation has been established in Th17 cells through GSK3a. Here, IKK is activated in response to IL-1 signaling resulting in GSK3a inhibition and stimulation of AKT-mTORC1 [47], linking

GSK3 to regulation of adaptive immunity. The importance of GSK3 in mediating the inflammatory response is underscored by the effectiveness of GSK3 inhibitors in treating inflammation. Administration of a GSK3 inhibitor prevented the death of mice resulting from a lethal dose (LD_{100}) of lipopolysaccharide [41]. Elsewhere, GSK3b plays a pro-inflammatory role in mouse models of arthritis and peritonitis [48]. Here too GSK3 resides at the intersection of pro-and anti-inflammatory cytokine production and mediates cross-talk between Interferon gamma (IFNg) and TLR signaling. These studies suggest that GSK3 inhibitors could be therapeutically useful in the treatment of inflammatory diseases. In mouse models of accelerated aging, the observed increased inflammation is associated with activation of NEMO [49]. Indeed, aging is associated with low-grade sterile inflammation [50], that includes elevated pro-inflammatory cytokines in the serum, activation of NF-kB signaling, and increased expression of immune and inflammation related genes [51]. Aging studies investigating the impact of long-term GSK3 inhibition are needed to clarify whether targeting GSK3 could be useful in attenuating age-related increases in inflammation.

GSK3 and Cellular Senescence

Another age-related phenomenon linked to GSK3 is cellular senescence, a state of permanent cell cycle arrest caused by diverse adverse signals, including contact inhibition, genotoxic injury, and mitochondrial stress [52,53]. Transplantation of senescent cells into mice resulted in aging pathology, while removal of these cells pharmacologically alleviated symptoms suggesting that cell senescence directly contributes to the aging process [54]. N-terminal phosphorylation of both GSK3 isoforms is reported to accompany hepatocyte senescence and treatment with lithium was sufficient to induce a senescent phenotype that is coincident with augmented anabolism including protein synthesis and glycogenesis [55]. GSK3b was shown to accumulate in the nucleus of human fibroblasts that had undergone replicative senescence, where it formed a stable complex with p53 [56]. Intriguingly, treatment of these cells with lithium blocked the interaction of GSK3b with p53 and caused cells to enter a reversible quiescent state. Thus, it appears GSK3 could both promote and oppose cellular senescence under different circumstances. The role of mitochondrial metabolism

in cellular senescence has yet to be fully resolved. Mitochondrial dysfunction has been associated with senescence and is detected in senescent cells; however, mitochondrial dysfunction has also been identified as a causal agent in senescence [57]. Growing evidence shows a role for cellular senescence and the senescence associated secretory phenotype in promoting aging phenotypes [58]. GSK3, residing as it does at the intersection of growth and metabolism, is likely to be important in senescence and may even contribute senescent cell accumulation as a function of age.

GSK3 and energy metabolism

Growth signaling was one of the first pathways to be associated with longevity and the impact of growth inhibition in enhancing longevity been consistently observed among species [5]. Extended lifespan has been shown in several genetic mouse models of somatotropic axis deficiency [4], and blunted growth is a hallmark of CR and is thought to partially mediate its benefits [59]. Growth inhibition with CR is accompanied by a modest but consistent upregulation of mitochondrial energy metabolism pathways. Intriguingly this effect is highly conserved across multiple tissues in mice, and among species on CR, suggesting that it is fundamental to the CR response [60]. An important question is how cross-talk between growth and metabolic pathways might mediate the effects of CR to delay aging and the onset of age-related disease. As a key effector of growth signaling, GSK3 is perfectly positioned as a regulator of this cross-talk and recent studies have explored the role of both GSK3 isoforms in controlling key metabolic proteins, intermediary metabolism, and mitochondrial function, as outlined below.

AMPK is a major player in regulating cellular energetics [61]. GSK3b phosphorylation inhibits AMPK activity by making the activation loop site more vulnerable to inhibitory phosphatases [62]. Ablation of the GSK3b site on AMPK in cells resulted in constitutive autophagy and inability to respond to anabolic conditions. Interestingly, GSK3b phosphorylation of AMPK requires a priming phosphorylation by AKT indicating that GSK3b may play a role in fine-tuning the balance of anabolism and catabolism to energetic status. Control over AMPK raises the possibility that GSK3 could be a negative regulator of mitochondrial energy production. GSK3 has previously been

shown to inhibit the activity of pyruvate dehydrogenase, which may attenuate mitochondrial activity [63]. A more direct relationship between GSK3 and mitochondria has been established through Drp1, which promotes mitochondrial fission [64]. Phosphorylation of Drp1 by GSK3 promoted elongated mitochondrial morphology, while inhibition with lithium resulted in more fragmented mitochondria. The ability of GSK3 to regulate mitochondria through PGC1a, a transcriptional co-activator and master regulator of mitochondrial function has also been reported [65], where GSK3b was shown to target PGC1a for nuclear proteasomal degradation (Fig.1.5). Another study in primary neurons demonstrated that GSK3b phosphorylation of PGC1a at T-295 was required for recognition by an E3 ubiquitin ligase [66]. Several additional questions surrounding this regulation remain, including the identity of the kinase that primes PGC1a for GSK3b targeting. In liver, GSK3b phosphorylates PPARa at serine 73, resulting in ubiquitination and proteasomal degradation. Inhibition of GSK3b was associated with attenuated hepatic steatosis in high fat diet fed mice, highlighting an important connection between GSK3b and metabolic disease [67].

GSK3 and Age-related Disease

Changes in GSK3 expression and function are strongly related to numerous diseases and disorders that share an increase in risk of incidence as a function of age. Among these are type 2 diabetes, cancer, inflammatory conditions, and Alzheimer's disease [6]. There is a substantial volume of research published on each of these chronic conditions and the role of GSK3 in each is rather scattered about the literature. Here we will briefly describe some of the studies that favor a role for GSK3 in progression of age-related diseases and suggest that GSK3 could be an agent in creating age-related disease vulnerability in the first place.

Diabetes: GSK3b expression levels have been found to correlate positively with glucoregulatory dysfunction in diabetes patients [68]. The significance of this association is unclear; however, genetic studies have revealed that GSK3 is a powerful mediator of systemic glucose and lipid homeostasis and that these actions have a high degree of tissue specificity (Table 1.1). The whole-

body GSK3b KO is embryonic lethal but the whole-body GSK3a KO mice display improved glucoregulatory function early in life [10]. Skeletal muscle specific GSK3b overexpression resulted in hyperlipidemia, elevated fasting insulin, and glucose intolerance in male mice [69]. Conversely, mice lacking GSK3b in skeletal muscle exhibit improved glucose tolerance and greater insulin-stimulated glycogen synthase regulation [70]. Liver-specific deletion of GSK3b did not exhibit an overt phenotype, indicating that the glucoregulatory role of GSK3 appears to be primarily extra-hepatic [70]. It seems likely that at least some phenotypes of GSK3 overexpression are linked to its role downstream of insulin and mTOR signaling. Double knock-in mice expressing AKT insensitive GSK3a and GSK3b were resistant to high fat diet induced obesity, dyslipidemia, and glucoregulatory impairment [71]. These mice also showed greater circulating levels of adiponectin, the adipose-tissue derived endocrine factor that signals through AMPK. Likely linked to the increase in adiponectin, the mice also showed an increase in energy expenditure. Further evidence suggests that GSK3 could be important for pancreatic endocrine function. Beta cell-specific expression of a constitutively active GSK3b transgene (GSK3b S9A) resulted in a reduction in beta cell mass and function [72]. Conversely, GSK3b deletion conferred resistance to high fat diet induced diabetes and resulted in beta cell expansion in mice [73]. Small-molecule inhibitors of GSK3 increased the replication of beta cells from isolated rat islets, suggesting that targeting GSK3 may have therapeutic value [74].These data show that GSK3 can impact multiple aspects of the metabolic syndrome, including insulin sensitivity, glucose clearance and storage, and lipid homeostasis. These studies highlight the distinction that needs to be made in terms of GSK3 protein levels and phosphorylation status, tissue specificity in GSK3 actions, and how its sensitivity to different signaling inputs not only allows for distinct outcomes of its activation but also means that context must be considered if GSK3 is to be a druggable target for metabolic dysfunction.

Alzheimer's disease: The role of GSK3 as a mediator of Alzheimer's disease pathology has been investigated for a few decades. GSK3a and GSK3b isoforms can each phosphorylate residues

on tau *in vitro* [18]; however, GSK3b but not GSK3a has been shown to co-localize with neurofibrillary tangles (NFTs) and active but not inactive (phosphorylated at S9) GSK3b was found in neurons in the early stages of tangle formation, suggesting that kinase active GSK3b is involved in the pathogenesis of NFTs [75,76]. This is supported by genetic evidence showing that neuron-specific overexpression of GSK3b in mice resulted in hyperphosphorylation of tau on residues that lead to paired helical filament formation [43]. GSK3 has also been connected to amyloid plaque pathology. Lithium treatment blunted processing and secretion of amyloid precursor protein (APP) peptide fragments from cells and lowered levels of A-beta in the brains of a genetic model of Alzheimer's disease [77]. In cells, the effect of lithium to promote amyloid secretion was attributed to GSK3a, but not GSK3b. This finding is supported by in-vivo evidence showing that GSK3a, but not GSK3b, knock-down ameliorates amyloid plaque load in a mouse model of Alzheimer's disease [78]. This same study demonstrated that knock-down of both GSK3 isoforms reduced tau phosphorylation, misfolding, and memory deficit. GSK3 has also been implicated as a mediator of neuroinflammation, neuritic damage, and learning and memory deficits [43,79]. Mice with induced overexpression of GSK3b exhibit phosphorylation and mislocalization of tau, along with increased nuclear beta-catenin. These cellular phenotypes were associated with cognitive impairments and astrogliosis even in the absence of NFT deposition. GSK3b associated neuronal apoptosis, decreased brain volume, and impairment in learning and memory were completely reversible after 6-weeks of transgene silencing, pointing to a direct role of GSK3 in producing Alzheimer's disease related traits [80]. Additional studies have established that GSK3b promotes long term depression and inhibits long term potentiation, further connecting GSK3 to memory impairment [81]. More recently, GSK3 was shown to be activated in mouse models of Alzheimer's disease and inhibition was shown to attenuate dendritic spine loss [82]. Mechanistically the protective effect of GSK3 inhibition was linked to preserved CREB activity and increased expression of the CREB target gene BDNF. A recent clinical trial in patients who were already being treated for Alzheimer's disease suggests that disease progression and extent of GSK3 inhibition will both be important factors to

consider in using GSK3 as a treatment target [83]. Peptides that mimic GSK3-primed substrates are currently being developed and may provide advantages over ATP-competitive inhibitors, including higher selectivity and weaker GSK3 inhibition [84]. These studies and others convincingly show GSK3 as a player in Alzheimer's disease [85], but raise questions about the sequence of events in the etiology and progression of spontaneous age-related Alzheimer's disease. It will be of profound interest to understand which of the roles identified for GSK3 in Alzheimer disease models, as a factor promoting amyloid and NFT pathology or as a factor responding to the burden of amyloid and NFT pathology, is the more physiologically important one during human disease development and how it might be effectively targeted as a clinical intervention.

Cancer: As a key regulator of cell fate GSK3 has been implicated in the biology of many different cancers, both as an oncogene and as a tumor suppressor. Elevated GSK3b expression has been observed in pancreatic cancer cell lines, where it was responsible for promoting NF-kB activity and was necessary for NF-kB mediated proliferation and survival [86]. High levels of GSK3 expression have been observed in colon, liver, and ovarian cancers; however, the physiological significance of this is not known [87]. The role of GSK3 as a tumor suppressor is perhaps better understood. GSK3 is an effector of the WNT signaling pathway that targets beta-catenin for degradation, thus blocking the transcription of oncogenic targets. Expression of a kinase-inactive form of GSK3b in mice acts as a dominant negative and promotes the formation of mammary tumors that express high levels of beta catenin and cyclin D1 [88]. GSK3 may also play a role in the enhanced survival of cancer cells by controlling the localization and activation of bcl-2 family protein Bax, a key regulator of apoptosis [33]. Mcl-1 is another bcl-2 family protein linked to GSK3. Ablation of the GSK3b phosphorylation site on stabilizes Mcl-1, blocks apoptosis, and desensitizes cells to chemotherapeutics, again supporting a role for GSK3 in cancer development and as a target for enhancing cancer therapies [89]. Another aspect of cancer biology linked to GSK3 is the epithelial-mesenchymal transition (EMT), a process that renders cancer cells more motile and metastatic.

GSK3 targets the transcriptional repressor Snail for proteasomal degradation resulting in maintenance of E cadherin expression [90]. E cadherin expression is required for normal adhesion of epithelial cells, so loss of this protein is a key step in the EMT. Taken together, these studies reveal a complex, and often contradictory role for GSK3 in the biology of cancer. Importantly, the stabilization of beta catenin remains an unwanted consequence of GSK3 inhibitors. Development of isoform-selective inhibitors for GSK3 has promise for the treatment of acute myeloid leukemia [91]. In this study, selective inhibition of GSK3a was shown to block AML colony formation without causing beta-catenin stabilization, and impaired leukemia initiation and prolonged survival in vivo. Many GSK3 inhibitors fail clinical trials because of off-target toxicities. A better understanding of the biology of GSK3 will be imperative if treatments focusing on this key growth responsive kinase are to be selective and effective.

Normative Aging: The role of GSK3 in normative aging has only recently been investigated. GSK3b protein levels increase in multiple regions of the rat brain with age [92]. Conversely, the neuroprotective intervention of CR is associated with lower protein levels of GSK3b in both mouse and rhesus hippocampus and relatively greater levels of inhibitory serine-9 phosphorylation [93]. Further evidence for a role of GSK3 in aging comes from shorter lived species. In worms, GSK3 inhibition resulted in dose-dependent increases in lifespan that was accompanied by chromatin remodeling [94]. Another study found that lithium increased mitochondrial energetics in worms and postulated that lithium resulted in selective autophagy of dysfunctional mitochondria [95]. In flies, lithium resulted in dose-dependent reduction in triglycerides and increased xenobiotic resistance, and the lifespan promoting effect of lithium was dependent upon activation of NRF-1 [96]. Conversely, overexpression of Shaggy, the GSK3 homologue in flies resulted in shortened lifespan that was partially rescued by lithium. These results show that GSK3 is relevant to longevity and suggest that its ability regulate metabolism is central to its role in aging. Although GSK3a KO mice have improved glucoregulatory function early in life, these mice exhibit shortened lifespans and increased age-related pathology [97]. This includes cardiac dysfunction, early onset of sarcopenia,

and increases in cellular senescence, some of which are thought to occur partially through activation of mTOR Complex 1. Therefore, it appears that both GSK3 loss of function and gain of function can negatively impact lifespan under different circumstances. Given the established role of GSK3 in development, studies that use conditional modulation of GSK3 would be required to dissect its role specifically in the aging process.

Conclusion

From its initial identification as a regulator of glycogen metabolism, the known functions of GSK3 have expanded to encompass numerous fundamental pathways. GSK3 plays multifactorial roles in growth signaling, inflammation, senescence, cell fate, and energy metabolism. Each of these pathways has been implicated in age-related dysfunction, suggesting that GSK3 may play a central role in the increased disease vulnerability that accompanies aging. Many of the disease and disorders of age have been studied in isolation and many transgenic mouse studies employ young animals. Nonetheless, across the literature, there is an interesting case to be made for GSK3 as a driver in aging and even perhaps as a potential target for intervention. Evidence to date suggests that GSK3 actions and responsivity to perturbation are highly context-dependent: differences in interactions and flux through GSK3-regulated path-ways occur as a function of cell type, tissue type, and background metabolic status. High granularity studies focusing on GSK3 biology, in particular, the impact of status and combinations of signaling inputs on cellular outcome, should be highly informative. If dysregulation of GSK3 is indeed causal age-related disease vulnerability, targeted therapeutic strategies could prove effective across a spectrum of age-related diseases.

REFERENCES

1 Kennedy, B. K. *et al.* Aging: a common driver of chronic diseases and a target for novel interventions. *Cell* **159**, 709-713, doi:10.1016/j.cell.2014.10.039 (2014).
2 Bonomini, F., Rodella, L. F. & Rezzani, R. in *Aging Dis* Vol. 6 109-120 (2015).
3 Balasubramanian, P., Howell, P. R. & Anderson, R. M. Aging and Caloric Restriction Research: A Biological Perspective With Translational Potential. *EBioMedicine* **21**, 37-44, doi:10.1016/j.ebiom.2017.06.015 (2017).
4 Bartke, A. Somatic growth, aging, and longevity. *NPJ Aging Mech Dis* **3**, 14, doi:10.1038/s41514-017-0014-y (2017).
5 Fontana, L. & Partridge, L. Promoting Health and Longevity through Diet: from Model Organisms to Humans. *Cell* **161**, 106-118, doi:10.1016/j.cell.2015.02.020 (2015).
6 Beurel, E., Grieco, S. F. & Jope, R. S. Glycogen synthase kinase-3 (GSK3): regulation, actions, and diseases. *Pharmacol Ther* **148**, 114-131, doi:10.1016/j.pharmthera.2014.11.016 (2015).
7 Woodgett, J. R. Molecular cloning and expression of glycogen synthase kinase-3/factor A. *Embo j* **9**, 2431-2438 (1990).
8 Hoeflich, K. P. *et al.* Requirement for glycogen synthase kinase-3beta in cell survival and NF-kappaB activation. *Nature* **406**, 86-90, doi:10.1038/35017574 (2000).
9 Kaidanovich-Beilin, O. *et al.* Abnormalities in brain structure and behavior in GSK-3alpha mutant mice. *Mol Brain* **2**, 35, doi:10.1186/1756-6606-2-35 (2009).
10 MacAulay, K. *et al.* Glycogen synthase kinase 3alpha-specific regulation of murine hepatic glycogen metabolism. *Cell Metab* **6**, 329-337, doi:10.1016/j.cmet.2007.08.013 (2007).
11 Cross, D. A., Alessi, D. R., Cohen, P., Andjelkovich, M. & Hemmings, B. A. Inhibition of glycogen synthase kinase-3 by insulin mediated by protein kinase B. *Nature* **378**, 785-789, doi:10.1038/378785a0 (1995).
12 Dominguez, I., Itoh, K. & Sokol, S. Y. Role of glycogen synthase kinase 3p3 as a negative regulator of dorsoventral axis formation in Xenopus embryos. **92**, 8498-8502 (1995).
13 Ding, V. W., Chen, R. H. & McCormick, F. Differential regulation of glycogen synthase kinase 3beta by insulin and Wnt signaling. *J Biol Chem* **275**, 32475-32481, doi:10.1074/jbc.M005342200 (2000).
14 Sutherland, C. What Are the bona fide GSK3 Substrates? *Int J Alzheimers Dis* **2011**, 505607, doi:10.4061/2011/505607 (2011).
15 Jope, R. S. & Johnson, G. V. The glamour and gloom of glycogen synthase kinase-3. *Trends Biochem Sci* **29**, 95-102, doi:10.1016/j.tibs.2003.12.004 (2004).
16 Jope, R. S. *et al.* Stressed and inflamed, can GSK3 be blamed? *Trends Biochem Sci* **42**, 180-192, doi:10.1016/j.tibs.2016.10.009 (2017).
17 Klein, P. S. & Melton, D. A. A molecular mechanism for the effect of lithium on development. *Proc Natl Acad Sci U S A* **93**, 8455-8459 (1996).
18 Hanger, D. P., Hughes, K., Woodgett, J. R., Brion, J. P. & Anderton, B. H. Glycogen synthase kinase-3 induces Alzheimer's disease-like phosphorylation of tau: generation of paired helical filament epitopes and neuronal localisation of the kinase. *Neurosci Lett* **147**, 58-62 (1992).
19 Stambolic, V. & Woodgett, J. R. Mitogen inactivation of glycogen synthase kinase-3 beta in intact cells via serine 9 phosphorylation. *Biochem J* **303 (Pt 3)**, 701-704 (1994).
20 Frame, S. & Cohen, P. GSK3 takes centre stage more than 20 years after its discovery. *Biochem J* **359**, 1-16 (2001).
21 Eldar-Finkelman, H., Seger, R., Vandenheede, J. R. & Krebs, E. G. Inactivation of glycogen synthase kinase-3 by epidermal growth factor is mediated by mitogen-activated protein kinase/p90 ribosomal protein S6 kinase signaling pathway in NIH/3T3 cells. *J Biol Chem* **270**, 987-990 (1995).

22 Manning, B. D. & Toker, A. AKT/PKB Signaling: Navigating the Network. *Cell* **169**, 381-405, doi:10.1016/j.cell.2017.04.001 (2017).

23 Hermida, M. A., Dinesh Kumar, J. & Leslie, N. R. GSK3 and its interactions with the PI3K/AKT/mTOR signalling network. *Adv Biol Regul* **65**, 5-15, doi:10.1016/j.jbior.2017.06.003 (2017).

24 Inoki, K. *et al.* TSC2 integrates Wnt and energy signals via a coordinated phosphorylation by AMPK and GSK3 to regulate cell growth. *Cell* **126**, 955-968, doi:10.1016/j.cell.2006.06.055 (2006).

25 Buller, C. L. *et al.* A GSK-3/TSC2/mTOR pathway regulates glucose uptake and GLUT1 glucose transporter expression. *Am J Physiol Cell Physiol* **295**, C836-843, doi:10.1152/ajpcell.00554.2007 (2008).

26 Welsh, G. I., Miller, C. M., Loughlin, A. J., Price, N. T. & Proud, C. G. Regulation of eukaryotic initiation factor eIF2B: glycogen synthase kinase-3 phosphorylates a conserved serine which undergoes dephosphorylation in response to insulin. *FEBS Lett* **421**, 125-130 (1998).

27 Koo, J., Wu, X., Mao, Z., Khuri, F. R. & Sun, S. Y. Rictor Undergoes Glycogen Synthase Kinase 3 (GSK3)-dependent, FBXW7-mediated Ubiquitination and Proteasomal Degradation. *J Biol Chem* **290**, 14120-14129, doi:10.1074/jbc.M114.633057 (2015).

28 Zhang, H. H., Lipovsky, A. I., Dibble, C. C., Sahin, M. & Manning, B. D. S6K1 regulates GSK3 under conditions of mTOR-dependent feedback inhibition of Akt. *Mol Cell* **24**, 185-197, doi:10.1016/j.molcel.2006.09.019 (2006).

29 Liberman, Z. Serine 332 Phosphorylation of Insulin Receptor Substrate-1 by Glycogen Synthase Kinase-3 Attenuates Insulin Signaling *. **280**, 4422-4428, doi:10.1074/jbc.M410610200 (2005).

30 Sharfi, H. & Eldar-Finkelman, H. Sequential phosphorylation of insulin receptor substrate-2 by glycogen synthase kinase-3 and c-Jun NH2-terminal kinase plays a role in hepatic insulin signaling. *Am J Physiol Endocrinol Metab* **294**, E307-315, doi:10.1152/ajpendo.00534.2007 (2008).

31 Leng, S., Zhang, W., Zheng, Y., Liberman, Z. & Rhodes, C. J. Glycogen synthase kinase 3 b mediates high glucose-induced ubiquitination and proteasome degradation of insulin receptor substrate 1. doi:10.1677/JOE-09-0456 (2009).

32 Maccario, H., Perera, N. M., Davidson, L., Downes, C. P. & Leslie, N. R. PTEN is destabilized by phosphorylation on Thr366. *Biochem J* **405**, 439-444, doi:10.1042/bj20061837 (2007).

33 Maurer, U., Preiss, F., Brauns-Schubert, P., Schlicher, L. & Charvet, C. GSK-3 - at the crossroads of cell death and survival. *J Cell Sci* **127**, 1369-1378, doi:10.1242/jcs.138057 (2014).

34 Maurer, U., Charvet, C., Wagman, A. S., Dejardin, E. & Green, D. R. Glycogen synthase kinase-3 regulates mitochondrial outer membrane permeabilization and apoptosis by destabilization of MCL-1. *Mol Cell* **21**, 749-760 (2006).

35 Pastorino, J. G., Hoek, J. B. & Shulga, N. Activation of glycogen synthase kinase 3beta disrupts the binding of hexokinase II to mitochondria by phosphorylating voltage-dependent anion channel and potentiates chemotherapy-induced cytotoxicity. *Cancer Res* **65**, 10545-10554, doi:10.1158/0008-5472.can-05-1925 (2005).

36 Tanno, M. *et al.* Translocation of glycogen synthase kinase-3beta (GSK-3beta), a trigger of permeability transition, is kinase activity-dependent and mediated by interaction with voltage-dependent anion channel 2 (VDAC2). *J Biol Chem* **289**, 29285-29296, doi:10.1074/jbc.M114.563924 (2014).

37 Watcharasit, P. *et al.* Glycogen synthase kinase-3beta (GSK3beta) binds to and promotes the actions of p53. *J Biol Chem* **278**, 48872-48879, doi:10.1074/jbc.M305870200 (2003).

38 Kim, W.-Y. *et al.* GSK-3 is a master regulator of neural progenitor homeostasis. *Nature Neuroscience* **12**, 1390, doi:doi:10.1038/nn.2408 (2009).

39 Eom, T. Y. & Jope, R. S. Blocked inhibitory serine-phosphorylation of glycogen synthase kinase-3alpha/beta impairs in vivo neural precursor cell proliferation. *Biol Psychiatry* **66**, 494-502, doi:10.1016/j.biopsych.2009.04.015 (2009).

40 Lopez-Otin, C., Blasco, M. A., Partridge, L., Serrano, M. & Kroemer, G. The hallmarks of aging. *Cell* **153**, 1194-1217, doi:10.1016/j.cell.2013.05.039 (2013).

41 Martin, M., Rehani, K., Jope, R. S. & Michalek, S. M. Toll-like receptor – mediated cytokine production is differentially regulated by glycogen synthase kinase 3. **6**, 777-784, doi:10.1038/ni1221 (2005).

42 Grimes, C. A. & Jope, R. S. CREB DNA binding activity is inhibited by glycogen synthase kinase-3 beta and facilitated by lithium. *J Neurochem* **78**, 1219-1232 (2001).

43 Lucas, J. J. *et al.* Decreased nuclear beta-catenin, tau hyperphosphorylation and neurodegeneration in GSK-3beta conditional transgenic mice. *Embo j* **20**, 27-39, doi:10.1093/emboj/20.1.27 (2001).

44 Bullock, B. P. & Habener, J. F. Phosphorylation of the cAMP response element binding protein CREB by cAMP-dependent protein kinase A and glycogen synthase kinase-3 alters DNA-binding affinity, conformation, and increases net charge. *Biochemistry* **37**, 3795-3809, doi:10.1021/bi970982t (1998).

45 Medunjanin, S. *et al.* GSK-3beta controls NF-kappaB activity via IKKgamma/NEMO. *Sci Rep* **6**, 38553, doi:10.1038/srep38553 (2016).

46 Zhang, X. *et al.* Hypothalamic IKKbeta/NF-kappaB and ER stress link overnutrition to energy imbalance and obesity. *Cell* **135**, 61-73, doi:10.1016/j.cell.2008.07.043 (2008).

47 Gulen, M. F. *et al.* Inactivation of the enzyme GSK3alpha by the kinase IKKi promotes AKT-mTOR signaling pathway that mediates interleukin-1-induced Th17 cell maintenance. *Immunity* **37**, 800-812, doi:10.1016/j.immuni.2012.08.019 (2012).

48 Hu, X. *et al.* IFN-gamma suppresses IL-10 production and synergizes with TLR2 by regulating GSK3 and CREB/AP-1 proteins. *Immunity* **24**, 563-574, doi:10.1016/j.immuni.2006.02.014 (2006).

49 Osorio, F. G. *et al.* Nuclear lamina defects cause ATM-dependent NF-kappaB activation and link accelerated aging to a systemic inflammatory response. *Genes Dev* **26**, 2311-2324, doi:10.1101/gad.197954.112 (2012).

50 Franceschi, C. & Campisi, J. Chronic inflammation (inflammaging) and its potential contribution to age-associated diseases. *J Gerontol A Biol Sci Med Sci* **69 Suppl 1**, S4-9, doi:10.1093/gerona/glu057 (2014).

51 Salminen, A., Kaarniranta, K. & Kauppinen, A. Inflammaging: disturbed interplay between autophagy and inflammasomes. *Aging (Albany NY)* **4**, 166-175 (2012).

52 Campisi, J. & d'Adda di Fagagna, F. Cellular senescence: when bad things happen to good cells. *Nat Rev Mol Cell Biol* **8**, 729-740, doi:10.1038/nrm2233 (2007).

53 Wiley, C. D. *et al.* Mitochondrial Dysfunction Induces Senescence with a Distinct Secretory Phenotype. *Cell Metab* **23**, 303-314, doi:10.1016/j.cmet.2015.11.011 (2016).

54 Xu, M. *et al.* Senolytics improve physical function and increase lifespan in old age. *Nat Med* **24**, 1246-1256, doi:10.1038/s41591-018-0092-9 (2018).

55 Seo, Y. H. *et al.* Enhanced glycogenesis is involved in cellular senescence via GSK3/GS modulation. *Aging Cell* **7**, 894-907, doi:10.1111/j.1474-9726.2008.00436.x (2008).

56 Zmijewski, J. W. & Jope, R. S. Nuclear accumulation of glycogen synthase kinase-3 during replicative senescence of human fibroblasts. *Aging Cell* **3**, 309-317, doi:10.1111/j.1474-9728.2004.00117.x (2004).

57 Kwon, S. M., Hong, S. M., Lee, Y. K., Min, S. & Yoon, G. Metabolic features and regulation in cell senescence. *BMB Rep* **52**, 5-12 (2019).

58 Kirkland, J. L. & Tchkonia, T. Cellular Senescence: A Translational Perspective. *EBioMedicine* **21**, 21-28, doi:10.1016/j.ebiom.2017.04.013 (2017).

59 Anderson, R. M. & Weindruch, R. Metabolic reprogramming, caloric restriction and aging. *Trends Endocrinol Metab* **21**, 134-141, doi:S1043-2760(09)00194-5 [pii] 10.1016/j.tem.2009.11.005 (2010).

60 Barger, J. L. *et al.* A Conserved Transcriptional Signature of Delayed Aging and Reduced Disease Vulnerability Is Partially Mediated by SIRT3. *PLoS One* **10**, e0120738, doi:10.1371/journal.pone.0120738 (2015).

61 Steinberg, G. R. & Carling, D. AMP-activated protein kinase: the current landscape for drug development. *Nat Rev Drug Discov*, doi:10.1038/s41573-019-0019-2 (2019).

62 Suzuki, T. *et al.* Inhibition of AMPK catabolic action by GSK3. *Mol Cell* **50**, 407-419, doi:10.1016/j.molcel.2013.03.022 (2013).

63 Hoshi, M. *et al.* Regulation of mitochondrial pyruvate dehydrogenase activity by tau protein kinase I/glycogen synthase kinase 3beta in brain. doi:10.1073/pnas.93.7.2719 (1996).

64 Chou, C. H. *et al.* GSK3beta-mediated Drp1 phosphorylation induced elongated mitochondrial morphology against oxidative stress. *PLoS One* **7**, e49112, doi:10.1371/journal.pone.0049112 (2012).

65 Anderson, R. M. *et al.* Dynamic regulation of PGC1alpha localization and turnover implicates mitochondrial adaptation in calorie restriction and the stress response. *Aging Cell* **7**, 101-111, doi:10.1111/j.1474-9726.2007.00357.x (2008).

66 Olson, B. L. *et al.* SCF Cdc4 acts antagonistically to the PGC1 ⎵ transcriptional coactivator by targeting it for ubiquitin-mediated proteolysis. 252-264, doi:10.1101/gad.1624208.cose (2008).

67 Hinds, T. D. *et al.* in *J Biol Chem* Vol. 291 25179-25191 (2016).

68 Nikoulina, S. E. *et al.* Potential role of glycogen synthase kinase-3 in skeletal muscle insulin resistance of type 2 diabetes. *Diabetes* **49**, 263-271 (2000).

69 Pearce, N. J. *et al.* Development of glucose intolerance in male transgenic mice overexpressing human glycogen synthase kinase-3beta on a muscle-specific promoter. *Metabolism* **53**, 1322-1330 (2004).

70 Patel, S. *et al.* Tissue-specific role of glycogen synthase kinase 3beta in glucose homeostasis and insulin action. *Mol Cell Biol* **28**, 6314-6328, doi:10.1128/mcb.00763-08 (2008).

71 Chen, H. *et al.* PI3K-resistant GSK3 controls adiponectin formation and protects from metabolic syndrome. *Proc Natl Acad Sci U S A* **113**, 5754-5759, doi:10.1073/pnas.1601355113 (2016).

72 Liu, Z., Tanabe, K., Bernal-Mizrachi, E. & Permutt, M. A. Mice with beta cell overexpression of glycogen synthase kinase-3beta have reduced beta cell mass and proliferation. *Diabetologia* **51**, 623-631, doi:10.1007/s00125-007-0914-7 (2008).

73 Liu, Y. *et al.* Conditional ablation of Gsk-3β in islet beta cells results in expanded mass and resistance to fat feeding-induced diabetes in mice. *Diabetologia* **53**, 2600-2610, doi:10.1007/s00125-010-1882-x (2010).

74 Mussmann, R. *et al.* Inhibition of GSK3 promotes replication and survival of pancreatic beta cells. *J Biol Chem* **282**, 12030-12037, doi:10.1074/jbc.M609637200 (2007).

75 Yamaguchi, H. *et al.* Preferential labeling of Alzheimer neurofibrillary tangles with antisera for tau protein kinase (TPK) I/glycogen synthase kinase-3 beta and cyclin-dependent kinase 5, a component of TPK II. *Acta Neuropathol* **92**, 232-241 (1996).

76 Pei, J. J. *et al.* Distribution of active glycogen synthase kinase 3beta (GSK-3beta) in brains staged for Alzheimer disease neurofibrillary changes. *J Neuropathol Exp Neurol* **58**, 1010-1019 (1999).

77 Phiel, C. J., Wilson, C. A., Lee, V. M. & Klein, P. S. GSK-3alpha regulates production of Alzheimer's disease amyloid-beta peptides. *Nature* **423**, 435-439, doi:10.1038/nature01640 (2003).

78 Hurtado, D. E. *et al.* Selectively silencing GSK-3 isoforms reduces plaques and tangles in mouse models of Alzheimer's disease. *J Neurosci* **32**, 7392-7402, doi:10.1523/JNEUROSCI.0889-12.2012 (2012).

79 Hernandez, F., Borrell, J., Guaza, C., Avila, J. & Lucas, J. J. Spatial learning deficit in transgenic mice that conditionally over-express GSK-3beta in the brain but do not form tau filaments. *J Neurochem* **83**, 1529-1533 (2002).

80 Engel, T., Hernandez, F., Avila, J. & Lucas, J. J. Full reversal of Alzheimer's disease-like phenotype in a mouse model with conditional overexpression of glycogen synthase kinase-3. *J Neurosci* **26**, 5083-5090, doi:10.1523/jneurosci.0604-06.2006 (2006).

81 Hooper, C. *et al.* Glycogen synthase kinase-3 inhibition is integral to long-term potentiation. *Eur J Neurosci* **25**, 81-86, doi:10.1111/j.1460-9568.2006.05245.x (2007).

82 DaRocha-Souto, B. *et al.* Activation of glycogen synthase kinase-3 beta mediates beta-amyloid induced neuritic damage in Alzheimer's disease. *Neurobiol Dis* **45**, 425-437, doi:10.1016/j.nbd.2011.09.002 (2012).

83 Lovestone, S. *et al.* A phase II trial of tideglusib in Alzheimer's disease. *J Alzheimers Dis* **45**, 75-88, doi:10.3233/jad-141959 (2015).

84 Eldar-Finkelman, H. & Martinez, A. GSK-3 Inhibitors: Preclinical and Clinical Focus on CNS. *Front Mol Neurosci* **4**, doi:10.3389/fnmol.2011.00032 (2011).

85 Llorens-Marítin, M., Jurado, J., Hernández, F. & Ávila, J. GSK-3β, a pivotal kinase in Alzheimer disease. *Front Mol Neurosci* **7**, doi:10.3389/fnmol.2014.00046 (2014).

86 Ougolkov, A. V., Fernandez-Zapico, M. E., Savoy, D. N., Urrutia, R. A. & Billadeau, D. D. Glycogen synthase kinase-3beta participates in nuclear factor kappaB-mediated gene transcription and cell survival in pancreatic cancer cells. *Cancer Res* **65**, 2076-2081, doi:10.1158/0008-5472.CAN-04-3642 (2005).

87 McCubrey, J. A. *et al.* GSK-3 as potential target for therapeutic intervention in cancer. *Oncotarget* **5**, 2881-2911 (2014).

88 Farago, M. *et al.* Kinase-inactive glycogen synthase kinase 3beta promotes Wnt signaling and mammary tumorigenesis. *Cancer Res* **65**, 5792-5801, doi:10.1158/0008-5472.CAN-05-1021 (2005).

89 Ding, Q. *et al.* Degradation of Mcl-1 by beta-TrCP mediates glycogen synthase kinase 3-induced tumor suppression and chemosensitization. *Mol Cell Biol* **27**, 4006-4017, doi:10.1128/mcb.00620-06 (2007).

90 Doble, B. W. & Woodgett, J. R. Role of glycogen synthase kinase-3 in cell fate and epithelial-mesenchymal transitions. *Cells Tissues Organs* **185**, 73-84, doi:10.1159/000101306 (2007).

91 Wagner, F. F. *et al.* Exploiting an Asp-Glu "switch" in glycogen synthase kinase 3 to design paralog-selective inhibitors for use in acute myeloid leukemia. *Sci Transl Med* **10**, doi:10.1126/scitranslmed.aam8460 (2018).

92 Lee, S. J. *et al.* Age-related changes in glycogen synthase kinase 3beta (GSK3beta) immunoreactivity in the central nervous system of rats. *Neurosci Lett* **409**, 134-139, doi:10.1016/j.neulet.2006.09.026 (2006).

93 Martin, S. A. *et al.* Regional metabolic heterogeneity of the hippocampus is nonuniformly impacted by age and caloric restriction. *Aging Cell* **15**, 100-110, doi:10.1111/acel.12418 (2016).

94 McColl, G. *et al.* Pharmacogenetic analysis of lithium-induced delayed aging in Caenorhabditis elegans. *J Biol Chem* **283**, 350-357, doi:10.1074/jbc.M705028200 (2008).

95 Tam, Z. Y., Gruber, J., Ng, L. F., Halliwell, B. & Gunawan, R. Effects of lithium on age-related decline in mitochondrial turnover and function in Caenorhabditis elegans. *J Gerontol A Biol Sci Med Sci* **69**, 810-820, doi:10.1093/gerona/glt210 (2014).

96 Castillo-Quan, J. I. *et al.* Lithium Promotes Longevity through GSK3/NRF2-Dependent Hormesis. *Cell Rep* **15**, 638-650, doi:10.1016/j.celrep.2016.03.041 (2016).

97 Zhou, J. *et al.* GSK-3alpha is a central regulator of age-related pathologies in mice. *J Clin Invest* **123**, 1821-1832, doi:10.1172/jci64398 (2013).

Table 1.1

GSK3 Gain-of-function

PMID	Year	Isoform	Expression System	Functional Outcomes
11007782	2000	GSK3b[S9A]	Thy1-Cre	Tau hyperphosphorylation
12182887	2002			Reduced brain size
16943560	2006			Hypophagia, increased locomotor activity
11226152	2001	GSK3b	CamkIIa-Cre(Tet-off)	Astrogliosis, apoptosis, and neurodegeneration
12472906	2002			Impaired spatial memory
17241269	2007			Impaired long-term potentiation
15375789	2004	GSK3b	a-actin-Cre	Impaired glucoregulation, hyperlipidemia, and adiposity
15791206	2005	GSK3a[S21A] GSK3b[S9A]	Whole Body	Normal glucoregulation
27140617	2016			Resistance to HFD-induced adiposity and glucoregulatory dysfunction, increased adiponectin
18219478	2008	GSK3b[S9A]	Insulin2-Cre	Reduced beta-cell mass, impaired glucoregulation

GSK3 Loss-of-function

PMID	Year	Isoform	Expression System	Functional Outcomes
10894547	2000	GSK3b	Whole Body	Embryonic lethality mediated by TNFa
17908561	2007	GSK3a	Whole Body	Enhanced glucoregulation and IRS1 expression
19925672	2009			Reduced aggression, impaired motor coordination
23549082	2013			Reduced lifespan, sarcopenia, increased cellular senescence
18694957	2008	GSK3b	Albumin-Cre	Normal glucoregulation
			MLC1*f*-Cre	Enhanced glucoregulation and skeletal muscle glycogen
19801986	2009	GSK3a GSK3b	Whole Body Nestin-Cre	Progenitor pool expansion, impaired neurogenesis
20821187	2010	GSK3b	Insulin2-Cre	Enhanced glucoregulation, resistance to HFD-induced diabetes

Figure 1.1

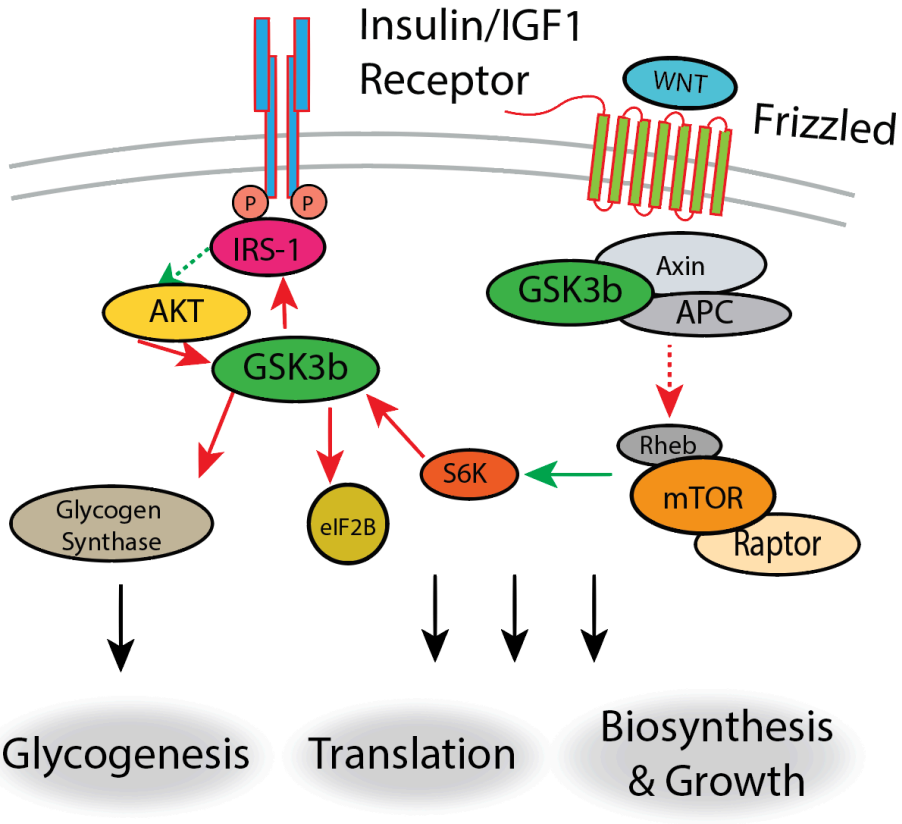

Figure 1.1. GSK3b & growth regulation. GSK3b activity is suppressed by the insulin/IGF1 and WNT signaling pathways. In the resting state, GSK3b is constitutively active and suppresses growth signaling, translation, and glycogenesis by phosphorylating multiple targets. Activation of Akt by the insulin signaling pathway leads to phosphorylation and suppression of GSK3b activity. GSK3b is also active in the absence of WNT signaling leading to inhibition of mTORC1 and cell growth. Conversely, active mTORC1 inhibits GSK3b activity in a negative feedback loop through S6K.

Figure 1.2

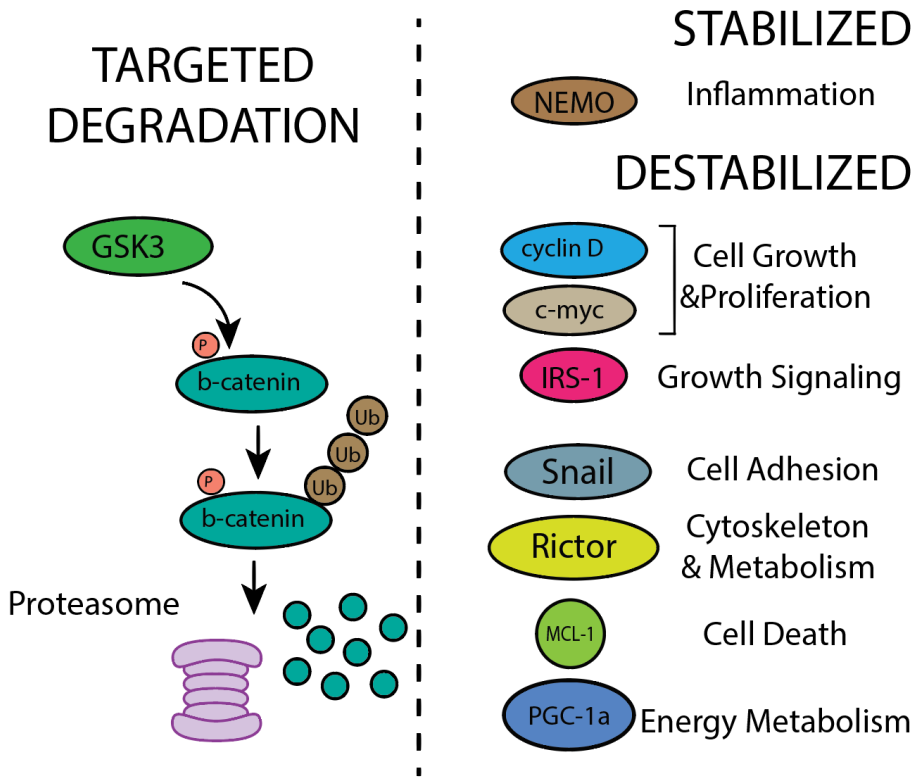

Figure 1.2. GSK3 phosphorylation regulates the stability of diverse protein targets. Many proteins phosphorylated by GSK3b are targeted for ubiquitin-mediated degradation, most notably beta-catenin in the absence of WNT signaling. These proteins are involved in diverse pathways that impact aging and disease vulnerability including inflammation, metabolism, growth, and different aspects of cell fate.

Figure 1.3

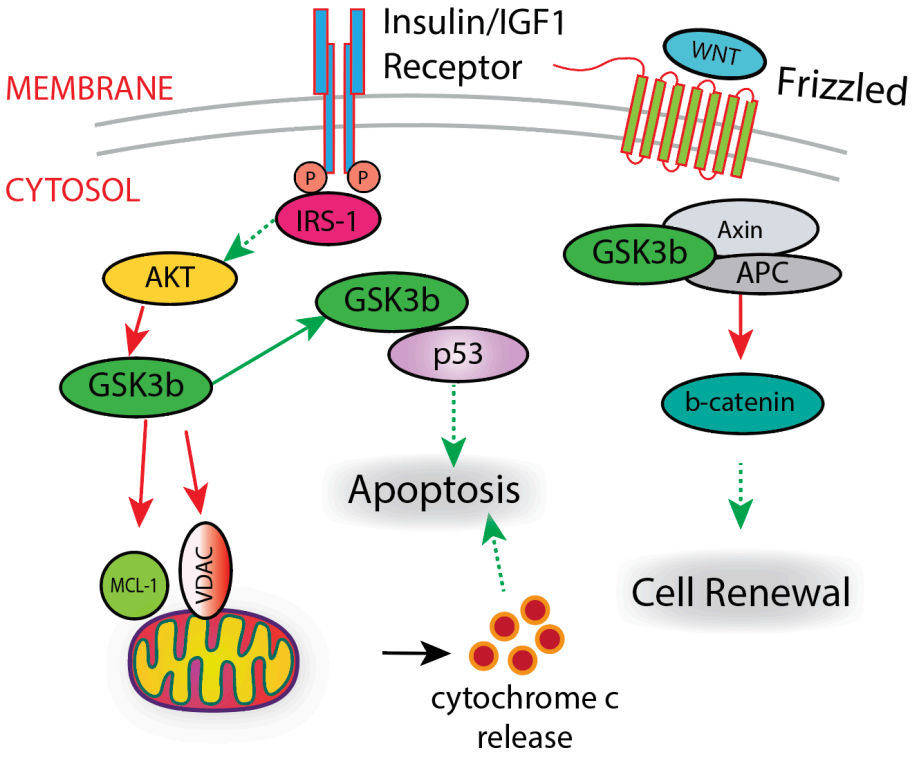

Figure 1.3. GSK3 regulates cell death, renewal, and differentiation. Active GSK3b increases mitochondrial permeability by phosphorylating proteins on the mitochondrial outer membrane. Subsequent release of cytochrome c triggers the intrinsic pathway leading to apoptosis. GSK3b also interacts with p53 and promotes cell cycle arrest and apoptosis. Inhibitory phosphorylation of GSK3b in response to insulin signaling promotes cell survival by blocking these pathways. Stem cell function is regulated in part through the activity of the WNT signaling pathway. GSK3b phosphorylates and targets beta catenin for degradation in the absence of WNT signaling, blocking stem cell renewal.

Figure 1.4

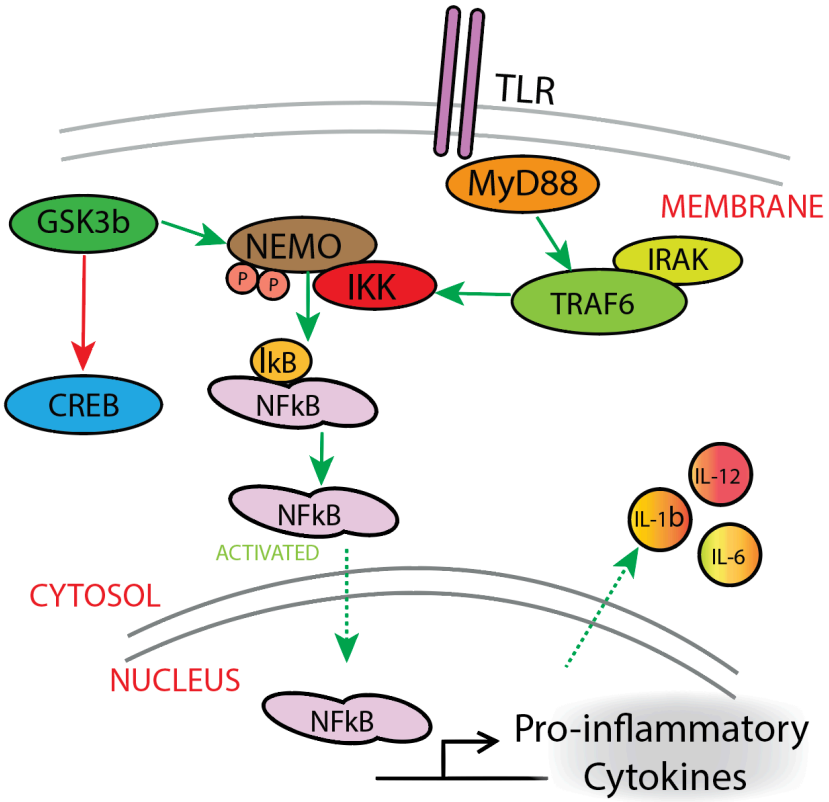

Figure 1.4. GSK3b regulates inflammation. Active GSK3b promotes NFkB stability and nuclear localization downstream of toll-like receptor (TLR) signaling, leading to the production of pro-inflammatory cytokines. Conversely, GSK3b blocks nuclear accumulation of CREB by promoting its degradation. GSK3b also promotes the integrity of TLR signaling by stabilizing NEMO, a factor that promotes the DNA binding activity of NFkB.

Figure 1.5

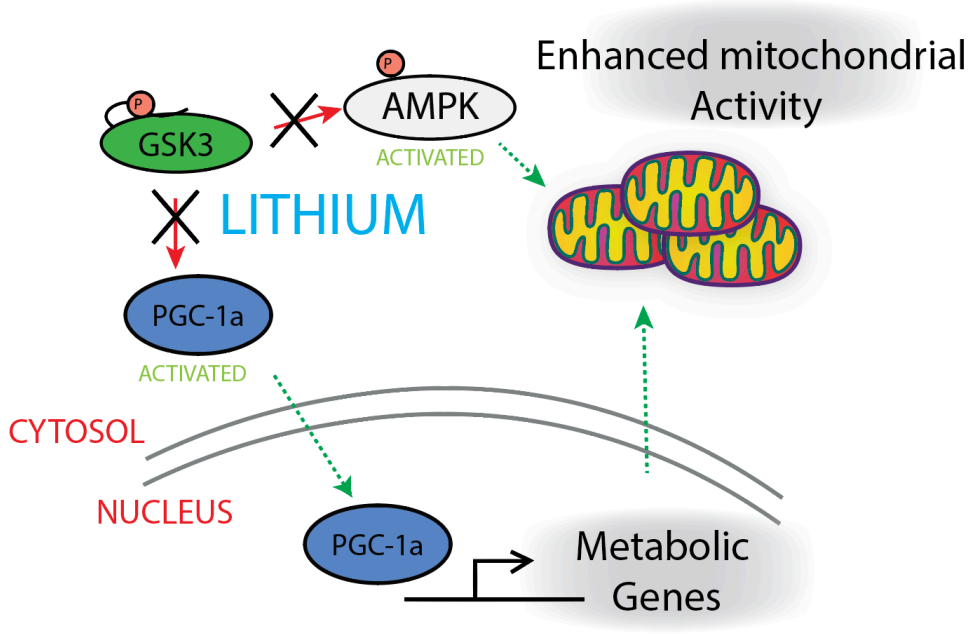

Figure 1.5. GSK3b regulates mitochondrial energy metabolism. Inhibition of GSK3b by lithium stabilizes PGC1a and increases mitochondrial respiration. Activated PGC1a increases expression of target genes coincident with increased respiration. GSK3 negatively regulates AMPK and activating phosphorylation of AMPK is increased with lithium. These nutrient sensing pathways converge on mitochondrial function, suggesting that GSK3 is a key upstream regulator of metabolism.

Chapter 2: GSK3b regulates cellular energy metabolism

Excerpts taken from the following published works:

GSK3b regulates brain energy metabolism
Stephen A. Martin*, Dylan C. Souder*, Karl N. Miller, Josef P. Clark, md Abdul Kader Sagar, Kevin W. Eliceiri, Luigi Puglielli, T. Mark Beasley, and Rozalyn M. Anderson.
*co-first author
Cell Reports. 2018 May 15;23(7): 1922-1931

Respiration experiments and subcellular fractionation were performed in collaboration with Stephen A Martin. Dylan C Souder performed the remaining experiments. Fluorescence lifetime imaging (FLIM) was conducted under the supervision of Abdul Kader Sagar.

ABSTRACT

Glycogen synthase-kinase 3-beta (GSK3b) is a key WNT effector and insulin-signaling kinase that plays broad roles in cellular growth and survival. GSK3b is enriched in the brain, where it controls neurogenesis, long-term potentiation, and neurotransmission. We previously identified GSK3b as a regulator of the mitochondrial response to oxidative stress, and here we sought to link GSK3b to energy metabolism in the brain focusing on metabolism of brain cells. In this study we use pharmacological and genetic techniques to show that lowering GSK3b activity enhances energy metabolism in glioblastoma cell lines and differentiated neuronal cell lines. Inhibition of GSK3b with lithium in H4 neuroglioma cells elevated mitochondrial respiration, intermediary metabolism, and increased protein stability of PGC1a, a transcriptional co-activator and key mitochondrial regulator. Importantly, expression of a lithium-insensitive GSK3b mutant demonstrated that the mitochondrial response to lithium is GSK3b-dependent. Lithium induced nuclear localization of PGC1a protein and transcriptional changes in PGC1a target genes, including the neurotrophin BDNF and metabolic genes involved in substrate utilization. The ability of lithium to influence NAD(P)H metabolism was conserved between cell types; however, neuron-like cells displayed a much higher magnitude response, emphasizing cell-type specificity in metabolic regulation. Cell size, growth rate, and cytoskeleton were altered with GSK3b inhibition. These data highlight a novel role for metabolic regulation by GSK3b and raise the possibility that GSK3b links energy production to a wide range of neuronal functions.

INTRODUCTION

Calorie restriction (CR) is the most robust and reproducible intervention to extend lifespan in a wide range of organisms[1]. One of the most fundamental and conserved observations in CR is the re-wiring of mitochondrial function and intermediary metabolism towards metabolic efficiency and growth repression[2]. CR is neuroprotective, improves neuroplasticity, and emerging evidence suggests that maintenance of mitochondrial integrity is important for these phenotypes[3,4]. Conversely, nutritional excess in human populations has been linked to dysfunction of metabolism and growth, ultimately leading to an accelerated rate of aging[5]. Several neurodegenerative diseases are associated with aging, including Alzheimer's disease (AD) and Parkinson's disease (PD). Crucially, these diseases share a common feature of mitochondrial dysfunction, a hallmark of the aging process that has been implicated in the early stages of disease processes[5]. Maintenance of mitochondrial function requires a fine-tuned balance of growth signaling and nutrient sensing that allows neurons to adapt to internal and external stimuli[6]. The following introduction describes how energy metabolism and growth signaling are perturbed with brain aging and disease. This chapter elucidates a novel mechanism for the regulation of central nervous system mitochondrial metabolism involving the growth-signaling sensitive kinase GSK3b, expanding our current understanding of mechanisms of brain aging and CR.

Both global and regional brain volume decreases with normal aging, including the hippocampus and temporal lobes[7]. Importantly, there is significant variability in the rate of brain atrophy among individuals implicating genetic characteristics in the pace of aging; however, growing evidence indicates that the rate of brain aging can be modified by diet and exercise[8]. The ability of diet to modify brain aging is exemplified by CR; CR delays age-related atrophy in areas of the frontal and temporal lobes as well as sub-cortical regions in rhesus monkeys[9]. Additionally, CR monkeys with higher insulin sensitivity had greater hippocampal and pre-frontal cortex gray matter volume[10], suggesting that insulin sensitivity is mechanistically important for neuroprotection by

CR. As discussed previously, GSK3b is a key insulin-effector that has been linked to neurodegenerative disease (Chapter 1)[11]. We reported that protein levels of GSK3b are lower and contain greater inhibitory phosphorylation in the hippocampus of CR mice and monkeys[12]. These data raise the possibility that insulin/growth signaling through GSK3b could play an important role in brain aging. Consistent with this idea, roles for growth signaling in longevity have been well-established in the literature. Ablation of insulin and mTORC1 pathway components is sufficient to extend lifespan in a range of animals[13]. Additionally, evidence in humans suggests that these laboratory findings have relevance to disease. Cortical and hippocampal volume is inversely related to insulin sensitivity in AD suggesting that growth signaling factors directly act on the brain[14]. Growth signaling status tightly regulates energy metabolism both systemically, and at the cellular level[15,16]. Therefore, effectors of growth signaling are prime targets for understand the mechanisms of neuroprotection in aging and disease.

Neuroimaging studies have demonstrated that brain energy metabolism changes with age. For example, ^{18}FDG PET imaging has revealed age-related decline in the rate of glucose uptake (CMR_{glc}) that precedes the emergence of dementia by decades[17]. PET imaging coupled to fMRI has shown that brain oxygen consumption ($CMRO_2$) is maintained with aging in contrast to CMR_{glc}, pointing to possible impairment of aerobic glycolysis and neuron-astrocyte cross talk[17]. The precise mechanisms of these changes are unknown; however, loss of CMR_{glc} is associated with peripheral insulin resistance[18]. In terms of cell signaling, insulin and insulin-like growth factor IGF-1 can be viewed as growth stimuli, promoting energy storage, biosynthesis, and anabolism[19]. A wealth of in vivo studies now point to peripheral insulin sensitivity and insulin-regulated processes as key components of the brain aging process[10,20]. Impairment of energy metabolism has also been implicated in the pathology of neurodegenerative diseases. Parkinson's disease (PD) in particular is strongly linked to mitochondrial dysfunction through Parkin, an E3 ubiquitin ligase that mediates mitophogy[21]. Intriguingly, Parkin loss-of-function has been linked to suppression of levels and activity PGC1a, a transcriptional co-activator and critical regulator of mitochondrial

function[22]. Our own lab has demonstrated profound changes in hippocampal energy metabolism change during normative aging in mice, suggesting that brain aging, and not just neurodegenerative disease, may also be tied to metabolic regulation[12].

As previously mentioned, upregulation of PGC1a target genes is highly represented in our molecular studies of CR[2]. PGC1a integrates cellular nutrient sensing and growth signaling to promote the expression of metabolic and mitochondrial genes[23]. Intriguingly, PGC1a stability and turnover is controlled by direct phosphorylation by GSK3b. In NIH 3T3 cells GSK3 targets PGC1a for proteasomal degradation during the response to oxidative stress, effectively controlling the timing of PGC1a nuclear localization[24]. GSK3b has also been connected to PGC1a stability in primary neurons, demonstrating that the GSK3b/PGC1a axis could be relevant to brain metabolism[25]. Collectively, these studies raise the possibility that GSK3b is mechanistically connected to PGC1a and energy metabolism in the context of delayed brain aging and CR .

The following chapter defines the role of GSK3b in regulating mitochondrial metabolism in cell culture models and connects GSK3b activity to PGC1a stability and transcriptional regulation. GSK3b expression differs greatly between brain regions and cell types[12]. Moreover, accumulating evidence suggests that regulatory roles of GSK3 are tissue and cell-type specific[26]. Here we use cell culture models of astrocytes (H4) and neurons (differentiated PC12) to determine if the GSK3b inhibitor lithium has an impact on mitochondrial function. Mitochondria are measured in this study through direct assays of mitochondrial membrane potential, respiration, and mitochondrial volume. Metabolic imaging and biochemical detection of NAD cofactor are used to determine the influence of GSK3b on intermediary metabolism. Finally, the mechanistic connection of GSK3b to metabolism and PGC1a are explored using genetic techniques and immunodetection of PGC1a protein in lithium treated cells.

RESULTS

GSK3b inhibition regulates mitochondrial metabolism in H4 cells

To determine whether GSK3b regulates mitochondrial function under basal conditions, inhibitors were employed in cultured cells. H4 neuroglioma cells were treated with lithium chloride [15mM], a direct inhibitor of GSK3b, in addition to the GSK3-specific ATP competitive inhibitor, inhibitor VIII [15uM]. Consistent with a growth regulatory role of GSK3b, treatment with either inhibitor suppressed cellular growth by 24h (Fig.2.1A). Lithium treatment increased mitochondrial membrane potential dose-dependently at 2h and 24h treatment (Fig2.1A-B). A similar effect was observed with inhibitor VIII treatment (Fig.2.1D). Cellular respiration and mitochondrial respiratory capacity were similarly increased with lithium treatment by 2h and maintained out to 24h (Fig.2.1E). Subtle differences between the impact of lithium and inhibitor VIII on mitochondrial membrane potential were observed; however, the effect on oxygen consumption was essentially equivalent and was not additive (Fig.2.1F). A biochemical enzyme linked assay of whole cell lysates revealed that total levels of NAD cofactor were modestly increased after 24h lithium treatment with no change in NAD/NADH redox ratio, suggesting that GSK3 regulates metabolic capacity (Fig.2.1G). Although lithium stimulated mitochondrial function, no differences in mitochondrial content were observed by immunofluorescence or by western blot of electron transport chain proteins (Fig.2.1H-I). These data reveal that changes in energetics are due to adaptation of mitochondria not expansion of mitochondria number.

GSK3b regulates PGC1a levels, stability, and localization in H4 cells

Lithium increased inhibitory serine-9 phosphorylation of GSK3b, consistent with prior reports, confirming the efficacy of lithium treatment (Fig.2.2A). Our lab previously demonstrated that GSK3b controls the stability of PGC1a protein during the response to oxidative stress. GSK3b is constitutively active under basal conditions, so we sought to determine if PGC1a levels were impacted by GSK3b inhibition. Both lithium and inhibitor VIII increased PGC1a levels at 24h, with

a 1.3-fold increase being observed in lithium treated cells (Fig.2.2B). To more directly assess the impact of lithium on PGC1a turnover, H4 cells were treated with the ribosomal inhibitor cycloheximide [100uM] in the presence or absence of lithium or inhibitor VIII. This assay informs of intrinsic protein stability by quantifying the rate of protein degradation. Cycloheximide treatment depleted PGC1a protein levels at 24h, but this effect was partially rescued by GSK3b inhibition (Fig.2.2C-D). These data show that under basal conditions PGC1a is continually targeted for degradation by GSK3 activity, confirming that our previous discovery in fibroblast cells is also relevant in cells of the central nervous system. We next investigated PGC1a subcellular distribution. As in fibroblasts, PGC1a was detected in the nucleus and in the cytosol[24]. Nuclear abundance of PGC1a was elevated in lithium treated cells based on immunofluorescent detection (Fig.2.2E) and confirmed by subcellular fractionation (Fig.2.1F). Intriguingly, lithium induced nuclear accumulation of both total and serine-9 phosphorylated GSK3b, although the significance of this change in localization of both active and presumed inactive forms of GSK3b is unknown. The increased nuclear accumulation of PGC1a raised the possibility that PGC1a target genes might be impacted. Lithium treatment increased mRNA levels of the canonical transcript, PGC1a1, as well as levels of PGC1a4, a transcript variant expressed off an alternative promoter. Transcript levels of a range of PGC1a target genes were also impacted, including the TCA cycle regulatory gene PDK4, BDNF, SCD1, and cytochrome c oxidase subunit 5b (Cox5b) (Fig.2.2G). These data collectively demonstrate that GSK3b regulates basal mitochondrial activity in cells and alters PGC1a protein stability, subcellular localization, and transcriptional activity.

GSK3b regulates metabolism and PGC1a in differentiated PC12 cells

Having established that GSK3b regulates metabolism in a glial cell line, we sought to determine if neuronal energy metabolism is impacted by lithium treatment. The rat adrenal gland-derived PC12 cell line can be differentiated into neurons through nerve growth factor (NGF) treatment. Treatment of differentiated PC12 cells with lithium chloride [15mM] resulted in an increase

of PGC1a protein levels (1.5-fold) at 24h that was accompanied by increased serine-9 phosphorylation of GSK3b, recapitulating what was observed in H4 cells (Fig.2.3A). Levels of PGC1a target genes BDNF and PDK4 mRNA were increase with lithium treatment in PC12 cells; however, lithium did not impact mRNA levels of the canonical PGC1a1 isoform and instead preferentially increased PGC1a4 levels (Fig.2.3B-C). Total levels of NAD cofactor detected using an enzyme-linked biochemical assay were increased in lithium-treated PC12 cells, representing an increase in the oxidized pool, as NADH levels remained unchanged. The NAD/NADH ratio trended upwards with lithium treatment, but did not reach significance (Fig.2.3D). Similar to H4 cells, these differences in cellular energetics were not explained by a difference in mitochondrial content shown by immunofluorescence (Fig.2.3E) or by immunostaining of electron transport chain complex I-V proteins (Fig.2.3F). PGC1a protein was almost entirely nuclear in differentiated PC12 cells both with and without lithium (Fig.2.3G); this is in contrast to H4 cells, where PGC1a localization was largely perinuclear in the untreated state and more nuclear with lithium treatment. GSK3b displayed a similar nuclear accumulation with lithium treatment in PC12 cells as H4 cells (Fig.2.3G). Interestingly, in the case of neurons serine-9 phosphorylated GSK3b formed discrete puncta in the perinuclear region after 24h of lithium treatment (Fig.2.3G). The significance of this change in localization is unclear. In terms of established GSK3-linked cell structural regulatory function, marked cytoskeletal changes occurred with GSK3b inhibition in these cells, including deterioration of filamentous actin and retraction of beta-actin to the perinuclear region (Fig.2.3G). Collectively, these data demonstrate that the impact of GSK3b on mitochondrial function, NAD metabolism, and PGC1a is common to glia and neuron-like cells, but the cellular morphology and cytoskeletal remodeling was more prominent in neurons.

GSK3b affects cellular NAD(P)H metabolism

Multiphoton laser scanning microscopy (MPLSM) is a high-resolution imaging based technique that allows for quantitation of differences in cellular metabolism among cells and as a function of treatment. This technology takes advantage of autofluorescence of reduced forms of NAD

and NADP cofactors. The latency between excitation and emission of an NAD(P)H fluorophore can be quantified by fluorescence lifetime imaging microscopy (FLIM), which produces a first order decay curve described by $\tau_m = a_1 \bullet \tau_1 + a_2 \bullet \tau_2$. The fast component ($\tau_1$) corresponds to the free pool of NAD(P)H, while the slow component (τ_2) represents the bound pool. Mean fluorescence lifetime (τ_m) summarizes the aggregate of these two pools and a_1/a_2 are coefficients that represent the total contribution of each pool to τ_m. Fluorescence decay curves were generated over multiple pulses, repeated for each pixel in the image capture field, and were quantified on a by-pixel basis and color-coded according to picoseconds of decay (Fig.2.4A-B). Mean fluorescence lifetime was lower in the nucleus compared to the cytosol in both H4 and differentiated PC12 cell types, consistent with a higher proportion of bound NAD(P)H in the mitochondria (Fig.2.4C-D). Intriguingly, lithium treatment increased τ_m in both the cytosolic and nuclear pools of H4 cells (Fig.2.4C), with main effects of treatment, cellular compartment, and a treatment by compartment interaction (Table 2.1). These differences extended to all parameters of the decay curve including higher τ_1 (free pool), a more modest increase in τ_2 (bound pool), and a substantial decrease in the contribution of free NAD(P)H to the total signal (a_1). These results are consistent with the increase in mitochondrial respiration and changes in cellular redox shown previously, and demonstrate that intermediary metabolism is markedly changed by lithium treatment. Mirroring changes in total NAD content, larger magnitude changes in FLIM were detected in lithium-treated PC12 cells. Significant increases in τ_m were observed with main effects of treatment, cellular compartment, and a treatment by compartment interaction (Table 2.2). All parameters of the decay curve were significantly changed, suggesting alterations in both the free and protein-bound NAD(P)H pools (Fig.2.4D). The outcomes observed in these cells are consistent with greater mitochondrial oxidative capacity in neurons compared to glia, and suggest that GSK3b plays are role in controlling metabolic capacity in both cell types. Fluorescence intensity of NAD(P)H is influenced by total levels of NAD(P)H and the proportion of NAD(P)H bound to the proteome. Lithium had no impact

on NAD(P)H fluorescence intensity in H4 cells after 24h treatment (Fig.2.4E); however, fluorescence intensity increased significantly in differentiated PC12 cells (Fig.2.4F). These data demonstrate that while metabolism of both cell types are lithium responsive, the magnitude and the nature of the response is cell type specific.

The impact of lithium on mitochondrial metabolism is GSK3b-dependent

To determine whether lithium-induced changes in mitochondrial function were GSK3b-dependent, we used siRNAs targeted to GSK3b transcript to knock down GSK3b protein levels. Transfection of H4 cells with siRNA against GSK3b resulted in an ~85% reduction of GSK3b protein levels at 48h (Fig.2.5A). Knockdown of GSK3b protein was sufficient to increase mitochondrial membrane potential and phenocopy the effect of lithium (Fig.2.5B), suggesting that GSK3b mediates the effects of lithium on mitochondrial function. Despite phenocopying the effect of lithium on mitochondrial membrane potential, knock-down of GSK3b did not produce the same transcriptional signature; BDNF was similarly upregulated with the knockdown, while no induction of PGC1a transcripts or metabolic genes was observed (Fig.2.5C). These data show that depletion of the protein is not the same as inhibition of the protein activity. The inhibitory effect of lithium is mediated by serine-9 phosphorylation of GSK3b protein[27]. We expressed a lithium-insensitive GSK3b mutant, GSK3b[S9A] in H4 cells to assess the dependence of the lithium-effect on GSK3b inhibition (Fig.2.5D). Transfection of GSK3b[S9A] into H4 cells was sufficient to decrease mitochondrial membrane potential by 48h of treatment (Fig.2.5E). Furthermore, expression of GSK3b[S9A] abrogated the ability of lithium to increase mitochondrial membrane potential by 24h (Fig.2.5E), demonstrating that lithium works through GSK3b to impact mitochondrial function.

Having shown that suppression of GSK3b activity upregulates mitochondrial function, we next investigated the impact of GSK3b overexpression. We developed an H4 cell line stably expressing a doxycycline-inducible GSK3b construct (pTLxG) capable of 4-fold induction of GSK3b transcript and 3-fold increase in GSK3b protein (Fig.2.5F-G). GSK3b overexpression significantly

impacted cell morphology and cytoskeletal structure. Cells overexpressing GSK3b were larger with greater average cell area (Fig.2.5H). Immunofluorescent detection of PGC1a revealed a decrease of PGC1a levels after 48h of GSK3b-transgene induction (Fig.2.5I), consistent with enhanced ubiquitin-mediated degradation mediated by GSK3b. Despite significant changes in cell growth and PGC1a levels, GSK3b overexpression failed to influence mitochondrial membrane potential (Fig2.5J), in contrast to the GSK3b[S9A] data shown previously. These data demonstrate that modulation of GSK3b impacts growth and PGC1a, but that the results are not reciprocal to what was observed with lithium.

DISCUSSION

These data establish a novel role for GSK3b in regulating energy metabolism and PGC1a protein in neurons and in glia. Both lithium and inhibitor VIII stimulated cellular respiration and elevated mitochondrial membrane potential. Importantly, knock-down of GSK3b phenocopied the ability of lithium to enhance mitochondrial membrane potential, establishing GSK3b as a *bona-fide* regulator of energy metabolism. Consistent with upregulation of mitochondrial function, PGC1a mRNA and protein levels were elevated with lithium treatment coincident with nuclear localization of PGC1a protein. Lithium also stabilized PGC1a protein in H4 cells. The evidence presented here suggests that both the stability and activity of PGC1a are enhanced under conditions of diminished GSK3b activity.

Intermediary metabolism was interrogated in this study through biochemical assay of NAD content and FLIM of endogenous NAD(P)H cofactor. Based on the biochemistry, both total and oxidized NAD cofactor were increased with lithium treatment, with a much greater magnitude effect observed in differentiated PC12 cells than in glia. FLIM of these cells mirrored changes in NAD cofactor content; lithium lengthened the fluorescence lifetime of NAD(P)H in both cell types, but to a much greater extent in differentiated PC12 cells. The changes in intermediary metabolism observed in this study are consistent with enhancement of mitochondrial oxidative metabolism.

The cell type specificity of the lithium response also matches what is known about neuron and astrocyte metabolism. Neurons display a much greater capacity to oxidize substrates than astrocytes, which are primarily glycolytic and rely on mitochondrial function for anaplerosis to a greater extent[28]. Here, the ability of lithium to more substantially affect PC12 likely reflects a greater respiratory capacity of the mitochondria. These data are consistent with our previously published work, which shows longer NAD(P)H lifetimes in neuropil compared to the non-neuronal brain cell populations[12].

From a mechanistic perspective, expression of a lithium-insensitive GSK3b mutant demonstrated that lithium works through GSK3b to impact mitochondrial function. Transfection of GSK3b[S9A] alone was sufficient to decrease mitochondrial membrane potential, and render H4 cells refractory to lithium treatment. Interestingly, overexpression of wild-type GSK3b through a doxycycline-inducible construct did not impact mitochondrial membrane potential, despite marked changes in cell size and the cytoskeleton. This conflicting result is likely explained by the ability of cells to physiologically limit activity of the transgenically-overexpressed GSK3b by endogenous mechanisms. The basal mitochondrial membrane potential of H4 cells is also lower than other cell lines tested in our hands (Chapter 4). It is possible that extremely low basal mitochondrial function in H4 cells cannot be altered without cellular toxicity. Further experiments in a more physiologically-relevant model (e.g. primary astrocytes) will be required to establish the impact of GSK3b overexpression.

The data presented here offer compelling evidence that GSK3b regulates mitochondrial function in cells of the central nervous system. As a constitutively active kinase, GSK3b would be expected to exert its' control under basal conditions, perhaps restraining oxidative metabolism in the absence of growth and nutrient signals. Neurogenesis, synaptic activity, and long term potentiation are all controlled by GSK3b[26], raising the possibility that energy production can be directly coupled to important neuronal functions through GSK3b activity. We previously published that CR

results in lower abundance of GSK3b in the hippocampus with coincident greater levels of inhibitory phosphorylation, and that these changes in endogenous GSK3b are associated with altered metabolism[12]. Now we propose that a direct relationship between GSK3b and energy metabolism exists in the aging brain. Enhancement of total NAD in particular has the potential to exert neuroprotective actions through the sirtuin family of metabolic regulators. Sirtuins are NAD dependent de-acetylases and use NAD as a co-substrate in their reactions[29]. Activation of SIRT1, by far the best characterized sirtuin, has been shown by others to stimulate mitochondrial activity, PGC1a-dependent transcription, and metabolic plasticity[30,31]. These mechanisms are NAD dependent and could contribute to CR's ability to delay age-related deterioration in the brain. SIRT1 has been shown to counter amyloidogenesis cultured neurons[32], suggesting that therapies aimed at boosting NAD could be beneficial. Coming back to the data shown here, lower levels of GSK3b activity with CR could result in stabilization of PGC1a protein and retention of mitochondrial plasticity even with advanced age. To gain further insight into specific mechanisms of GSK3b in influencing mitochondrial function in physiological systems studies in primary neurons, astrocytes, and mice will need to be conducted. Altogether, this study highlights a new pathway for metabolic regulation that could have mechanistic relevance for CR and age-related diseases such as AD.

METHODS

Cell Culture

H4 cells were obtained from ATCC (HTB-148; Manassas, VA, USA) and cultured in DMEM containing 10% fetal bovine serum and 1% penicillin/streptomycin. PC-12 cells were obtained from ATCC (CRL-1721) and cultured in Dulbecco's modified Eagle's medium (DMEM) with 10% horse serum, 5% fetal bovine serum, and 1% penicillin/streptomycin.

PC-12 Cell Differentiation

All PC-12 experiments were conducted on fully differentiated PC-12 cells (7 days of differentiation). For differentiation, PC-12 cells were plated on collagen coated plates and cultured for 7 days in DMEM containing 0.1% horse serum, 100 ng/ml 2.5S nerve growth factor (N-100; Alomone Labs, Jerusalem, Israel), and 1% penicillin/streptomycin. Media was changed every 2 days.

Lithium Treatment

Lithium time-course experiments were carried out using cell culture media supplemented with 15mM lithium chloride (LiCl). Media change was carried out 2 or 24 hours prior to collection as indicated. For PGC1a protein stability experiments, cells were pretreated for 1 hour with media containing 15mM LiCl or control media, followed by the direct addition of cycloheximide (100nM) or eqivalent volume of DMSO (vehicle) to the plates for the indicated time.

Lipofectamine Transfection

H4 cells were seeded in 6-well plates 24 hours prior to lipofectamine transfection (6ul/well). HA-GSK3b[S9A] and pcDNA3.1 control vectors were transfected at 3ug/well and media change was carried out 4 hours after transfection and prior to lithium treatment. GSK3b siRNA was transfected at 30nM for 24h and media was changed prior to lithium treatment.

Metabolic Assays

Mitochondrial membrane potential

Mitochondrial membrane potential was determined using the JC-1 assay (T-3168; Thermo Fisher Scientific) in accordance with the manufacturer's instructions. Cells were incubated in 1 µg/mL JC-1 dye for 15-minutes prior to counting and re-suspension in D-PBS for assay. Fluorescent emission was measured at 590nm and 530nm with excitation at 535nm and 485nm respectively.

Mitochondrial Respiration (Seahorse Assay)

Basal and maximal respiration of H4 cells was determined using a Seahorse extracellular flux (XF) Cell Mito Stress Test Kit (103015-100; Agilent Technologies, Santa Clara, CA, USA). Cells were plated at 4.0×10^4/well in a 96-well microplate using growth media in the presence or absence of 15mM LiCl and incubated overnight. One hour prior to assay, cells were switched into assay media in accordance with the manufacturer's instructions and incubated at 37 C in a non-CO_2 incubator. At the time of assay, cells were loaded into the XF analyzer along with a loaded sensor cartridge containing the following ETS inhibitors: Oligomycin (100 μM), FCCP (100uM), and Rotenone/antimycin A (50 μM). Inhibitors were sequentially injected into the assay media and basal respiration, ATP production, maximal respiration, and non-mitochondrial respiration were measured as a function of cellular oxygen consumption.

Cellular Respiration (OxoPlate Assay)

Oxygen consumption of H4 cells was determined using an Oxoplate (OP96U; Presens) oxygen monitoring system. Cells were suspended in respiration buffer (pH 7.4) containing D-Mannitol, Potassium Chloride (KCL), Magnesium Chloride ($MgCl_2$), and Monopotassium Phosphate (KH_2PO_4) at 4.0×10^5/well in quadruplicate. Fluorescent emission was measured at 650nm and 590nm with excitation at 540nm at 10-minute intervals at 37 C.

Biochemical NAD(H) Assays

NAD/NADH quantification was determined using the Biovision NAD/NADH quantification colorimetric assay kit (K337-100; Biovision) per manufacturer's instructions.

Cell Proliferation Analysis

Cellular proliferation was quantified using a CyQUANT direct cell proliferation assay (C35011; Thermo Fisher Scientific) per manufacturer's instructions.

Live/Dead Assay

Cellular viability in response to lithium and GSK3b inhibitor VIII treatment was determined using a Molecular Probes LIVE/DEAD Viability/Cytotoxicity Kit (L3224; Thermo Fisher Scientific).

Quantitation of transcript and protein abundance

Western Blotting and Antibodies

Cells were lysed and protein was extracted in modified RIPA buffer containing protease and phosphatase inhibitors (P8340 and 524624, respectively; Sigma Aldrich, St. Louis, MO, USA). Proteins were detected by immunoblotting using standard techniques. Antibodies used were PGC1α (sc-13067; Santa Cruz Biotechnology, Santa Cruz, CA, USA) GSK3b (9315; Cell Signaling Technologies, Boston, MA), serine 9 phospho-GSK3b (9336; Cell Signaling Technology), Total OXPHOS (ab110413; Abcam, Cambridge, MA, USA), Cyclin-d1 (ab7958; Abcam) beta-actin (A1978; Sigma Aldrich) and Sirt1 ((sc-74504, Santa Cruz), PARP (9542S; Cell Signaling). Subcellular fractionation was performed using nuclear/cytoplasmic fractionation kit (K266-100; Biovision, Milpitas, CA, USA) per manufacturer's instructions. Equivalent protein amounts were loaded for both the nucleus and cytoplasm.

RNA Analysis

Cells were lysed in Trizol (15596018; Thermo Fisher Scientific, Waltham, MA, USA) and RNA was isolated using Direct-zol RNA Miniprep kit (R2072; Zymo Research, Irvine, CA, USA) in accordance with manufacturers instructions. cDNA was synthesized using a High Capacity reverse transcription cDNA kit (4368813; Thermo Fisher Scientific). Quantitive real-time reverse transcription PCR was performed on an Applied Biosystems Prism 7900 using TaqMan and SYBR Green gene expression assays (Thermo Fisher Scientific)

Microscopy

Immunofluorescence Microscopy

Cellular localization was analyzed by immunofluorescence using standard techniques. H4 cells were cultured on glass coverslips and PC-12 cells were cultured on Nunc Lab-Tek CC2 chamber slides (154917; Thermo Fisher Scientific). Following 24h LiCl treatment, cells were fixed in 3.7% formaldehyde for 10 minutes. Cells were incubated overnight in primary antibodies (sc-13067; Santa Cruz Biotechnology, Santa Cruz, CA, USA) GSK3b (9315; Cell Signaling Technologies, Boston, MA), serine 9 phospho-GSK3b (9336; Cell Signaling Technology), alpha-tubulin (T6199; Sigma Aldrich)), and Tomm20 (ab 56783; Abcam). Cellular distribution of proteins was visualized using fluorescent-tagged secondary antibodies (FI-2000, FI-1000; Vector Laboratories) USA. F-actin was visualized using Rhodamine Phalloidin (PDHR1; Cytoskeleton Inc, Denver, CO, USA). Nuclei were visualized using Hoechst Solution (62249; Thermo Fisher Scientific). All images were captured using uniform exposure settings on a Leica DM4000B microscope (Leica Microsystems, Wetzlar, Germany) and photographed with a Retiga 4000R digital camera (QImaging Systems, Surrey, BC, Canada)

Multiphoton laser scanning Microscopy

Immediately prior to multiphoton imaging, cells were fixed for 10 minutes with formalin and mounted onto glass coverslips using Vectashield (Vector Labs) hard-mount mounting solution. Cryostat sections were dried onto glass coverslips and mounted using Clear-mount mounting solution (Thermo Fisher Scientific). The instrument response function of the optical system was calibrated before each imaging session. A Nikon CFI Plan Apo 60x lens (Melville, NY, USA) was used for all imaging. Data were collected using an excitation wavelength of 780 nm, and emission was filtered at 457 ± 50 nm, the spectral peak for NADH/NADPH. The data collection time was 120 s using a pixel frame size of 256 × 256. The system has multiple detectors including a 16 channel combined spectral lifetime detector (utilizes a Hamamatsu PML-16 PMT), detection range 350 to 720 nm, and a H7422P GaAsP photon counting PMT (Hamamatsu) for intensity and

lifetime imaging. Acquisition was performed with WiscScan, a LOCI developed acquisition package software. Autofluorescence intensity and fluorescence lifetime data were analyzed in SPCImage (Becker & Hickl, v.3.9.7, Berlin, Germany) where a Levenberg–Marquardt routine for nonlinear fitting was used to fit the fluorescence decay curve collected for each pixel in the 256 × 256 frame to a model multi-exponential decay function. Data were assessed by the minimized chi-square value generated during the fit so that analysis was unbiased. To eliminate background fluorescence a threshold for analysis was applied based on photon counts. Additionally, pixels were assigned a bin of 2 for optimal fitting of the data. For NAD(P)H autofluorescent intensity, data were analyzed in ImageJ (NIH, Wayne Rasband; https://imagej.nih.gov/ij/) and regions were defined by cellular compartment or hippocampal region. For fluorescence lifetime, regions of interest were defined by the same criteria using the inclusion tool in SPC image.

Histochemistry and Immunodetection

Serial cryostat sections 10 μm in thickness were cut at −14°C with a Leica Cryostat, defrosted and air-dried, and stained for cytochrome *c* oxidase enzymatic activity as previously described[12]. For each experiment, tissues were sliced, batches were processed, and data were captured start to finish within 24 h. Immunodetection of PGC1a and GSK3b was conducted as previously described[12]. following antigen retrieval on 10μm cryosections (mouse) tissues. Antibodies and reagents used are as follows: biotinylated anti-mouse Ig (BA-9200; Vector Labs, Burlingame, CA, USA) or biotinylated anti-rabbit IgG (BA-1000; Vector Labs), peroxidase-labeled avidin biotin complex (ABC) solution (PK-6200; Vector Labs), ImmPACT NovaRED reagent (SK-4805; Vector Labs), PGC1a (sc-13067; Santa Cruz Biotechnology), total GSK3b (9315; Cell Signaling Technology), serine 9 phospho-GSK3b (9336; Cell Signaling Technology). With the exception of the multiphoton imaging, stained slides were imaged with a Leica Microsystems DM4000B microscope and photographed with a Retiga 4000R digital camera (QImaging Systems, Surrey, BC, Canada). Camera settings were optimized for each stain; for uniformity, all images for a given

stain were taken on the same day with identical settings, fixed light levels, and fixed shutter speed optimized at each magnification. Digital images were converted from color to monochrome and inverted, so that greater stain intensity is shown as brighter pixels. All image analysis was performed using Adobe Photoshop (Adobe Systems, San Jose, CA, USA). Stain intensity was measured using either the rectangular marquee tool or the lasso outline tool in the hippocampal region of interest. Within each region for each stain, the size of the capture box was uniform with an average inclusion of ~30K pixels.

Quantification and Statistical Analysis

Independent Student's t test and ANOVA with post hoc analyses were used to evaluate statistical significance in all cell culture studies. Statistical analyses for the hippocampal immunohistochemistry and MPLSM-FLIM was conducted as previously described[12]. Briefly, to account for the dependence among observations due to multiple measurements per animal, we performed linear mixed models (LMM) assuming a compound symmetric covariance structure using SAS PROC MIXED[33]. The LMMs included full factorial with Type 3 tests of the main effects and interactions. To explore the lithium carbonate dosage-by-region interaction, simple main effects were investigated to determine whether there were dosage effects within each region. We employed no formal multiple testing correction. Instead, consistent with published guidelines for statistical reporting[34], exact p values are reported. All data are reported as mean ± SEM.

REFERENCES

1 Anderson, R. M. & Weindruch, R. Metabolic reprogramming, caloric restriction and aging. *Trends Endocrinol Metab* **21**, 134-141, doi:S1043-2760(09)00194-5 [pii] 10.1016/j.tem.2009.11.005 (2010).

2 Barger, J. L. *et al.* A Conserved Transcriptional Signature of Delayed Aging and Reduced Disease Vulnerability Is Partially Mediated by SIRT3. *PLoS One* **10**, e0120738, doi:10.1371/journal.pone.0120738 (2015).

3 Colman, R. J. *et al.* Caloric restriction reduces age-related and all-cause mortality in rhesus monkeys. *Nat Commun* **5**, 3557, doi:10.1038/ncomms4557 (2014).

4 Fusco, S. & Pani, G. Brain response to calorie restriction. *Cell Mol Life Sci* **70**, 3157-3170, doi:10.1007/s00018-012-1223-y (2013).

5 Mattson, M. P. & Arumugam, T. V. Hallmarks of Brain Aging: Adaptive and Pathological Modification by Metabolic States. *Cell Metab* **27**, 1176-1199, doi:10.1016/j.cmet.2018.05.011 (2018).

6 Camandola, S. & Mattson, M. P. Brain metabolism in health, aging, and neurodegeneration. *Embo j* **36**, 1474-1492, doi:10.15252/embj.201695810 (2017).

7 Scahill, R. I. *et al.* A longitudinal study of brain volume changes in normal aging using serial registered magnetic resonance imaging. *Arch Neurol* **60**, 989-994, doi:10.1001/archneur.60.7.989 (2003).

8 Martin, B., Mattson, M. P. & Maudsley, S. Caloric restriction and intermittent fasting: two potential diets for successful brain aging. *Ageing Res. Rev.* **5**, 332-353 (2006).

9 Colman, R. J. *et al.* Caloric restriction delays disease onset and mortality in rhesus monkeys. *Science* **325**, 201-204, doi:325/5937/201 [pii] 10.1126/science.1173635 (2009).

10 Willette, A. A. *et al.* Calorie restriction reduces the influence of glucoregulatory dysfunction on regional brain volume in aged rhesus monkeys. *Diabetes* **61**, 1036-1042, doi:db11-1187 [pii] 10.2337/db11-1187 (2012).

11 Souder, D. C. & Anderson, R. M. An expanding GSK3 network: implications for aging research. *Geroscience*, doi:10.1007/s11357-019-00085-z (2019).

12 Martin, S. A. *et al.* Regional metabolic heterogeneity of the hippocampus is nonuniformly impacted by age and caloric restriction. *Aging Cell* **15**, 100-110, doi:10.1111/acel.12418 (2016).

13 Kenyon, C. The plasticity of aging: insights from long-lived mutants. *Cell* **120**, 449-460 (2005).

14 Burns, J. M. *et al.* Peripheral insulin and brain structure in early Alzheimer disease. *Neurology* **69**, 1094-1104, doi:10.1212/01.wnl.0000276952.91704.af (2007).

15 Guo, S. Insulin signaling, resistance, and the metabolic syndrome: insights from mouse models into disease mechanisms. *J Endocrinol* **220**, T1-t23, doi:10.1530/joe-13-0327 (2014).

16 Ben-Sahra, I. & Manning, B. D. mTORC1 signaling and the metabolic control of cell growth. *Curr Opin Cell Biol* **45**, 72-82, doi:10.1016/j.ceb.2017.02.012 (2017).

17 Goyal, M. S. *et al.* Loss of Brain Aerobic Glycolysis in Normal Human Aging. *Cell Metab* **26**, 353-360.e353, doi:10.1016/j.cmet.2017.07.010 (2017).

18 Baker, L. D. *et al.* INSULIN RESISTANCE IS ASSOCIATED WITH ALZHEIMER-LIKE REDUCTIONS IN REGIONAL CEREBRAL GLUCOSE METABOLISM FOR COGNITIVELY NORMAL ADULTS WITH PRE-DIABETES OR EARLY TYPE 2 DIABETES. *Arch Neurol* **68**, 51-57, doi:10.1001/archneurol.2010.225 (2011).

19 Manning, B. D. & Toker, A. AKT/PKB Signaling: Navigating the Network. *Cell* **169**, 381-405, doi:10.1016/j.cell.2017.04.001 (2017).

20 O'Grady, J. P. *et al.* Elevated Insulin and Insulin Resistance are Associated with Altered Myelin in Cognitively Unimpaired Middle-Aged Adults. *Obesity (Silver Spring)* **27**, 1464-1471, doi:10.1002/oby.22558 (2019).

21 Park, J. S., Davis, R. L. & Sue, C. M. in *Curr Neurol Neurosci Rep* Vol. 18 (2018).

22 Shin, J. H. *et al.* PARIS (ZNF746) Repression of PGC1α Contributes to Neurodegeneration in Parkinson's Disease. *Cell* **144**, 689-702, doi:10.1016/j.cell.2011.02.010 (2011).

23 Miller, K. N., Clark, J. P. & Anderson, R. M. Mitochondrial regulator PGC1a-Modulating the modulator. *Curr Opin Endocr Metab Res* **5**, 37-44, doi:10.1016/j.coemr.2019.02.002 (2019).

24 Anderson, R. M. *et al.* Dynamic regulation of PGC1alpha localization and turnover implicates mitochondrial adaptation in calorie restriction and the stress response. *Aging Cell* **7**, 101-111, doi:10.1111/j.1474-9726.2007.00357.x (2008).

25 Olson, B. L. *et al.* SCF Cdc4 acts antagonistically to the PGC1 ␣ transcriptional coactivator by targeting it for ubiquitin-mediated proteolysis. 252-264, doi:10.1101/gad.1624208.cose (2008).

26 Beurel, E., Grieco, S. F. & Jope, R. S. Glycogen synthase kinase-3 (GSK3): regulation, actions, and diseases. *Pharmacol Ther* **148**, 114-131, doi:10.1016/j.pharmthera.2014.11.016 (2015).

27 Cross, D. A., Alessi, D. R., Cohen, P., Andjelkovich, M. & Hemmings, B. A. Inhibition of glycogen synthase kinase-3 by insulin mediated by protein kinase B. *Nature* **378**, 785-789, doi:10.1038/378785a0 (1995).

28 Weber, B. & Barros, L. F. The Astrocyte: Powerhouse and Recycling Center. *Cold Spring Harb Perspect Biol* **7**, doi:10.1101/cshperspect.a020396 (2015).

29 Houtkooper, R. H., Pirinen, E. & Auwerx, J. Sirtuins as regulators of metabolism and healthspan. *Nat Rev Mol Cell Biol* **13**, 225-238, doi:nrm3293 [pii] 10.1038/nrm3293 (2012).

30 Canto, C. & Auwerx, J. PGC1alpha, SIRT1 and AMPK, an energy sensing network that controls energy expenditure. *Curr Opin Lipidol* **20**, 98-105, doi:10.1097/MOL.0b013e328328d0a4 00041433-200904000-00004 [pii] (2009).

31 Hirschey, M. D., Shimazu, T., Huang, J. Y., Schwer, B. & Verdin, E. SIRT3 regulates mitochondrial protein acetylation and intermediary metabolism. *Cold Spring Harb Symp Quant Biol* **76**, 267-277, doi:10.1101/sqb.2011.76.010850 (2011).

32 Qin, W. *et al.* Neuronal SIRT1 activation as a novel mechanism underlying the prevention of Alzheimer disease amyloid neuropathology by calorie restriction. *J Biol Chem* **281**, 21745-21754, doi:10.1074/jbc.M602909200 (2006).

33 Littell, R., Milliken, G., Stroup, W., Wolfinger, R. & Schabenberger, O. *SAS system for mixed models*. 2 edn, (SAS Institute, Inc., 2006).

34 Saville, D. J. Multiple Comparison Procedures - the Practical Solution. *American Statistician* **44**, 174-180, doi:Doi 10.2307/2684163 (1990).

Figure 2.1

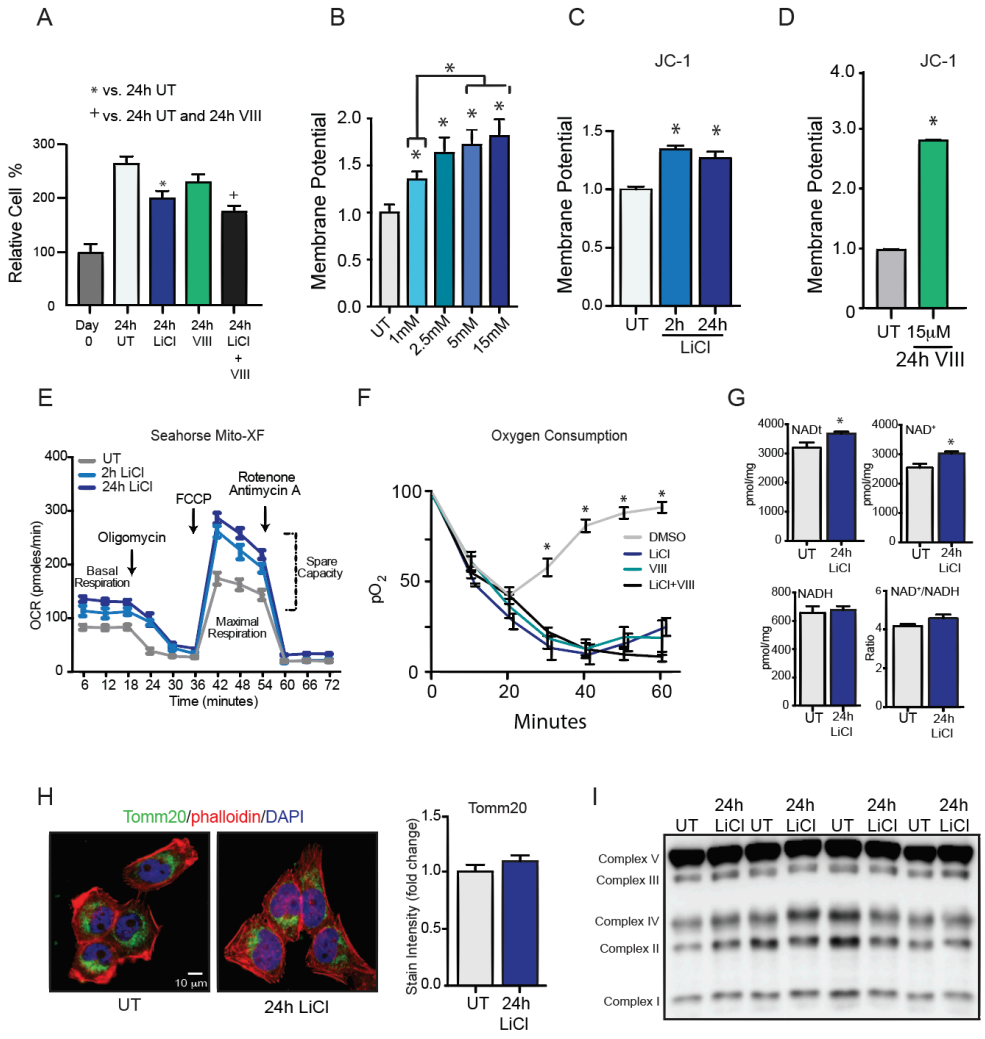

Figure 2.1. GSK3b regulates mitochondrial metabolism in H4 cells. (A) Proliferation assay of H4 cells treated with 24h LiCl [15mM], GSK3b inhibitor VIII [15um] or a combination of LiCl and VIII. (B-D) JC-1 measurement of mitochondrial membrane potential following (B) LiCl dose curve (24h). (C) LiCl time-course (D) inhibitor VIII treatment (E) Basal and maximal cellular respiration. (F) Oxygen consumption of LiCl and inhibitor VIII-treated cells (24h) (G) Biochemical detection of NAD^+ and NADH cofactor after 24h LiCl treatment. (H) Immunofluorescent stain of mitochondria (TOMM20), filamentous actin (rhodamine-phalloidin), and DAPI following 24h LiCl treatment. (I) Western blot of ETC complexes I-V following 24h LiCl treatment.

n = 3-6 biological replicates per assay; data are shown as an average ± SEM; *p < 0.05 Student's t test

Figure 2.2

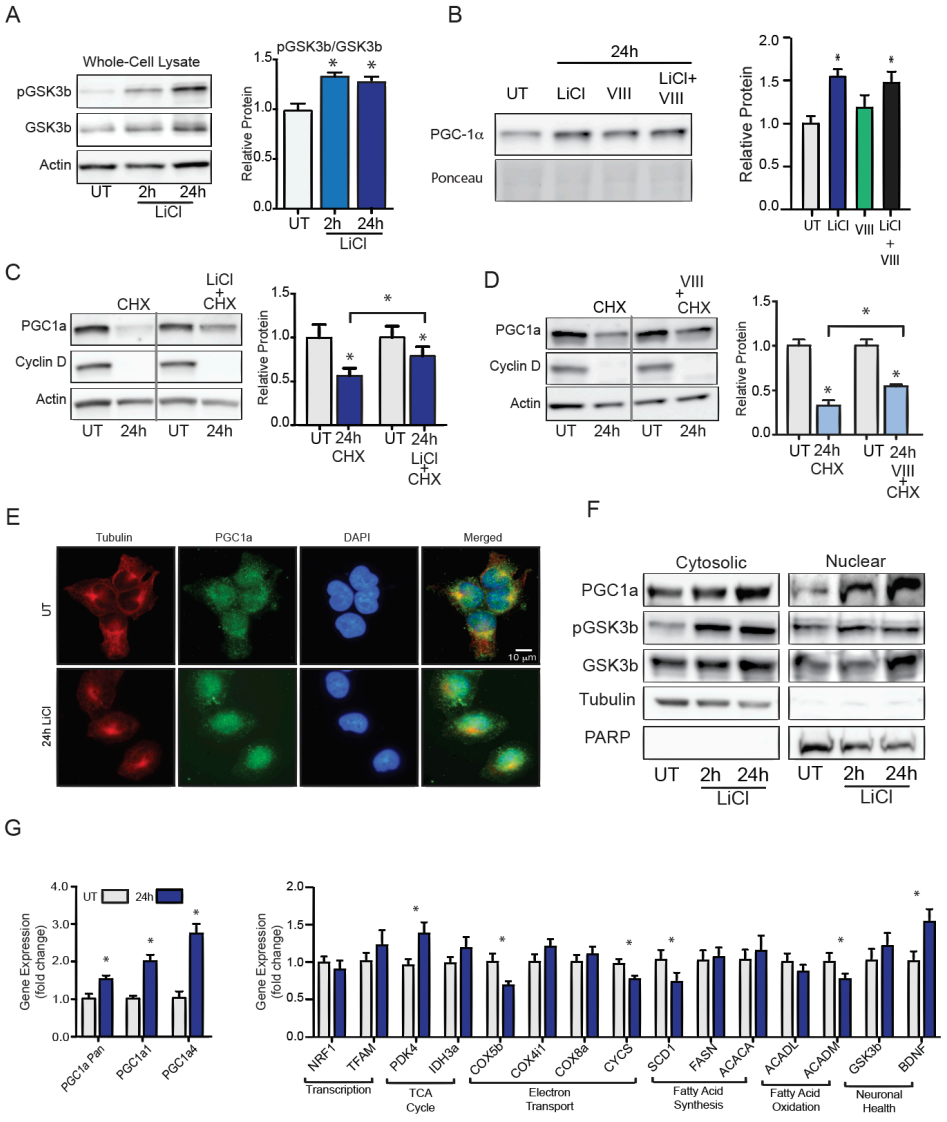

Figure 2.2. GSK3b regulates PGC1a levels, stability, and localization in H4 cells. (A) Western blot of serine-9 pGSK3b, total GSK3b, and actin following 24h LiCl treatment [15mM]. (B) PGC1a levels following 24h LiCl, inhibitor VIII [15uM], and a combination of LiCl and VIII. (C-D) PGC1a, cyclin D, and actin levels following 24h cycloheximide (100uM) in the presence or absence of (C) LiCl [15mM] or (D) inhibitor VIII [15um] (E) Immunofluorescent stain of tubulin and PGC1a following 24h LiCl treatment (40x). (F) Western blot of PGC1a, pGSK3b, and GSK3b in cytosolic/nuclear fractions following LiCl treatment. Nuclear (PARP) and cytosolic (tubulin) controls included. (G) PGC1a transcript levels following 24h LiCl treatment. (H) Transcript levels of PGC1a-target genes following 24h LiCl treatment.

n = 3-6 biological replicates per assay; data are shown as an average ± SEM; *p < 0.05 Student's t test

Figure 2.3

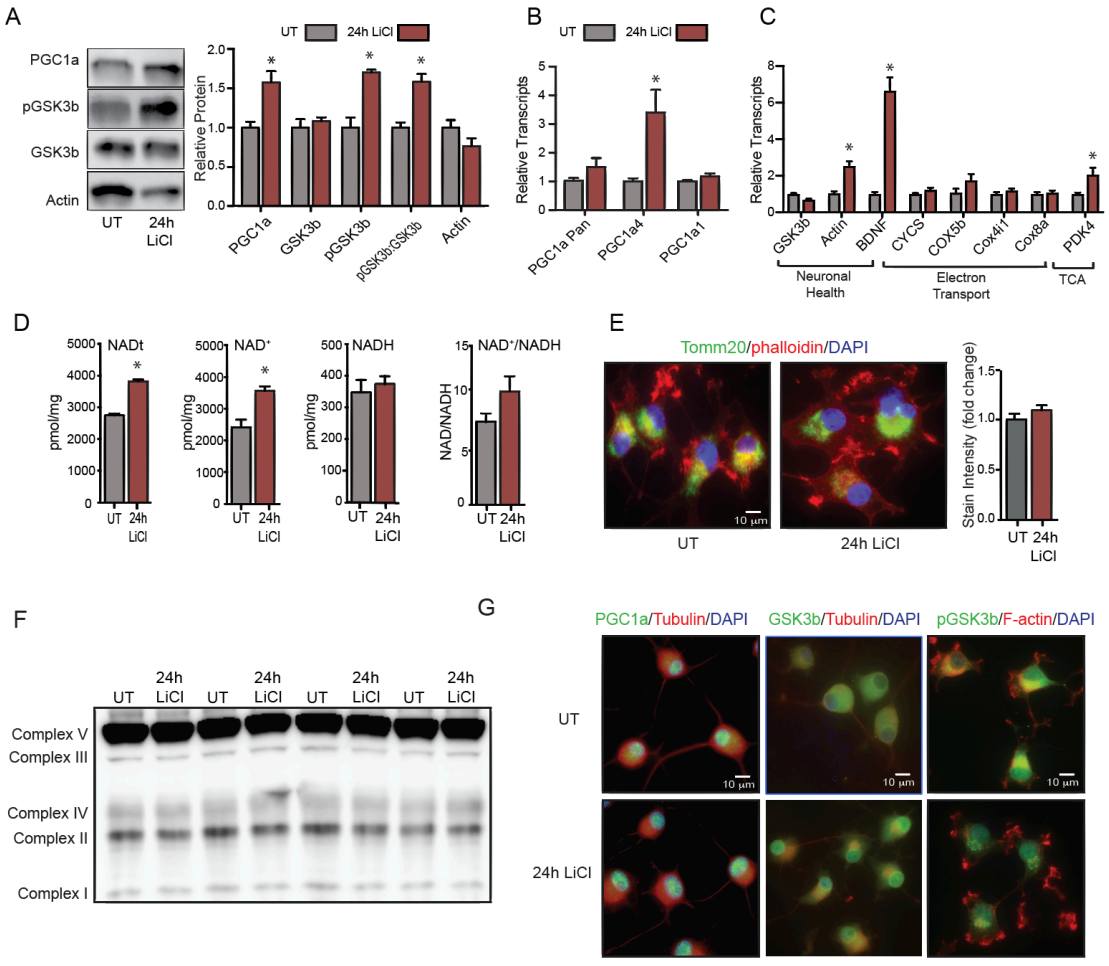

Figure 2.3. GSK3b regulates metabolism and PGC1a in differentiated PC12 cells. (A) Western blot of PGC1a, serine-9 pGSK3b, GSK3b, and actin following 24h LiCl treatment. (B) PGC1a transcript levels following 24h LiCl treatment. (C) Transcript levels of PGC1a-target genes following 24h LiCl treatment. (D) Biochemical detection of NAD^+ and NADH cofactor after 24h LiCl treatment. (E) Immunofluorescent stain of mitochondria (TOMM20), filamentous actin (rhodamine-phalloidin), and DAPI following 24h LiCl treatment (40x). (F) Western blot of ETC complexes I-V following 24h LiCl treatment. (G) Immunofluorescent stain of PGC1a, serine-9 pGSK3b, GSK3b, and tubulin or rhodamine-phalloidin following 24h LiCl treatment.

n = 3-6 biological replicates per assay; data are shown as an average ± SEM; *p < 0.05 Student's t test

Figure 2.4

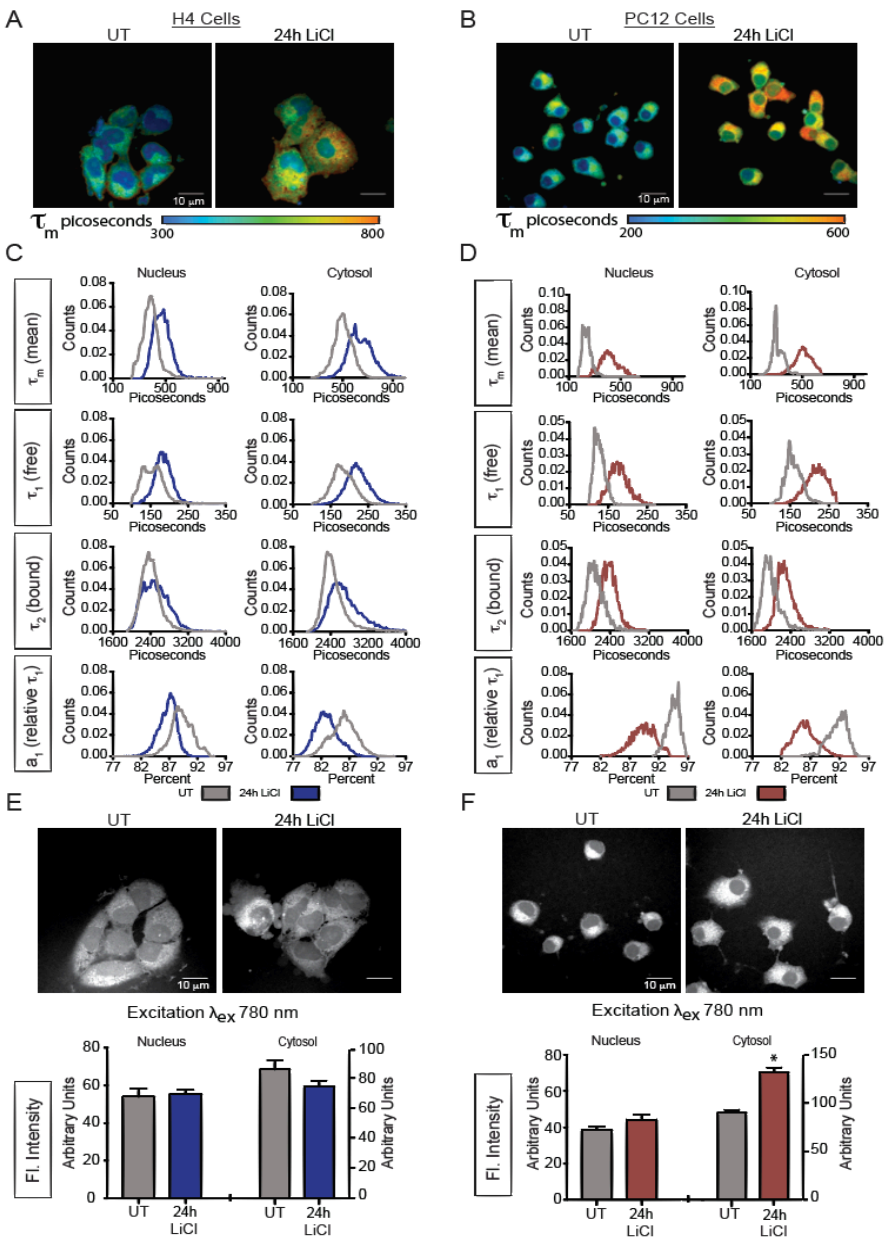

Figure 2.4. GSK3b affects cellular NAD(P)H metabolism (A) Representative images showing mean fluorescence lifetime (τ_m) in picoseconds (ex780nm) in the absence or presence of 24h LiCl [15mM] treatment for (A) H4 glioma and (B) differentiated PC12 cells (60x). (C-D) Distributions of mean fluorescence lifetime tm (top rows), short component t1 (upper middle rows), long component τ_2 (lower middle rows), a1, the relative contribution of τ_1 to τ_m (bottom row) before and after 24h LiCl treatment for (C) H4 glioma and (D) differentiated PC12 cells. (E-F) NAD(P)H fluorescence intensity within the nucleus and cytoplasm following 24h LiCl treatment in (E) H4 glioma and (F) differentiated PC12 cells

n = 6-8 biological replicates per measure; data are shown as a distribution or an average ± SEM; *p < 0.05, linear mixed model

Figure 2.5

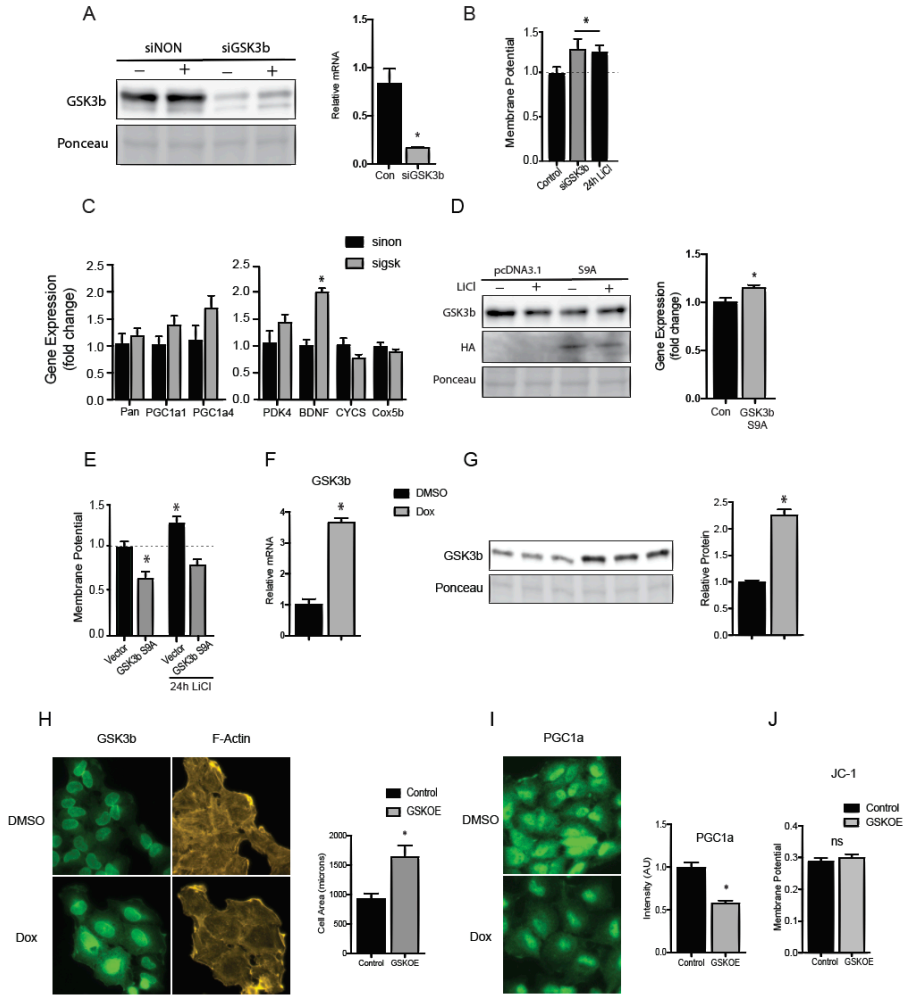

Figure 2.5. The impact of lithium on mitochondrial metabolism is GSK3b-dependent (A) Western blot of GSK3b protein and transcript expression 48h following GSK3b siRNA transfection (B) JC-1 measurement of mitochondrial membrane potential 48h following GSK3b siRNA transfection or 24h LiCl treatment. (C) Transcript levels of PGC1a and PGC1a-target genes 24h following GSK3b siRNA transfection. (D) Western blot of total GSK3b protein and anti-HA epitope 48h following GSK3b[S9A] transfection. (E) JC-1 measurement of mitochondrial membrane potential 48h following GSK3b siRNA transfection and 24h following LiCl treatment. (F) Transcript levels and (G) protein levels of GSK3b following 24h doxycycline [1uM] treatment in H4-pTLxG stable cell line. (H-I) Immunofluorescent stain of (H) GSK3b and filamentous actin (rhodamine-phalloidin) or (I) PGC1a following 24h doxycycline treatment in H4-pTLxG cells (40x); Images correspond to respective quantification of cell area and PGC1a levels. (I) JC-1 measurement of mitochondrial membrane potential.

n = 3-6 biological replicates per assay; data are shown as an average ± SEM; *p < 0.05 Student's t test

Table 2.1

Lifetime Component	**Lithium Main Effect**	**Cellular Compartment Main Effect**	**Lithium x Cellular Compartment Interaction**
τ_m	$F_{(1,24)}$=397.64; p<0.0001*	$F_{(1,24)}$=1442.81; p<0.0001*	$F_{(1,24)}$=39.10; p<0.0001*
τ_1	$F_{(1,24)}$=22.687; p<0.0001*	$F_{(1,24)}$=1065.98; p<0.0001*	$F_{(1,24)}$=20.40; p<0.0001*
τ_2	$F_{(1,24)}$=52.63; p<0.0001*	$F_{(1,24)}$=99.67; p<0.0001*	$F_{(1,24)}$=38.26; p<0.0001*
a_1	$F_{(1,24)}$=351.75; p<0.0001*	$F_{(1,24)}$=2088.94; p<0.0001*	$F_{(1,24)}$=13.10; p<0.0001*
*p<0.05			

Table 2.2

Lifetime Component	**Lithium Main Effect**	**Cellular Compartment Main Effect**	**Lithium x Cellular Compartment Interaction**
τ_m	$F_{(1,20)}$=1347.86; p<0.0001*	$F_{(1,20)}$=1421.16; p<0.0001*	$F_{(1,20)}$=36.90; p<0.0001*
τ_1	$F_{(1,20)}$=753.53; p<0.0001*	$F_{(1,20)}$=1795.27; p<0.0001*	$F_{(1,20)}$=33.72; p<0.0001*
τ_2	$F_{(1,20)}$=367.49; p<0.0001*	$F_{(1,20)}$=230.66; p<0.0001*	$F_{(1,20)}$=0.11; P=0.7461
a_1	$F_{(1,20)}$=1049.76; p<0.0001*	$F_{(1,20)}$=1720.55; p<0.0001*	$F_{(1,20)}$=19.28; p<0.0001*
*p<0.05			

Chapter 3: GSK3b is linked to brain aging and regulates brain metabolism *in-vivo*

Excerpts taken from the following published works:

GSK3b regulates brain energy metabolism
Stephen A. Martin*, Dylan C. Souder*, Karl N. Miller, Josef P. Clark, md Abdul Kader Sagar, Kevin W. Eliceiri, Luigi Puglielli, T. Mark Beasley, and Rozalyn M. Anderson.
*co-first author
Cell Reports. 2018 May 15;23(7): 1922-1931

Stephen A Martin analyzed immunohistochemistry data for lithium-treated mice. Samantha Wright prepared cortical brain homogenates for RNA-seq. Timothy Rhoads conducted pathway analysis of RNA-seq data. Dylan C Souder performed all remaining work.

ABSTRACT

Brain aging is associated with a multitude of cellular and biochemical changes that coincide with functional decline and disease vulnerability. The causative aspects of central nervous system decline remain unclear; however, at the systemic level growth signaling integrity and metabolic regulation have been linked to longevity. GSK3b is a growth signaling-sensitive kinase linked to metabolic regulation and delayed-aging by calorie restriction (CR). In this study, we investigate the relationship between endogenous GSK3b protein levels in the brain and cortical gene expression in mice as a function of age, and the relationship between GSK3b and brain energy metabolism *in vivo* through treatment of mice with the GSK3b inhibitor lithium. Aging was associated with an increase in hippocampal GSK3b protein. RNA-seq analysis confirmed that age-related increases in GSK3b abundance were associated with enrichment of WNT signaling pathways at the transcriptional level. In addition, aging induced changes in pathways linked to NAD(P)H metabolism. To directly test the impact of GSK3b on brain metabolism young mice were treated with GSK3b inhibitor lithium carbonate. Multiphoton imaging of NAD(P)H *in situ* confirmed a role for GSK3b in regulation of brain metabolism, where lithium treatment enhanced the protein-bound pool of hippocampal NAD(P)H, increased PGC1a levels, and cytochrome c oxidase enzyme activity. RNA-seq of cortex from lithium treated mice further support a role for GSK3b at the intersection of growth and metabolic networks in the brain.

At the transcriptional level, multiple transcription factors were enriched between lithium doses. Furthermore, the impact of lithium dose on the outcome measures in this study were nonlinear. We conclude that GSK3b is a key node in brain aging that could be targeted to preserve mitochondrial function.

INTRODUCTION

GSK3b has been implicated in the pathology of age-related diseases including cancer, diabetes, and Alzheimer's disease (AD)[1]. One of the major obstacles in identifying potential mechanisms for GSK3b in disease is the lack of an integrated understanding of how GSK3b influences biological systems. Over 70 *in-vivo* GSK3b substrates have been identified with diverse roles in cellular function[2]. Furthermore, GSK3b signaling is coupled to specialized pathways that are tissue and cell-type specific[3]. Hypothesis-driven studies have been successful in identifying specific roles for GSK3b in biological processes; however, manipulation of GSK3b induces broad changes to model systems that cannot be comprehensively assessed *a-priori*. Next-generation sequencing (NGS) is a high-throughput, high-sensitivity tool to assess global changes in mRNA expression in biological studies[4]. This technique is particularly useful in associating specific phenotypes in a study to patterns in gene expression that can inform of functional changes, including potential regulatory factors responsible for broader functional outcomes. This unbiased approach provides a snap shot of tissue status and can be used to identify the responsive pathways as a function of treatment or age. The data can be interrogated to discover linked networks, but also to take a hypothesis-building approach to ask if GSK3b, or any factor for that matter, might be linked to the changes identified.

Our lab has previously shown that aging induces a distinct state of brain energy metabolism associated with changes in cellular redox that are cell type and brain region specific[5]. CR reversed age-related changes in redox metabolism in middle-aged mice, and preliminary studies linked these differences to PGC1a and GSK3b. At the protein level, abundance of GSK3b was lower in brains of CR mice. In addition, greater levels of inhibitory serine-9 phosphorylation were also detected. The impact of CR to lower levels of GSK3b and increased inhibitory phosphorylation was conserved in brains of monkeys subject to adult onset CR [5]. Independent experiments in cultured cells have established that GSK3b regulates mitochondrial function and PGC1a protein in multiple contexts[6,7]. These data collectively raise the possibility that GSK3b levels and

activity change in the aging brain, and that this influences the expression energy metabolism genes. The previous chapter of this thesis defines a role for GSK3b in regulating cellular energy metabolism and PGC1a protein (Chapter 2). We hypothesize that this functional relationship is conserved *in-vivo,* particularly in the brain. GSK3b protein is enriched in neurons, where it plays a variety of neuron-specific roles including the regulation of synaptic plasticity and neurodevelopment[8,9]. The following two-part study links GSK3b to changes in the cortical metabolism and in the transcriptome identified through RNA sequencing, both as a function of age and in response to *in vivo* inhibition of GSK3b.

RESULTS

Aging increases levels of brain GSK3b and is associated with changes in growth and metabolism

To determine how GSK3b protein levels are impacted during normative aging, we used frozen brain specimens from male mice of 10, 20, or 30 months of age. Mice were maintained on standard diet fed at 95% of ad libitum amounts to avoid obesity. GSK3b protein levels were quantified by immunohistochemistry. Consistent with our prior studies of CR[5], GSK3b levels displayed region and cell-type specificity in the hippocampus (Fig.3.1A). The highest levels of GSK3b were observed in neurons of the polymorphic layer (PL) and the somato-dendritic compartment of granular cell layer (GCL) neurons. An increase in GSK3b levels with age was detected in these regions, and a main-effect of age on GSK3b abundance was significant (n=4-6 per group; p=0.0026) (Fig.3.1B). To investigate molecular changes in tissues from these same mice we conducted unbiased global gene expression profiling. RNA-sequencing of cortical tissue yielded approximately 15000 unique transcripts across the three age-groups. Differential expression of unique transcripts was quantified using edgeR[10]. Focusing on differences between brain specimens from 10 and 30-month-old mice, age was associated with the differential expression of 470 transcripts after multiple testing correction (Benjamini Hochberg with FDR<0.05) (Fig.3.1C). We subsequently performed over-representation analysis (ORA) for significantly altered transcripts using

gene-ontology (GO) terms for molecular function. ORA identified pathways involved in metabolism, immune function, and cell structure as significantly different as a function of age. Notably, NADH oxidase metabolism pathways and WNT receptor pathways (in which GSK3b is a known factor) were the most significantly enriched (Fig.3.1D). The identification of redox pathways as being age-responsive in our transcriptional data is consistent with our prior study that used multiphoton imaging to identify a role of NAD(P)H redox in the aging brain[5]. Altogether, these data show that age-related increases in GSK3b protein levels are associated with alterations in growth and metabolic pathways in the brain, with one of the top age-regulated pathways being one that directly involves GSK3b.

GSK3b is a regulator of brain energy metabolism in vivo

The previous chapter of this thesis describes the regulation of energy metabolism by GSK3b using cell culture models (Chapter 2). To determine the impact of GSK3b inhibition *in-vivo,* male C3B6-F1 hybrid mice (n=5-6 per group) were treated with control diet or diet with lithium carbonate (0.6, 1.2, 1.8, or 2.4 mg/kg) for 4 months from 2 months of age. At higher doses, lithium had an impact on body weight even though food intake was identical among all animals of the cohort (Table 3.1). Histochemical staining for cytochrome c oxidase activity revealed cell type and brain region differences in the hippocampus, consistent with our findings in a previous study of an independent cohort of aging mice[5] (Fig.3.2A). Quantitative analysis revealed a main effect of lithium and an interaction between treatment and region, suggesting that lithium induces region-specific alterations in brain energy metabolism. Immunodetection of GSK3b and PGC1a proteins also revealed substantial cell-type and region-specific differences in abundance, again matching our prior report[5] (Fig.3.2B-C). Although a main effect of lithium was not detected, a region by dose interaction was significant in modifying the abundance of these proteins (Table 3.2). The impact of lithium on PGC1a levels was non-linear within responsive regions, where PGC1a was increased in neurons of the PL, GCL, and cell bodies of the CA1 and CA3 regions at 1.2 mg/kg and

1.8 mg/kg (Fig.3.2C). To determine whether the ability of lithium to impact mitochondrial enzyme activity and PGC1a would be associated with changes in NAD(P)H metabolism, hippocampal sections from lithium treated mice were analyzed using multiphoton imaging to quantify NAD(P)H levels and properties. Lithium impacted mean fluorescence lifetime (τ_m) in the GL, PL, and molecular layer (ML), with main effects of region, treatment, and a region by treatment interaction detected (Fig.3.2D-E)(Table 3.3). These data show that GSK3b inhibition with lithium alters brain energy metabolism in vivo and that manipulation of GSK3b is associated with changes in PGC1a protein levels. These data also show that GSK3b connects to diverse aspects of brain metabolism including mitochondrial activity and redox, and that outcomes of GSK3b inhibition are dependent on lithium dose and brain region.

GSK3b inhibition alters gene expression in the brain in a dose-dependent manner

We previously demonstrated that GSK3b inhibition in cultured cells by lithium treatment was associated with enhanced respiration and transcriptional activation of PGC1a regulated genes involved in energy metabolism (Chapter 2)[7]. The data shown above demonstrate that lithium broadly impacts metabolism in vivo, prompting an expansion of the investigation to gene expression. In an exploratory study (n=2 per group; 5 groups), RNA sequencing of cortical tissue from lithium-treated mice detected ~15000 unique transcripts across each of the 5 diet groups (control and 4 lithium doses). Analysis of differentially expressed genes (DEGs) via edgeR[10] revealed a dose-dependent effect of lithium treatment on gene expression, with the greatest number of DEGs found at the highest dose (2.4 mg/kg) (Fig.3.3A). ORA analysis of significantly changing genes between lithium doses showed enrichment of growth signaling and transcriptional pathways (Fig.3.B). Relatively few transcripts were significantly changing across lithium does; however, the over-representation of transcriptional pathways in our analysis raised the possibility that lithium was associated with a specific transcriptional signature. Hierarchical clustering of all significant DEGs between groups revealed a common pattern shared between doses, with similar

numbers of upregulated and downregulated genes (Fig.3.3C). We filtered the dataset to transcripts that were significantly altered at all four doses. Only one gene (mannose receptor C-type 1) was found to be significantly upregulated for all four lithium doses. Nineteen additional transcripts were identified at the higher doses of lithium (1.2-2.4 mg/kg), suggesting that lithium impacts a core set of transcripts at multiple doses (Fig.3.3D). Analysis of the top five significantly induced and repressed transcripts within each dose (log_2 fold-change) revealed that most of these genes were shared between 1.2-2.4 mg/kg treatments. Notably, several transcription factors were part of this group, including Fos, Jun b, Hif3a, Egr4, and NR4a3 (Fig.3.3E). These data show that lithium dose-dependently alters cortical gene expression in young mice. This study is still ongoing, we are increasing the numbers of mice per diet group used for RNA-seq analysis and expect to be able to draw more biology from those data to reveal the extent of GSK3b influence on brain processes.

DISCUSSION

Prior investigations of neuronal GSK3b have linked it to many detrimental phenotypes at the molecular level, including tau hyper-phosphorylation, glial activation, and neurotoxicity[11,12]. Up to this point there have been fewer studies focused on the impact of aging on GSK3b. Here we report an age-associated increase in hippocampal GSK3b protein that suggests GSK3b may play a role in brain aging. Differences in GSK3b levels between cell types and brain regions suggest that the functional consequences of altered GSK3b abundance may differ between these regions. Our data show that GSK3b is highly enriched in neurons. In neurons, independent studies have shown that GSK3b controls synaptic plasticity in a variety of ways, including regulating tubulin dynamics and synaptic vesicle recovery during neuronal activity[13,14]. In light of those findings, the upregulation of GSK3b in hippocampal dendrites in aged mice could produce alterations in neuronal activity and arborization, although we have not investigated this yet. Our data show that GSK3b levels were also numerically greater in the somas of PL and GCL neurons. It has been

well established that GSK3b regulates the activity of numerous transcription factors and chromatin modifiers (Chapter 1), raising the possibility that GSK3b mediates gene expression changes with age[1,2]. Our data suggests that this is indeed the case. Age was associated with the differential expression transcripts associated with diverse pathways in immune function, intermediary metabolism, and cell structure. Intriguingly, the WNT signaling pathway, in which GSK3b is a key factor, was one of the most significantly enriched pathways to come out of this analysis[15]. In other studies, inhibition of GSK3b through either lithium or the WNT-7a ligand has been shown to modulate microtubule dynamics and axon structure[16]. Considering the established role GSK3b plays in both WNT signaling and neuronal function, it is reasonable to suspect that age-related increases in GSK3b contribute directly to the transcriptomic changes in these same pathways that were identified in our study. Moreover, the age-related enrichment of metabolic pathways detected by ORA is consistent with our hypothesis that GSK3b plays a role in brain metabolism.

Corroborating evidence in support of the hypothesis that GSK3b regulates brain energy metabolism comes from our pharmacological study of GSK3b inhibition. Treatment of mice with various doses of the GSK3b inhibitor lithium resulted in upregulation of PGC1a protein, increased cytochrome c oxidase activity, and enhancement of the protein-bound pool of NAD(P)H cofactor. Collectively, these data demonstrate a profound impact of GSK3b on metabolism in the hippocampus. The directionality of lithium-induced changes in brain metabolism matches those observed in lithium-treated cells (Chapter 2), paving the way for complimentary mechanistic studies in cell culture. Our previous studies have uncovered a decline in mitochondrial metabolism with brain aging in mice, which may be connected to observations in other studies that report mitochondrial insufficiency associated with diseases of age including AD and PD[5,17]. Collectively these findings suggest that GSK3b could be an effective target to delay or prevent age-related loss in metabolic integrity. In support of this idea, lithium has been shown to extend lifespan in worms and flies through mechanisms linked to transcriptional and metabolic pathways [18,19].

More direct evidence for a role for GSK3b in brain metabolism comes from transcriptional data generated from the cortices of lithium-treated mice. Here we uncovered dose-dependent changes in gene expression. The impact of lithium was the greatest with 2.4 mg/kg treatment; however, a core set of lithium responsive transcripts were conserved from 1.2 to 2.4 mg/kg. The absence of these shared genes in the 0.6 mg/kg dose indicates there may be thresholds for different aspects of GSK3b function, where distinct substrates of GSK3b kinase activity are differentially sensitive to GSK3b inhibition. The concept of layered sensitivities among GSK3b substrates is supported by our measurements of hippocampal metabolism, which demonstrate that outcome measures differed by dose in their peak response to lithium among regions. Importantly, transcription factors were over-represented in the shared response to lithium. Two of these transcription factors, Fos and Jun b , are directly regulated at the protein-stability level by GSK3b[2]. As members of the AP-1 family of transcription factors, these genes play broad roles in cell survival, growth, and differentiation. Recently, AP-1 transcription factors have been implicated in a positive feedback loop involving the BDNF/TrkB signaling axis, placing GSK3b upstream of neuron survival and plasticity[20]. Despite these promising leads, the presence of diverse cell populations in cortical tissue makes it challenging to delineate transcriptional responses between cell types. Emerging single-cell RNA sequencing technology or laser-capture microdissection of specific brain regions will be useful in future studies to identify cell-type and region-specific effects of lithium.

In summary, we have demonstrated that age-related increases in GSK3b protein levels in mice are associated with a transcriptional signature specifically linked to GSK3b signaling and to its newly-defined role in energy metabolism regulation. In young mice, treatment with the GSK3b inhibitor lithium alters hippocampal energy metabolism in a dose-dependent manner, and induces transcriptomic changes that implicate growth pathways. These results implicate GSK3b in brain aging and suggest that GSK3b related processes are part of the increase in disease vulnerability

as a function of age. We conclude that GSK3b biology is not only worthy of in depth-investigation, but that it could be a useful target for interventions to ameliorate age-related functional decline.

METHODS

Animals

Aging Study

Six-week-old male B6C3F1 hybrid mice were obtained from Harlan Laboratories (Madison, WI, USA) and housed under controlled pathogen-free conditions in accordance with the recommendations of the University of Wisconsin Institutional Animal Care and Use Committee. For the aging study, mice were fed 87 kcal week^{-1} of control diet (Bio-Serv diet #F05312) from 2 months of age and were individually housed. This level of calorie intake is ~95% of *ad libitum* for the B6C3F1 strain so all food was consumed. By 30 months of age, mortality of the control animals was ~45%, consistent with the expected lifespan for this strain. Mice were euthanized by cervical dislocation at 10, 20, and 30 months of age. Brains were isolated, bisected, embedded in OCT, frozen in liquid nitrogen, and stored at −80°C until further processing.

Lithium Study

Six-week-old male B6C3F1 hybrid mice were obtained from Harlan Laboratories (Madison, WI, USA) and housed under controlled pathogen-free conditions in accordance with the recommendations of the University of Wisconsin Institutional Animal Care and Use Committee. Mice were fed 87 kcal week^{-1} of control diet (F05312; Bio-Serv, Flemington, NJ, USA) and were individually housed with *ad libitum* access to water. This level of food intake is ~95% *ad libitum* for the B6C3F1 strain so all food was consumed. Following two weeks of facility acclimation, mice were randomized into five treatment groups fed the control diet supplemented with increasing concentrations of dietary lithium carbonate (2 months old; n = 10/group): Group 1) 0.0 g/kg/day Li_2CO_3; Group 2) 0.6 g/kg/day Li_2CO_3; Group 3) 1.2 g/kg/day Li_2CO_3; Group 4) 1.8 g/kg/day Li_2CO_3; Group 5) 2.4

g/kg/day Li_2CO_3. Li_2CO_3 supplemented mice were administered an additional drinking bottle containing saline (0.45% NaCl) to offset polyuria, a common side effect of lithium treatment. Mice consumed dietary lithium for 4 months, and were euthanized at 6 months of age. Brains were isolated, bisected, embedded in OCT, frozen in liquid nitrogen, and stored at −80°C until further processing.

Transcriptomics

Brain punches were homogenized using TRIzol reagent. RNA extraction proceeded using a Direct-zol RNA kit (Zymo Research, Irvine, CA) according to the manufacturer's instructions. Purified total RNA was then used to generate mRNA-sequencing libraries using NEBNext Poly(A) mRNA Magnetic Isolation Module and NEBNext Ultra RNA Library Prep kit for Illumina (Illumina Inc., San Diego, California, USA). Libraries were then submitted to the University of Wisconsin-Madison Biotechnology Center Sequencing Facility for high throughput RNA-Seq.

Immunohistochemistry

Serial cryostat sections 10 μm in thickness were cut at −14°C with a Leica Cryostat, defrosted and air-dried, and stained for cytochrome c oxidase enzymatic activity as previously described[5]. For each experiment, tissues were sliced, batches were processed, and data were captured start to finish within 24 h. Immunodetection of PGC1a and GSK3b was conducted as previously described following antigen retrieval on 10-μm cryosections (mouse) tissues[5]. Antibodies and reagents used are as follows: biotinylated anti-mouse Ig (BA-9200; Vector Labs, Burlingame, CA, USA) or biotinylated anti-rabbit IgG (BA-1000; Vector Labs), peroxidase-labeled avidin biotin complex (ABC) solution (PK-6200; Vector Labs), ImmPACT NovaRED reagent (SK-4805; Vector Labs), PGC1a (sc-13067; Santa Cruz Biotechnology), total GSK3b (9315; Cell Signaling Technology). With the exception of the multiphoton imaging, stained slides were imaged with a Leica Microsystems DM4000B microscope and photographed with a Retiga 4000R digital camera (QIm-

aging Systems, Surrey, BC, Canada). Camera settings were optimized for each stain; for uniformity, all images for a given stain were taken on the same day with identical settings, fixed light levels, and fixed shutter speed optimized at each magnification. Digital images were converted from color to monochrome and inverted, so that greater stain intensity is shown as brighter pixels. All image analysis was performed using Adobe Photoshop (Adobe Systems, San Jose, CA, USA). Stain intensity was measured using either the rectangular marquee tool or the lasso outline tool in the hippocampal region of interest. Within each region for each stain, the size of the capture box was uniform with an average inclusion of ~30K pixels.

Multiphoton laser scanning Microscopy

Cryostat sections were dried onto glass coverslips and mounted using Clear-mount mounting solution (Thermo Fisher Scientific). The instrument response function of the optical system was calibrated before each imaging session. A Nikon CFI Plan Apo 60x lens (Melville, NY, USA) was used for all imaging. Data were collected using an excitation wavelength of 780 nm, and emission was filtered at 457 ± 50 nm, the spectral peak for NADH/NADPH. The data collection time was 120 s using a pixel frame size of 256 × 256. The system has multiple detectors including a 16 channel combined spectral lifetime detector (utilizes a Hamamatsu PML-16 PMT), detection range 350 to 720 nm, and a H7422P GaAsP photon counting PMT (Hamamatsu) for intensity and lifetime imaging. Acquisition was performed with WiscScan, a LOCI developed acquisition package software. Autofluorescence intensity and fluorescence lifetime data were analyzed in SPCImage (Becker & Hickl, v.3.9.7, Berlin, Germany) where a Levenberg–Marquardt routine for nonlinear fitting was used to fit the fluorescence decay curve collected for each pixel in the 256 × 256 frame to a model multi-exponential decay function. Data were assessed by the minimized chi-square value generated during the fit so that analysis was unbiased. To eliminate background fluorescence a threshold for analysis was applied based on photon counts. Additionally, pixels were assigned a bin of 3 for optimal fitting of the data. For NAD(P)H autofluorescent intensity,

data were analyzed in ImageJ (NIH, Wayne Rasband; https://imagej.nih.gov/ij/) and regions were defined by cellular compartment or hippocampal region. For fluorescence lifetime, regions of interest were defined by the same criteria using the inclusion tool in SPC image.

Statistics

Statistical analyses for the hippocampal immunohistochemistry and MPLSM-FLIM was conducted as previously described[5]. Briefly, to account for the dependence among observations due to multiple measurements per animal, we performed linear mixed models (LMM) assuming a compound symmetric covariance structure using SAS PROC MIXED[21]. The LMMs included full factorial with Type 3 tests of the main effects and interactions. To explore the lithium carbonate dosage-by-region interaction, simple main effects were investigated to determine whether there were dosage effects within each region. We employed no formal multiple testing correction. Instead, consistent with published guidelines for statistical reporting[22], exact p values are reported.

REFERENCES

1 Beurel, E., Grieco, S. F. & Jope, R. S. Glycogen synthase kinase-3 (GSK3): regulation, actions, and diseases. *Pharmacol Ther* **148**, 114-131, doi:10.1016/j.pharmthera.2014.11.016 (2015).

2 Sutherland, C. What Are the bona fide GSK3 Substrates? *Int J Alzheimers Dis* **2011**, 505607, doi:10.4061/2011/505607 (2011).

3 Kaidanovich-Beilin, O. & Woodgett, J. R. GSK-3: Functional Insights from Cell Biology and Animal Models. *Front Mol Neurosci* **4**, 40, doi:10.3389/fnmol.2011.00040 (2011).

4 Schuster, S. C. Next-generation sequencing transforms today's biology. *Nat Methods* **5**, 16-18, doi:10.1038/nmeth1156 (2008).

5 Martin, S. A. *et al.* Regional metabolic heterogeneity of the hippocampus is nonuniformly impacted by age and caloric restriction. *Aging Cell* **15**, 100-110, doi:10.1111/acel.12418 (2016).

6 Anderson, R. M. *et al.* Dynamic regulation of PGC1alpha localization and turnover implicates mitochondrial adaptation in calorie restriction and the stress response. *Aging Cell* **7**, 101-111, doi:10.1111/j.1474-9726.2007.00357.x (2008).

7 Martin, S. A. *et al.* GSK3beta Regulates Brain Energy Metabolism. *Cell Rep* **23**, 1922-1931.e1924, doi:10.1016/j.celrep.2018.04.045 (2018).

8 Grant, C. D. M. GSK3 ␋ Overexpression in Dentate Gyrus Neural Precursor Cells Expands the Progenitor Pool and Enhances Memory. **291**, 8199-8213, doi:10.1074/jbc.M115.674531 (2016).

9 Hooper, C. *et al.* Glycogen synthase kinase-3 inhibition is integral to long-term potentiation. *Eur J Neurosci* **25**, 81-86, doi:10.1111/j.1460-9568.2006.05245.x (2007).

10 Robinson, M. D., McCarthy, D. J. & Smyth, G. K. edgeR: a Bioconductor package for differential expression analysis of digital gene expression data. *Bioinformatics* **26**, 139-140, doi:10.1093/bioinformatics/btp616 (2010).

11 Hernandez, F., Borrell, J., Guaza, C., Avila, J. & Lucas, J. J. Spatial learning deficit in transgenic mice that conditionally over-express GSK-3beta in the brain but do not form tau filaments. *J Neurochem* **83**, 1529-1533 (2002).

12 Engel, T., Hernandez, F., Avila, J. & Lucas, J. J. Full reversal of Alzheimer's disease-like phenotype in a mouse model with conditional overexpression of glycogen synthase kinase-3. *J Neurosci* **26**, 5083-5090, doi:10.1523/jneurosci.0604-06.2006 (2006).

13 Geraldo, S. & Gordon-Weeks, P. R. Cytoskeletal dynamics in growth-cone steering. *J Cell Sci* **122**, 3595-3604, doi:10.1242/jcs.042309 (2009).

14 Clayton, E. *et al.* Dynamin I phosphorylation by GSK3 controls activity-dependent bulk endocytosis of synaptic vesicles. *Nat Neurosci* **13**, 845-851, doi:10.1038/nn.2571 (2010).

15 Klein, P. S. & Melton, D. A. A molecular mechanism for the effect of lithium on development. *Proc Natl Acad Sci U S A* **93**, 8455-8459 (1996).

16 Lucas, F. R., Goold, R. G., Gordon-Weeks, P. R. & Salinas, P. C. Inhibition of GSK-3beta leading to the loss of phosphorylated MAP-1B is an early event in axonal remodelling induced by WNT-7a or lithium. *J Cell Sci* **111 (Pt 10)**, 1351-1361 (1998).

17 Mattson, M. P. & Arumugam, T. V. Hallmarks of Brain Aging: Adaptive and Pathological Modification by Metabolic States. *Cell Metab* **27**, 1176-1199, doi:10.1016/j.cmet.2018.05.011 (2018).

18 McColl, G. *et al.* Pharmacogenetic Analysis of Lithium-induced Delayed Aging in Caenorhabditis elegans * □. **283**, 350-357, doi:10.1074/jbc.M705028200 (2008).

19 Kinghorn, K. J. *et al.* Lithium Promotes Longevity through GSK3 / NRF2- Dependent Hormesis Lithium Promotes Longevity. 638-650, doi:10.1016/j.celrep.2016.03.041 (2016).

20 Tuvikene, J., Pruunsild, P., Orav, E., Esvald, E. E. & Timmusk, T. AP-1 Transcription Factors Mediate BDNF-Positive Feedback Loop in Cortical Neurons. *J Neurosci* **36**, 1290-1305, doi:10.1523/jneurosci.3360-15.2016 (2016).

21 Littell, R., Milliken, G., Stroup, W., Wolfinger, R. & Schabenberger, O. *SAS system for mixed models*. 2 edn, (SAS Institute, Inc., 2006).

22 Saville, D. J. Multiple Comparison Procedures - the Practical Solution. *American Statistician* **44**, 174-180, doi:Doi 10.2307/2684163 (1990).

Figure 3.1

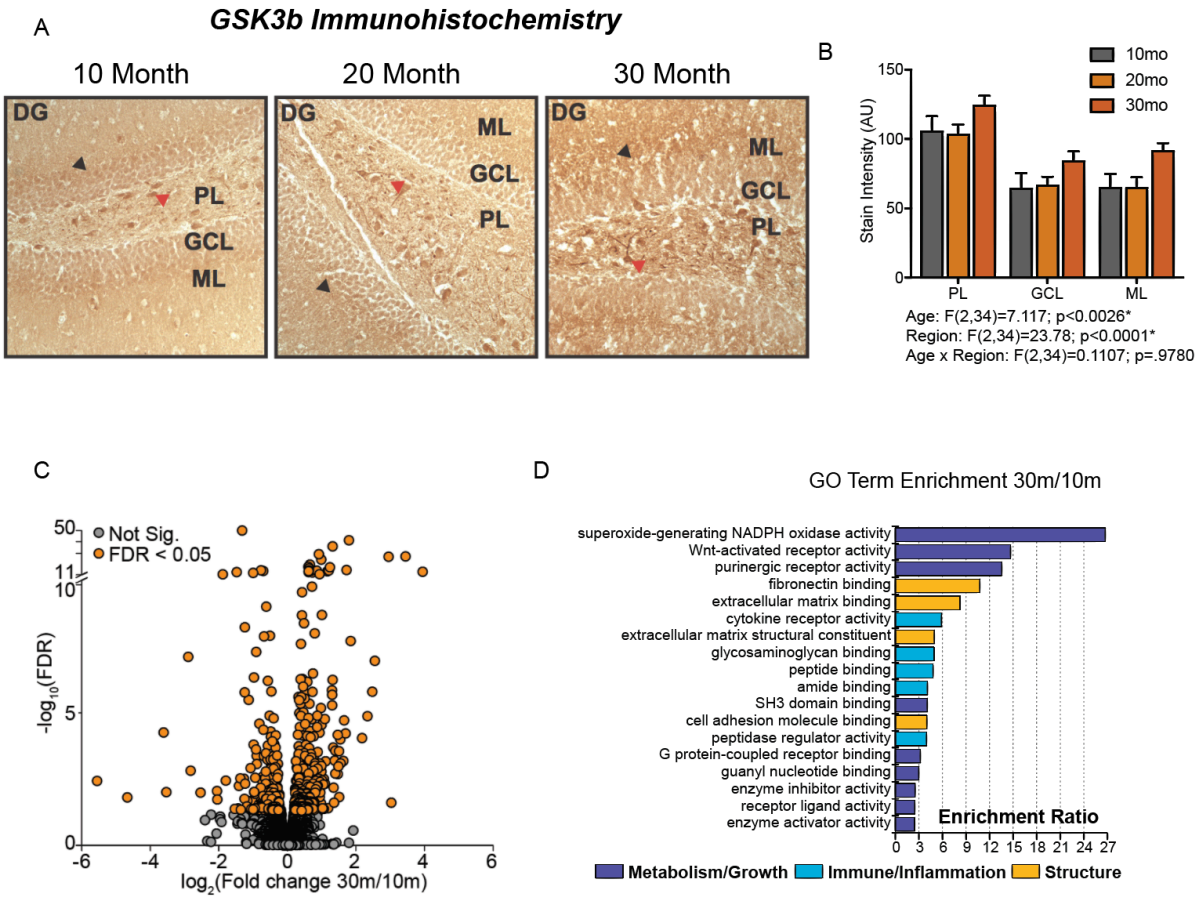

Figure 3.1. Age increases levels of brain GSK3b and is associated with changes in growth and metabolism. (A) Representative images of GSK3b immunodetection in 10, 20, and 30-month-old B6C3F1 mice. Black arrows indicate somato-dendritic enrichment of GSK3b. Red arrows indicate enrichment of GSK3b in polymorphic layer (PL) neurons. (B) Respective quantitation of GSK3b levels in hippocampal regions. (C) Volcano plot of differentially expressed cortical genes between 10 and 30-month-old mice. (D) Pathway enrichment via overrepresentation analysis (ORA) using gene ontology (GO) terms for molecular function.

n = 4-6 mice per age group; data shown as an average ± SEM; *p < 0.05 ANOVA. DG, dentate gyrus; GCL, granular cell layer; PL, polymorphic layer; ML, molecular layer

Figure 3.2

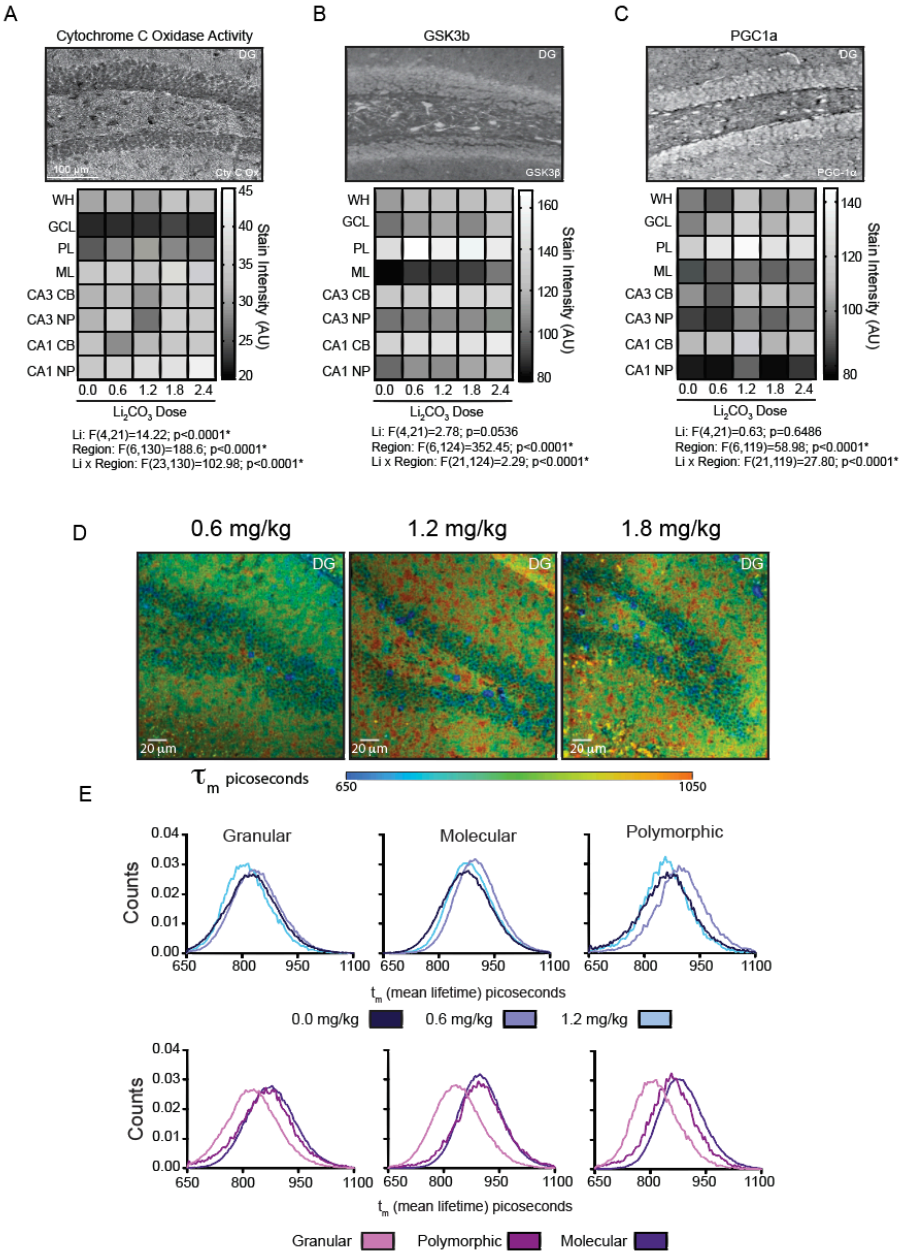

Figure 3.2. GSK3b is a regulator of brain energy metabolism *in vivo*. (A-C) Representative images and quantification of (A) cytochrome c oxidase mitochondrial activity stain (B) GSK3b immunodetection (C) and PGC1a immunodetection in the indicated hippocampal regions from Li_2CO_3 fed mice. (D) Mean fluorescence lifetime (τ_m) of the hippocampus from Li_2CO_3 fed mice with (E) distribution histograms of τ_m between doses and regions.

n = 5–6 mice per Li_2CO_3 dosage; data shown as an average ± SEM or distributions; *p < 0.05, linear mixed models. WH, whole hippocampus; DG, dentate gyrus; GCL, granular cell layer; PL, polymorphic layer; ML, molecular layer; CB, cell bodies; and NP, neuropil.

Figure 3.3

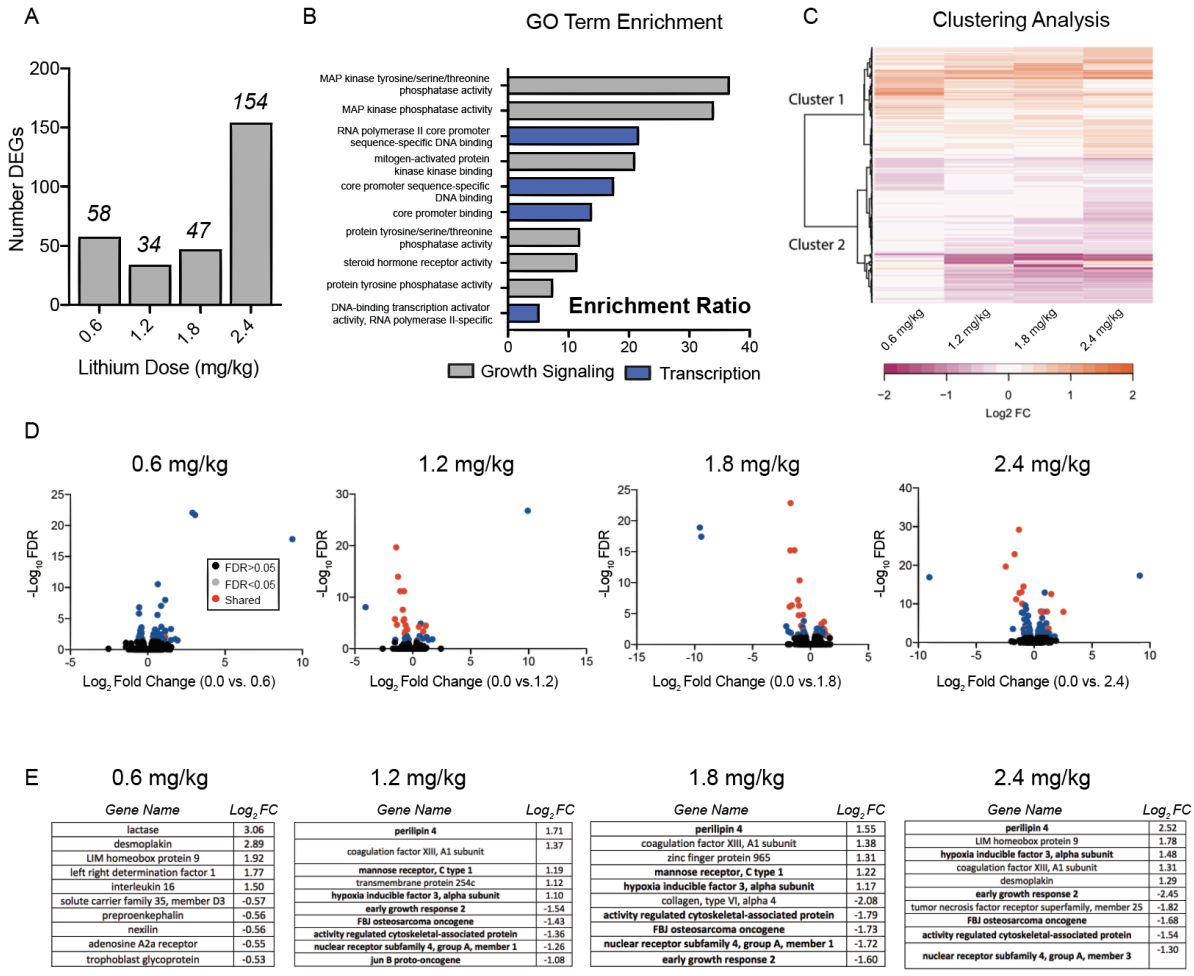

E

0.6 mg/kg

Gene Name	Log_2FC
lactase	3.06
desmoplakin	2.89
LIM homeobox protein 9	1.92
left right determination factor 1	1.77
interleukin 16	1.50
solute carrier family 35, member D3	-0.57
preproenkephalin	-0.56
nexilin	-0.56
adenosine A2a receptor	-0.55
trophoblast glycoprotein	-0.53

1.2 mg/kg

Gene Name	Log_2FC
perilipin 4	1.71
coagulation factor XIII, A1 subunit	1.37
mannose receptor, C type 1	1.19
transmembrane protein 254c	1.12
hypoxia inducible factor 3, alpha subunit	1.10
early growth response 2	-1.54
FBJ osteosarcoma oncogene	-1.43
activity regulated cytoskeletal-associated protein	-1.36
nuclear receptor subfamily 4, group A, member 1	-1.26
jun B proto-oncogene	-1.08

1.8 mg/kg

Gene Name	Log_2FC
perilipin 4	1.55
coagulation factor XIII, A1 subunit	1.38
zinc finger protein 965	1.31
mannose receptor, C type 1	1.22
hypoxia inducible factor 3, alpha subunit	1.17
collagen, type VI, alpha 4	-2.08
activity regulated cytoskeletal-associated protein	-1.79
FBJ osteosarcoma oncogene	-1.73
nuclear receptor subfamily 4, group A, member 1	-1.72
early growth response 2	-1.60

2.4 mg/kg

Gene Name	Log_2FC
perilipin 4	2.52
LIM homeobox protein 9	1.78
hypoxia inducible factor 3, alpha subunit	1.48
coagulation factor XIII, A1 subunit	1.31
desmoplakin	1.29
early growth response 2	-2.45
tumor necrosis factor receptor superfamily, member 25	-1.82
FBJ osteosarcoma oncogene	-1.68
activity regulated cytoskeletal-associated protein	-1.54
nuclear receptor subfamily 4, group A, member 3	-1.30

Figure 3.3. GSK3b inhibition alters gene expression in the brain in a dose-dependent manner. (A) Differentially expressed genes (DEGs) from cortical tissue of Li_2CO_3 fed mice by RNA-sequencing. (B) Pathway enrichment via overrepresentation analysis (ORA) of all DEGs between Li_2CO_3 doses. (C) Clustering analysis of all DEGs between Li_2CO_3 doses. (D) Volcano plots of Li_2CO_3 dose RNA-seq data indicated significantly changing genes (blue) and shared DEGs (red) between all doses or 1.2-2.4 mg/kg doses. (E) Top five upregulated and downregulated DEGs within each dose. Bold text indicates DEGs shared between 1.2-2.4 mg/kg doses.

n = 2 mice per Li_2CO_3 dosage; data shown include genes that passed multiple testing correction (FDR<0.05) between or within doses.

Table 3.1

Li_2CO_3 Dosage (mg/g diet)	Pre-intervention body mass (g)	Post-intervention body mass (g)	Body mass Δ (%)	Post-intervention body fat (%)
0.0	25.74 ± 0.52	36.47 ± 0.7	42.17 ± 3.80	35.08 ± 1.48
0.6	26.31 ± 0.62	37.80 ± 0.7	46.40 ± 3.43	35.05 ± 0.87
1.2	26.02 ± 0.52	37.40 ± 0.89	45.84 ± 4.59	34.42 ± 1.02
1.8	25.92 ± 0.53	32.51 ± 0.81[a]	25.59 ± 2.79[a]	29.02 ± 1.39[a]
2.4	25.82 ± 0.52	26.84 ± 0.52[ab]	4.24 ± 2.50[ab]	21.40 ± 0.42[ab]

Mean ± SEM
[a] $p<0.001$ vs. 0.0, 0.6, 1.2 mg/g dosages; [ab] $p<0.001$ vs. 1.8 mg/g dosage

Table 3.2

Stain	Lithium Dosage Main Effect	Region Main Effect	Dosage x Region Interaction
Cytochrome C Oxidase	$F_{(4,21)}$=14.22; p<0.0001*	$F_{(6,130)}$=188.6; p<0.0001*	$F_{(23,130)}$=102.98; P<0.0001*
PGC1a	$F_{(4,21)}$=0.63; p=0.6486	$F_{(6,119)}$=58.98; p<0.0001*	$F_{(21,119)}$=27.80; p<0.0001*
GSK3b	$F_{(4,21)}$=2.78; p=0.0536	$F_{(6,124)}$=352.45; p<0.0001*	$F_{(21,124)}$=2.29; p<0.0001*

*p<0.05

Table 3.3

Lifetime Component	Lithium Dosage Main Effect	Region Main Effect	Dosage x Region Interaction
τ_m	$F_{(2,13)}$=28.47; p<0.0001*	$F_{(2,13)}$=342.27; p<0.0001*	$F_{(4,13)}$=8.01; P=0.0018*
τ_1	$F_{(2,13)}$=4.05; p=0.0429*	$F_{(2,13)}$=96.65; p<0.0001*	$F_{(4,13)}$=3.81; P=0.0292*
τ_2	$F_{(2,13)}$=9.27; p=0.0032*	$F_{(2,13)}$=14.26; P=0.0005*	$F_{(4,13)}$=2.29; P=0.115
a_1	$F_{(2,13)}$=57.69; p<0.0001*	$F_{(2,13)}$=391.38; p<0.0001*	$F_{(4,13)}$=19.02; p<0.0001*

*p<0.05

Chapter 4: Neuron-specific mechanisms control the metabolic regulator PGC1a

Josef P Clark prepared mRNA-seq libraries for high throughput sequencing at the UW-Madison Biotechnology Center. Timothy Rhodes conducted gene set enrichment analysis for lithium-treated neurons. Tiara Porter from Darcie Moore's lab assisted with the neuronal differentiation experiments. Dylan Souder performed the remaining work presented

ABSTRACT

The role of transcriptional co-activator PGC1a is best characterized in peripheral tissues where it plays a role in adaptation to changes in energy availability or energetic demand. Less is known about how PGC1a is regulated in the brain, although it has been linked to various aspects neuronal function, from energetics to formation of structural processes. Our work has shown that metabolic status is highly cell type and brain region specific; we hypothesize that PGC1a may contribute to this heterogeneity, allowing metabolism to be tuned to cell type. Here we report that astrocytes and neurons differ substantially in metabolic status and in the transcript variants of PGC1a expressed, including the use of a neuron specific promoter. Taking advantage of the ability of GSK3b to influence PGC1a expression, we investigate how transcript variants are differentially regulated in primary neurons and primary astrocytes. Neuronal PGC1a responds robustly to GSK3b inhibition by lithium, switching the dominant promoter, leading to change isoform distribution and abundance. In contrast astrocytic PGC1a is completely refractory to lithium treatment. In neurons, RNA-seq analysis reveals that lithium broadly reprograms transcription and growth signaling status. Moreover, neuronal AMPK and the TrkB/CREB signaling axis are required for differential transcript regulation in response to lithium. The data presented here highlight key mechanisms for neuron-specific metabolic regulation that are likely to be relevant to neurodegenerative diseases and disease vulnerability as a consequence of age.

INTRODUCTION

Cellular energy metabolism is highly malleable, and its regulation is tightly coupled to both internal and external stressors. Mitochondria play a key role in the adaptive response to stress, and our lab has shown that the transcriptional co-activator PGC1a is required for survival following oxidative stress[1]. Multiple lines of evidence now point to a role for PGC1a in integrating and responding to diverse signals, ensuring the cellular metabolic response is matched to the prevailing conditions[2]. Data from our lab implicates mitochondrial pathways in the mechanisms of delayed aging by CR[3], and more recently has confirmed that several hallmarks of CR can be recapitulated in cells by activation of mitochondria[4]. The integration of cellular stress with a mitochondrial response has been proposed as the basis for the link between stress resistance and longevity. The complexity of PGC1a regulation is exemplified by numerous upstream regulators, post-translational modifications, and cell-type and context specific binding partners that fine-tune its co-activator function[2]. Moreover, Ppargc1a gene is expressed as numerous transcript and protein variants that have been associated with different gene target profiles[5]. However, there is a major gap in our understanding of PGC1a regulation and the functional significance of this regulation, particularly in the brain which has an incredible demand for energy. The following introduction describes what is currently known about PGC1a regulation and function in brain cell populations. This thesis chapter defines the mechanisms of PGC1a regulation in neurons, and describes a novel pathway for the activation of neuron-specific PGC1a transcript variants.

PGC1a was first identified as a cold-inducible co-activator that functions in the thermogenic response of brown adipose tissue[6]. It has since been implicated in the response to exercise in skeletal muscle, fasting in the liver, and even metabolic adaptations in certain cancers[7,8]. Several post-translational modifications couple energy demands to PGC1a stability, localization, and activity, and perhaps the best characterized is phosphorylation. PGC1a is phosphorylated and activated by kinases including PKA in liver, p38 MAPK and AMPK in skeletal muscle[7,9]. The insulin-sensitive AKT and spicing regulator Clk2 kinases have been shown to inhibit PGC1a function[2],

and PGC1a is controlled at the stability level by GSK3b[1,10,11]. De-acetylation by SIRT1 activates PGC1a under a variety of circumstances while conversely, acetylation by GCN5 has been shown to repress PGC1a[7]. While neurons utilize similar signaling networks to couple energy demands to energy production, the role of PGC1a in mediating these changes is unknown. We previously identified a role for GSK3b in regulating PGC1a stability (Chapter 2), and GSK3b inhibition with lithium increased mitochondrial respiration in brain cell types[10]. However, it is unclear whether enhanced stability of PGC1a was sufficient to promote the metabolic effects observed in the study. GSK3b has been shown to phosphorylate a range of metabolic and growth regulators with established links to mitochondrial function. Among these regulators are energy sensitive AMPK and TSC2, a modulator of mTORC1 signaling[12]. The established connection between GSK3b and cell-signaling networks raise the possibility that GSK3b coordinates energy metabolism through multiple mechanisms. It is also possible that GSK3b regulates PGC1a function both directly through stability, and indirectly through its impact on intracellular signaling factors associated with PGC1a regulation.

The complexity of PGC1a protein regulation described above extends to transcriptional regulation of the gene encoding Ppargc1a. The gene itself is >140kb and its canonical transcript contains 13 exons and a range of alternate exons that are engaged in different ways to produce different transcript isoforms [5]. PGC1a transcript variants can be expressed from three promoters, each with unique transcription start sites (TSS). These variants exhibit tissue specific expression profiles and are differentially regulated in response to physiological stimuli[5,13,14]. The splicing of Ppargc1a encoded mRNA controls exon usage and can result in truncated PGC1a proteins with functional roles that differ from full-length PGC1a[15,16]. In skeletal muscle, the canonical promoter (CP) of PGC1a1 is regulated preferentially by endurance exercise while transcripts expressed from the alternative promoter (AP) are induced by resistance training[13]. One such transcript, PGC1a4, is a result of alternative splicing and regulates a distinct subset of target genes including IGF1 and myostatin[13,16]. Another distinct splice variant NT-PGC1a is expressed from the AP and

is localized primarily in the cytosol, where it is strongly induced by fasting in the liver and controls gluconeogenic genes[17]. Transcript variation in Ppargc1a derived isoforms is also observed in the brain, which contains PGC1a variants found nowhere else in the body. These variants are expressed off a distinct brain promoter (BP) ~587kb distal to the canonical TSS and are more abundant in brain than the canonical isoform[18]. Recent studies indicate that the brain-specific promoter is uniquely responsive to hypoxia in cells[19]. The functional significance and conditions of recruitment of the brain specific PGC1a isoforms have yet to be elucidated. It is still unclear what mechanisms are engaged that lead to the production of these variants exclusively in the brain.

The precise functional roles of PGC1a in the brain remains poorly characterized; however, PGC1a expression has been linked to the pathology of neurodegenerative disorders. PGC1a null mice display striatal degeneration accompanied by defects in motor coordination[20,21]. Moreover, conditional knockout of PGC1a in striatal neurons results in dopaminergic neuron loss and a decrease in mitochondrial content[22], suggesting a role for PGC1a in Parkinson's disease (PD) pathology. Links between PGC1a and disease have been established indirectly in human populations; polymorphisms in PGC1a are associated with PD risk, and a reduction in PGC1a has been reported in PD brain tissue[22,23] . Mutant huntingtin, the protein responsible for the pathogenesis of HD suppresses PGC1a expression in neurons through a CREB-dependent mechanism. Importantly, lentiviral delivery of PGC1a provided neuroprotection in this study[24], suggesting that maintenance of mitochondrial integrity is protective against neurodegeneration. Failure in mitochondrial function has also been implicated in both neuronal aging and the pathogenesis of AD[25]. Levels of PGC1a mRNA and protein were found to be negatively associated with dementia and the extent of amyloid neuropathology[26]; however, it is unclear whether reductions in PGC1a are a consequence of neuropathology or if these findings represent a primary deficiency in PGC1a related to AD.

As noted above, the mechanisms controlling PGC1a expression are highly specific to the stimulus and cell type under investigation. The connection between PGC1a and neurodegenerative diseases is strong, with mounting evidence from studies in animal models, and in genome wide association studies (GWAS) of human populations. The purpose of this study is to define the regulation of PGC1a transcript variants in primary astrocytes and neurons, which in retaining many *in-vivo* properties of the brain, are a superior model for understanding regulatory mechanisms. Chapter 2 of this thesis describes a mechanism in which GSK3b regulates energy metabolism and indices of PGC1a function in H4 glioma cells and PC12 differentiated neurons. Here, we switch to primary cells and leverage the ability of lithium to alter PGC1a levels and transcriptional activity. We seek to define neuron and astrocyte aspects of PGC1a transcript regulation including alternative promoter usage, transcript stability, and transcription factor regulation. We also utilize neural stem cells to identify the relationship between PGC1a transcript variants and cellular identity. The outcomes here will provide a framework for how PGC1a is regulated in the brain and offer insight into how dysregulation of PGC1a could be targeted in neurodegenerative disease.

RESULTS

Neurons and astrocytes differ in metabolic phenotype and in PGC1a isoform expression

To investigate the regulation of energy metabolism specifically in neurons and astrocytes, we used the fluorescent JC1 dye that allows for quantitative measures of mitochondrial membrane potential. Neurons and astrocytes both displayed high mitochondrial polarization in culture (Fig.4.1A) that was unexpectedly much greater than that of PC12 differentiated neurons and H4 glioma cell culture models reported on in Chapter 2 of this thesis. These data confirm that primary cells are metabolically distinct from cell culture models that are commonly used surrogates. To determine whether indices of redox metabolism were similarly distinct in the primary cells, fixed cells were analyzed by fluorescence lifetime imaging (FLIM) of endogenous NAD(P)H cofactor.

This method (described in Chapter 2) allows for independent assessment of the relative contribution of bound and free NAD(P)H to total NAD(P)H pools. Despite showing similar mitochondrial polarization, neurons and astrocytes differed greatly from each other in mean fluorescence lifetime (τ_m), with neurons displaying much greater τ_m than astrocytes (Fig.4.1B). The FLIM signature of neurons was indicative greater oxidative metabolism relative to astrocytes. This was not unexpected as it has been established that these cell types differ in their reliance on glycolysis to meet energy demands[27].

PGC1a is a key regulator of mitochondrial function and has previously been shown to regulate NADH and NAD(P)H-dependent cellular processes[4]. As alluded to above, brain is unique in producing variants of PGC1a driven from the BP (Fig.4.1C) that contain up to five brain specific exons spliced to canonical exon 2 of the PGC1a gene[18]. Using primers against brain exon 1 and exon 2 (Table 4.1) the transcript variant termed *PGC1a B1E2* was detected. The resulting isoform from this transcript is predicted to share identity with PGC1a1 in most of the functional domains reported for PGC1a[18] (Fig.4.1C). Using qPCR of cortical RNA extracts from mice, PGC1a B1E2 was detected as ~ 8-fold more abundant than canonical full-length PGC1a1 and ~4.5 fold more abundant that the shorter alternative promoter driven PGC1a4 (Fig.4.1D). We next investigated whether differences in metabolism between primary neurons and astrocytes might correspond to cell-type specificity in PGC1a expression. To test this, primary neurons and astrocytes derived from mouse brains were cultured and PGC1a isoforms detected in each cell type by qPCR. The primers used for qPCR were validated for direct comparison of abundance of transcript (Table 4.1). Remarkably, neurons and astrocyte differed completely in PGC1a expression profiles. Neurons displayed ~8-fold greater PGC1a B1E2 levels than PGC1a1 with intermediate expression of PGC1a4 (Fig.4.1E). PGC1a B1E2 was not expressed in astrocytes, rather PGC1a1 was most abundant with a minor contribution from PGC1a4 (Fig.4.1F). Direct comparison between cell types revealed that total PGC1a levels and PGC1a4 were greater in neurons, while PGC1a1 was

greater in astrocytes (Fig.4.1G). Previous studies have demonstrated that PGC1a isoforms, including PGC1a1 and PGC1a4, regulate unique subsets of target genes that differ in the functional outcomes they control[5]. These data show that neurons and astrocytes differ in both metabolic identity, and PGC1a transcript expression. Neurons and astrocytes share a common progenitor, suggesting that expression of PGC1a B1E2 must be specifically activated at some point during neuronal differentiation. In collaboration with Darcie Moore's lab, hippocampal neural stem cells (NSCs) were isolated, differentiated, and sampled at intervals over the 14-day differentiation process. Induction of beta-tubulin III mRNA expression was detected at day 1 and further increased by day 7 confirming NSC differentiation *ex-vivo* (Fig.4.1H). PGC1a B1E2 was expressed at nominal levels in NSCs and increased ~12 fold by day 3 of differentiation and persisted for the remainder of the differentiation process (Fig.4.1I). In contrast, PGC1a1 levels were reduced nearly 2-fold by day 3 and recovered by day 14. A similar trend was detected for PGC1a4 over this same time frame (Fig.4.1J-K). Collectively, these results demonstrate that PGC1a transcript expression profiles are linked to unique metabolic states in neurons and astrocytes. Moreover, PGC1a B1E2 emerges through differentiation and its induction appears to be reciprocal to PGC1a and PGC1a4 expression as neurons commit to their cell fate.

Neurons but not astrocytes are metabolically responsive to lithium treatment

The fact that neurons and astrocytes are metabolically distinct and display unique PGC1a transcript profiles raised the possibility that the impact of GSK3b on PGC1a transcripts and energy metabolism might not be conserved. To test this, primary cells were treated with lithium chloride and transcripts of PGC1a isoforms were detected by qPCR. In neurons, consistent with our prior reports, PGC1a1 and PGC1a4 levels were induced with lithium. In contrast, levels of PGC1a B1E2 were suppressed with lithium treatment, resulting in no overall change in PGC1a abundance (Fig.4.2A). Surprisingly, lithium did not change the abundance of any PGC1a transcript in

astrocytes (Fig.4.2B). Using the JC-1 assay, lithium treatment resulted in a decrease in mitochondrial membrane potential in neurons but no change in astrocytes (Fig.4.2C-D). This is in stark contrast to H4 cells, where lithium treatment enhanced mitochondrial membrane potential (Chapter 2).

To investigate factors involved in the PGC1a isoform switch and concomitant lowering of mitochondrial membrane potential, neuronal extracts were subject to immunodetection of known PGC1a regulatory factors. Western blot analysis detected increased IRS inhibitory phosphorylation in the PI3K binding domain (IRS^{S632}) with lithium treatment, consistent with the ability of lithium to suppress growth (Fig.4.2E). Lithium induced an increase in activating phosphorylation of AMPK ($pAMPK^{T172}$), a PGC1a activator, along with a decrease in activating phosphorylation of AKT ($pAKT^{T308}$) and S6 ($pS6^{S240}$), both PGC1a inhibitors (Fig.4.2E). As previously observed with lithium treatment in cells, levels of $pGSK3b^{S9}$ increased in neurons and immunofluorescent detection of GSK3b in cultured neurons confirmed that lithium induced an increase in nuclear localization of GSK3b (Fig.4.2F). These alterations in signaling are consistent with repression of the PI3K and mTORC1 signaling pathways, with GSK3b at the center of this interwoven growth and metabolism regulatory network.

Quantitative analysis of PGC1a target-transcripts revealed changes in gene expression in lithium-treated neurons, including downregulation of cytochrome c (cycs) and induction of BDNF expression. These gene targets were also responsive to lithium in H4 glioma cells, suggesting that there may be separable cell type-dependent and cell-type independent PGC1a transcriptional programs responsive to GSK3b. The extent of impact of lithium on gene expression was determined through the unbiased approach of RNA sequencing. Following 24 hours of lithium treatment, neuronal RNA extracts were processed to produce sequencing libraries. Approximately 15000 unique transcripts were identified and differential expression was quantified between control and lithium-treated cells. Lithium induced profound changes in gene expression that extended to roughly half of the transcriptome. Notably, we observed induction of numerous transcription

factors including the cAMP-responsive Atf3, Fos, and Dmbx1, a transcription factor involved in neurodevelopment (Fig.4.2H). Functional enrichment of differentially expressed genes was determined through Gene-set enrichment analysis (GSEA) using Gene Ontology (GO) pathways as a reference. Pathways linked to transcription cofactor binding and DNA-dependent transcription-activator activity were significantly enriched, and positively associated with lithium treatment (Fig.4.2I). NAD(P)H metabolism and mitochondrial electron transport were also significantly enriched in this dataset, providing independent corroborating support for the metabolic measures of membrane potential and redox imaging. These results demonstrate that PGC1a isoform switching in response to lithium is part of a broader reprogramming of transcription.

PGC1a transcript variants are CREB-responsive

One of the likely candidates in the neuronal response to lithium is the transcription factor CREB (cAMP response element binding protein). Prior studies have shown that activation of CREB promotes PGC1a transcript expression in multiple tissues, including liver where it is involved in the adaptive response to energy stress[28]. This could be important, as PGC1a is known to activate its own transcription[5]. Separate studies have shown that GSK3b regulates the stability of CREB protein and that lithium promotes CREB DNA binding[29]. Our RNA-seq data revealed a notable upregulation of cAMP-responsive transcription factors, including ATF3 and ATF4 in primary neurons treated with lithium. Analysis of canonical CREB binding motifs at each of the PGC1a promoters revealed that all three possess predicted CREB binding sites (Fig.4.3A). CREB1 mRNA was not significantly impacted by lithium treatment; however, the absence of a change at the mRNA level does not preclude CREB protein activation in the transcriptional response to lithium, or a change in occupancy at PGC1a promoters. Along these lines, treatment of primary neurons with a CREB inhibitor resulted suppression of mitochondrial membrane potential, consistent with a role for CREB in regulating neuronal energy metabolism (Fig.4.3B). Conversely, lithium treatment activated CREB protein in neurons indicated by enhancement of the nuclear

pCREB^{S133} pool (Fig.4.3C). We next tested whether modulation of PGC1a isoforms was dependent upon CREB activity in lithium treated neurons. CREB inhibition using the compound 666-15 significantly decreased PGC1a4 and PGC1a B1E2 expression, but did not impact basal levels of PGC1a1 (Fig.4.3D). Lithium dependent induction of PGC1a1 and PGC1a4 was blocked in neurons treated with CREB inhibitor, indicating that CREB is necessary for PGC1a transcript induction in response to lithium. Intriguingly, the effect of CREB inhibition and lithium were additive in suppressing PGC1a B1E2 (Fig.4.3D). In addition to direct regulation by GSK3b, CREB is activated my numerous signals including calcium signaling and neurotrophin receptors[30]. The TrkB receptor is involved in coupling neurotrophic signals to survival, differentiation, and synaptic plasticity[31]. CREB has been identified as a key effector of TrkB signaling[32]. Therefore, we speculated that modulation TrkB signaling would impact PGC1a transcript expression. Low concentrations of ANA12, a TrkB receptor antagonist, were sufficient to block PGC1a1 and PGC1a4 induction with lithium. Mirroring what was observed with CREB inhibition, the impact of TrkB inhibition and lithium were additive in suppressing PGC1a B1E2 (Fig.4.3E). These results demonstrate that the TrkB/CREB signaling axis is necessary for PGC1a1 and PGC1a4 induction with lithium. Moreover, the additive effect of lithium and TrkB/CREB pathway inhibition on PGC1a B1E2 suggest that the suppression of this transcript variant occurs through alternative mechanisms.

PGC1a transcript variants are responsive to AMPK, but not SIRT1

AMPK has been shown to directly phosphorylate PGC1a, leading to its activation in skeletal muscle[9]. Activating phosphorylation of AMPK is increased with lithium raising the possibility that AMPK could control induction of PGC1a1 and PGC1a4 transcripts via stimulation of PGC1a transcriptional co-activation. To test this, neurons were treated with lithium in the presence of an AMPK inhibitor, Compound C. AMPK inhibition had no impact on basal levels of PGC1a transcripts in neurons; however, induction of PGC1a1 and PGC1a4 by lithium was blocked in the presence of AMPK inhibitor (Fig.4.4A). In contrast, inhibition of AMPK had no effect on levels or

lithium-induced repression of PGC1a B1E2 (Fig.4.4A). SIRT1 is a metabolic regulator belonging to the sirtuin-class of NAD-dependent deacetylates that has been shown to activate PGC1a in response to elevated $NAD^+/NADH$[33]. We previously demonstrated that lithium enhanced NAD cofactor levels in H4 and the neuron-like PC12 cells (Chapter 2), suggesting that lithium could indirectly activate PGC1a function through SIRT1 activation[10]. Treatment of neurons with the sirtuin inhibitor nicotinamide had no impact on basal levels of PGC1a transcripts (Fig.4.4B). Co-treatment of nicotinamide and lithium revealed that SIRT1 is not necessary for induction of PGC1a1 and PGC1a4 transcripts in response to lithium. Furthermore, nicotinamide had no impact on lithium-induced repression of PGC1a B1E2 (Fig.4.4C). These data demonstrate that AMPK activation is necessary, but not sufficient for PGC1a1 and PGC1a4 transcript induction, and despite its established role in PGC1a activation in the periphery, SIRT1 was not involved in the regulation of PGC1a transcripts in response to lithium.

In light of the fact that expression of PGC1a B1E2 is neuron-specific and is activated through neuron differentiation, the most likely explanation for the decrease of PGC1a B1E2 expression with lithium would be transcriptional repression. An alternate possibility would be that PGC1a B1E2 is produced at normal levels in lithium treated neurons but stability of the transcript is lower. To investigate this, primary neurons were treated with an inhibitor of transcription, actinomycin D, and PGC1a mRNA expression was followed out to 24h. This experiment showed that the stability of the major neuronal isoforms of PGC1a is not equivalent. After 24h treatment with actinomycin D PGC1a1 levels were reduced by 85%, PGC1a B1E2 were reduced by 58%, and PGC1a4 reduced by 43%. These data show that neuronal PGC1a1 is significantly less stable than either PGC1a4 or PGC1a B1E2 transcripts (Fig.4.4C). To determine whether lithium might alter the rate of transcript decay, the stability test was performed in neurons pre-treated with lithium for 24h, followed by a 24h actinomycin D treatment. Lithium significantly enhanced the stability of the full-length PGC1a transcript variants, while no change was observed in PGC1a4 stability (Fig.4.4D-F). These data indicate that inherent differences in mRNA stability do not explain

reduction in PGC1a B1E2 with lithium treatment. Ongoing experiments using chromatin Immunoprecipitation of histone activating and repressing marks should reveal if the canonical, alternate, and brain specific promoters are differentially accessible in neurons versus astrocytes and if accessibility of any of the PGC1a promoters in neurons is altered in the presence of lithium.

DISCUSSION

In order to be effective, metabolic adaptation must be specific to the upstream stimulus and cell type in question. The data presented here demonstrate that neurons and astrocytes differ greatly in PGC1a transcript variant expression and in metabolic profile. Given that PGC1a is a key regulator of mitochondrial metabolism and central to multiple stimuli that induce energetic adaptation, these differences imply that neurons and astrocytes are poised to respond differently to energy stress. This observation is supported by literature that highlights differences in neuron and astrocyte metabolism. Despite showing high glycolytic rates, astrocytes release significant amounts of lactate and display lower rates of oxidative metabolism than neurons[27,34]. Neurons also lack pyruvate carboxylase, a key anaplerotic enzyme that plays a significant role in mitochondrial substrate availability[35]. Our data show that both astrocytes and neurons have relatively high mitochondrial polarization, but differ quite drastically in redox metabolism indexed by FLIM. Our multiphoton imaging data revealed longer τ_m in neurons with fluorescence decay curves that are consistent with higher rates of oxidative metabolism. In addition to these functional differences, we report different abundance of PGC1a isoforms including the neuron specific PGC1a B1E2 variant that is the dominant isoform in neurons but entirely absent from astrocytes. These data confirm that on many levels neurons have a different metabolic set point from astrocytes.

Likely as a reflection of these different metabolic set points, neurons and astrocytes responded differently to lithium treatment. We report a switch in PGC1a transcript variant expression in neurons that was not observed in astrocytes. Expression of PGC1a B1E2 is driven off a

distinct promoter, and could be part of a broader strategy that allows neurons to couple PGC1a expression to unique stimuli. In our study, we show PGC1a1 and PGC1a4 are induced by lithium while PGC1a B1E2 is repressed. Furthermore, the relative contributions of CREB/TrkB and AMPK are distinct at the different promoters. Together these findings are consistent with the idea that alternative pathways regulate the expression from each of these promoters and in turn have specific impact on each of the resulting transcript variants. We previously reported an increase in mitochondrial polarization in H4 neuroglioma cells with lithium treatment[10]. Therefore, it was surprising here that astrocytes were refractory to lithium treatment, and that the response observed in neurons was a decrease in polarization. These inconsistencies are perhaps explained by differences in intrinsic metabolism between these cells; H4 cells displayed nearly 6-fold lower mitochondrial membrane potential than their astrocyte counterparts. Quantification of oxygen consumption and metabolic fluxes in lithium-treated neurons will be useful to clarify the metabolic basis for the observed changes.

GSK3b has been linked extensively to the PI3K and mTORC1 signaling pathways[13]. Lithium treatment in neurons changed the phosphorylation status of many growth regulators, not only GSK3b, in a manner that is consistent with growth repression. Moreover, the enrichment of growth factor binding pathways and transcription factor-related pathways in the RNA-sequencing data indicates that lithium broadly impacts neuronal growth status. We observed that this cellular reprogramming converged on PGC1a transcripts through the TrkB/CREB signaling axis. Inhibition of TrkB or CREB activity was sufficient to block upregulation of PGC1a1 and PGC1a4 with lithium. CREB inhibition alone also suppressed PGC1a expression in neurons co-incident with a reduction in mitochondrial membrane potential. These outcomes might have been anticipated given the key roles that CREB plays in neuronal survival and plasticity[31]. Our data suggest that activation of CREB is inherently coupled to upregulation of PGC1a expression. This mechanism would allow neurons to link energetically consuming processes of growth and neuroplasticity to an increase in metabolic capacity by PGC1a dependent mechanisms. Despite playing a necessary role in

PGC1a1 and PGC1a4 induction with lithium, CREB inhibition was additive with the repression of PGC1a B1E2. Having eliminated the possibility that lower levels of PGC1a B1E2 in lithium treated neurons might be due to loss of transcript stability, we now favor a model of silencing at the PGC1a Brain Promoter as a candidate mechanism for lithium's effect, leading to repression of PGC1a B1E2. Lithium treatment has previously been linked to changes in chromatin modifiers. Worms exposed to lithium experienced lifespan extension accompanied by chromatin remodeling and suppression of LSD1 histone-demethylase expression[36]. Here, we observed no change in LSD1 mRNA expression; however, the exploration of chromatin modifiers is a current area of investigation related to PGC1a B1E2 and its lower abundance in lithium treated neurons.

Nutrient sensing proteins have been linked extensively to PGC1a regulation and longevity[1]. We tested the role that two of these regulators, AMPK and SIRT1, play in the neuronal response to lithium. Using an AMPK inhibitor, we demonstrate that AMPK is necessary for induction of PGC1a1 and PGC1a4 with lithium. In contrast, SIRT1 inhibition did not modify PGC1a expression or modulate the lithium response. It is still unclear whether AMPK operates in parallel to the TrkB/CREB axis or whether these are convergent mechanisms. AMPK has been shown to directly phosphorylate PGC1a protein[9]. Since PGC1a protein is active in its own transcription, one possibility is that it displays bias towards PGC1a canonical and alternative promoters in the presence of lithium. An alternative possibility stems from the observation that AMPK directly phosphorylates transcription factors in the CREB family[37]. It is possible that in the presence of lithium, activation of AMPK leads to direct phosphorylation and activation of CREB. Even if this were the case, the data from TrkB inhibited cells suggests that at least some input from the TrkB pathway upstream of CREB is required for lithium to exert its full effects on the Canonical and Alternate Promoters. GSK3b inhibition with lithium has previously been linked to enhanced CREB DNA binding[30], it should be possible to test if a lithium insensitive mutant of GSK3b (S9A) would sufficient to override lithium induced activation of CREB protein.

In summary, we have demonstrated that neurons and astrocytes differ in mitochondrial and redox metabolism, PGC1a transcript variant expression, and in response to lithium. In neurons, lithium broadly impacted gene expression, specifically impacting transcription factor regulation and growth signaling pathways. Our studies suggest that the brain-specific isoforms of PGC1a could exist to couple PGC1a to processes that are unique to neurons, such as synaptic activity or neurotransmitter metabolism. These data connect longevity-associated pathways with metabolic regulation in neurons, providing a framework for the treatment of neurodegenerative diseases where dysregulation of PGC1a has been implicated.

METHODS

Animals

Wild-type male and female C57BL/6J were obtained from Jackson Laboratories (Bar Harbor, ME) and housed under controlled pathogen-free conditions in accordance with the recommendations of the University of Wisconsin Institutional Animal Care and Use Committee. Mice were allocated to breeding pairs at 10 weeks of age with two animals per-cage.

Cell Culture

Neurons

Cultures of primary neurons were prepared from C57BL/6J mouse pups at P0-P1. Briefly, brains were dissected out into ice-cold HBSS where the midbrain and meninges were removed. Brain tissue was minced and digested in 0.25% trypsin for 20-minutes at 37C. Trypsin was quenched with DMEM/10% FBS and cells were dissociated and counted prior to plating on poly-d-lysine coated-plates. The subsequent day, medium was replaced with Neurobasal Plus media with 1% GlutaMAX and 2% B27 Plus supplement (Gibco) containing 1uM cytosine arabinoside (AraC) to eliminate glial cell populations. Subsequent media changes were carried out every 3 days with

50% media replacement without AraC. Experiments were carried out between culture day 10 and 16 (DIV10-DIV16).

Astrocytes

Primary astrocytes were dissociated similarly to neurons and plated onto uncoated T-75 culture flasks in DMEM/10% FBS. Astrocytes proliferated to confluency, and were subsequently treated with 10uM AraC for 48h to eliminate non-astrocyte glial populations. Astrocytes were passaged into T-175 flasks and maintained in DMEM/10% for subsequent experiments.

Neural Stem Cells

Hippocampi were dissected in cold HBSS and dissociated using the GentleMACS Dissociator (Miltenyi Biotec) and MACS Neural Tissue Papain Dissociation Kit (Miltenyi Biotec) according to the manufacturers protocol. NSCs were cultured in DMEM/F12 media (Invitrogen) supplemented with GlutaMAX, FGF (20ng/mL), EGF (20ng/mL) and Heparain (5ug/mL) for the indicated number of days prior to assay.

Drug Treatments

Cells were treated with 15mM LiCl 24h prior to metabolic assays, qPCR, and RNA-sequencing. For neurons, LiCl treatment accompanied a 50% media change. Drug treatments were co-administered with lithium as follows: CREB inhibitor 666-15 (Millipore) [1uM], ANA12 (Sigma) [20uM], Compound C (Millipore) [8uM], Nicotinamide (Sigma) [5mM].

Mitochondrial membrane potential

Mitochondrial membrane potential was determined using the JC-1 assay (T-3168; Thermo Fisher Scientific) in accordance with the manufacturer's instructions. Cells were incubated in 1 μg/mL

JC-1 dye for 30-minutes prior to assay. Fluorescent emission was measured at 590nm and 530nm with excitation at 535nm and 485nm respectively.

Western Blotting and Antibodies

Cells were lysed and protein was extracted in modified RIPA buffer containing protease and phosphatase inhibitors (P8340 and 524624, respectively; Sigma Aldrich, St. Louis, MO, USA). Proteins were detected by immunoblotting using standard techniques. Antibodies used were PGC1α (NBP1-04676; Novus), serine 9 phospho-GSK3b (9336; Cell Signaling Technology), threonine 172 phospho-AMPK-alpha (2535S; Cell Signaling Technology), serine 632 phospho-IRS1 (2388S; Cell Signaling Technology), threonine 308 phospho-AKT (13038S; Cell Signaling Technology), serine 240 phospho S6 (2215S; Cell Signaling Technology), serine 133 phospho-CREB (ab32096; Abcam).

Multiphoton laser scanning Microscopy

Immediately prior to multiphoton imaging, cells were fixed for 10 minutes with formalin and mounted onto glass coverslips using Cytoseal 60 mounting solution. The instrument response function of the optical system was calibrated before each imaging session. A Nikon 100x lens (Melville, NY, USA) was used for all imaging. Data were collected using an excitation wavelength of 740 nm, and emission was filtered at 457 ± 50 nm, the spectral peak for NADH/NADPH. The data collection time was 120 s using a pixel frame size of 256 × 256. The system has multiple detectors including a 16 channel combined spectral lifetime detector (utilizes a Hamamatsu PML-16 PMT), detection range 350 to 720 nm, and a H7422P GaAsP photon counting PMT (Hamamatsu) for intensity and lifetime imaging. Acquisition was performed with WiscScan, a LOCI developed acquisition package software. Fluorescence lifetime data were analyzed in SPCImage (Becker & Hickl, v.3.9.7, Berlin, Germany) where a Levenberg–Marquardt routine for nonlinear fitting was used to fit the fluorescence decay curve collected for each pixel in the 256 × 256 frame

to a model multi-exponential decay function. Data were assessed by the minimized chi-square value generated during the fit so that analysis was unbiased. To eliminate background fluorescence a threshold for analysis was applied based on photon counts. Additionally, pixels were assigned a bin of 2 for optimal fitting of the data.

Transcriptomics

DIV10 neurons were treated with LiCl for 24h and lysed with TRIzol. RNA extraction proceeded using a Direct-zol RNA kit (Zymo Research, Irvine, CA) according to the manufacturer's instructions. Purified total RNA was then used to generate mRNA-sequencing libraries using NEBNext Poly(A) mRNA Magnetic Isolation Module and NEBNext Ultra RNA Library Prep kit for Illumina (Illumina Inc., San Diego, California, USA). Libraries were then submitted to the University of Wisconsin-Madison Biotechnology Center Sequencing Facility for high throughput RNA-Seq.

Quality and quantity was assessed using an Agilent DNA1000 series chip assay and Invitrogen Qubit HS Kit (Invitrogen), respectively. Sequencing reads were trimmed to remove sequencing adaptors and low-quality bases, aligned to mm10 reference genome using the STAR aligner, and alignments used as input to RSEM for quantification. Differential gene expression analysis was performed via EdgeR generalized linear model (GLM) method.

Statistics

All Student's t-tests were two tailed. One-way ANOVA was conducted assuming Gaussian distribution and corrected for multiple comparisons using Tukey's test.

REFERENCES

1 Anderson, R. M. *et al.* Dynamic regulation of PGC1alpha localization and turnover implicates mitochondrial adaptation in calorie restriction and the stress response. *Aging Cell* **7**, 101-111, doi:10.1111/j.1474-9726.2007.00357.x (2008).

2 Miller, K. N., Clark, J. P. & Anderson, R. M. Mitochondrial regulator PGC1a-Modulating the modulator. *Curr Opin Endocr Metab Res* **5**, 37-44, doi:10.1016/j.coemr.2019.02.002 (2019).

3 Barger, J. L. *et al.* A Conserved Transcriptional Signature of Delayed Aging and Reduced Disease Vulnerability Is Partially Mediated by SIRT3. *PLoS One* **10**, e0120738, doi:10.1371/journal.pone.0120738 (2015).

4 Miller, K. N. *et al.* PGC1a integrates a metabolism and growth network linked to caloric restriction. *Aging Cell*, e12999, doi:10.1111/acel.12999 (2019).

5 Martinez-Redondo, V., Pettersson, A. T. & Ruas, J. L. The hitchhiker's guide to PGC1alpha isoform structure and biological functions. *Diabetologia* **58**, 1969-1977, doi:10.1007/s00125-015-3671-z (2015).

6 Puigserver, P. *et al.* A cold-inducible coactivator of nuclear receptors linked to adaptive thermogenesis. *Cell* **92**, 829-839 (1998).

7 Fernandez-Marcos, P. J. & Auwerx, J. Regulation of PGC1alpha, a nodal regulator of mitochondrial biogenesis. *Am J Clin Nutr* **93**, 884s-890, doi:10.3945/ajcn.110.001917 (2011).

8 LeBleu, V. S. *et al.* PGC1α mediates mitochondrial biogenesis and oxidative phosphorylation in cancer cells to promote metastasis. *Nat Cell Biol* **16**, 992-1003, 1001-1015, doi:10.1038/ncb3039 (2014).

9 Jager, S., Handschin, C., St-Pierre, J. & Spiegelman, B. M. AMP-activated protein kinase (AMPK) action in skeletal muscle via direct phosphorylation of PGC1alpha. *Proc Natl Acad Sci U S A* **104**, 12017-12022, doi:0705070104 [pii] 10.1073/pnas.0705070104 (2007).

10 Martin, S. A. *et al.* GSK3beta Regulates Brain Energy Metabolism. *Cell Rep* **23**, 1922-1931.e1924, doi:10.1016/j.celrep.2018.04.045 (2018).

11 Olson, B. L. *et al.* SCF Cdc4 acts antagonistically to the PGC1 ␣ transcriptional coactivator by targeting it for ubiquitin-mediated proteolysis. 252-264, doi:10.1101/gad.1624208.cose (2008).

12 Souder, D. C. & Anderson, R. M. An expanding GSK3 network: implications for aging research. *Geroscience*, doi:10.1007/s11357-019-00085-z (2019).

13 Martinez-Redondo, V. *et al.* Peroxisome Proliferator-activated Receptor gamma Coactivator-1 alpha Isoforms Selectively Regulate Multiple Splicing Events on Target Genes. *J Biol Chem* **291**, 15169-15184, doi:10.1074/jbc.M115.705822 (2016).

14 Soyal, S. M. *et al.* The PPARGC1A locus and CNS-specific PGC1alpha isoforms are associated with Parkinson's Disease. *Neurobiol Dis* **121**, 34-46, doi:10.1016/j.nbd.2018.09.016 (2019).

15 Chang, J. S. *et al.* NT-PGC1alpha protein is sufficient to link beta3-adrenergic receptor activation to transcriptional and physiological components of adaptive thermogenesis. *J Biol Chem* **287**, 9100-9111, doi:10.1074/jbc.M111.320200 (2012).

16 Ruas, J. L. *et al.* A PGC1alpha isoform induced by resistance training regulates skeletal muscle hypertrophy. *Cell* **151**, 1319-1331, doi:10.1016/j.cell.2012.10.050 (2012).

17 Chang, J. S., Jun, H. & Park, M. Transcriptional coactivator NT-PGC-1α promotes gluconeogenic gene expression and enhances hepatic gluconeogenesis. *Physiol Rep* **4**, doi:10.14814/phy2.13013 (2016).

18 Soyal, S. M. *et al.* A greatly extended PPARGC1A genomic locus encodes several new brain-specific isoforms and influences Huntington disease age of onset. *Hum Mol Genet* **21**, 3461-3473, doi:10.1093/hmg/dds177 (2012).

19 Soyal, S. M. *et al.* The Expression of CNS-Specific PPARGC1A Transcripts Is Regulated by Hypoxia and a Variable GT Repeat Polymorphism. *Mol Neurobiol* **57**, 752-764, doi:10.1007/s12035-019-01731-5 (2020).

20 Lin, J. *et al.* Defects in adaptive energy metabolism with CNS-linked hyperactivity in PGC1alpha null mice. *Cell* **119**, 121-135 (2004).

21 Lucas, E. K. *et al.* Developmental Alterations in Motor Coordination and Medium Spiny Neuron Markers in Mice Lacking PGC1α. *PLoS One* **7**, doi:10.1371/journal.pone.0042878 (2012).

22 Jiang, H. *et al.* Adult Conditional Knockout of PGC1α Leads to Loss of Dopamine Neurons. *eNeuro* **3**, doi:10.1523/eneuro.0183-16.2016 (2016).

23 J, C., S, R., K, Z., RA, B. & DK, S. Association of PGC1alpha Polymorphisms With Age of Onset and Risk of Parkinson's Disease. *BMC medical genetics* **12**, doi:10.1186/1471-2350-12-69 (2011).

24 Cui, L. *et al.* Transcriptional repression of PGC1alpha by mutant huntingtin leads to mitochondrial dysfunction and neurodegeneration. *Cell* **127**, 59-69, doi:S0092-8674(06)01205-0 [pii] 10.1016/j.cell.2006.09.015 (2006).

25 Parihar, M. S. & Brewer, G. J. Mitoenergetic failure in Alzheimer disease. *Am J Physiol Cell Physiol* **292**, C8-23, doi:10.1152/ajpcell.00232.2006 (2007).

26 Qin, W. *et al.* PGC1alpha expression decreases in the Alzheimer disease brain as a function of dementia. *Arch Neurol* **66**, 352-361, doi:10.1001/archneurol.2008.588 (2009).

27 Belanger, M., Allaman, I. & Magistretti, P. J. Brain energy metabolism: focus on astrocyte-neuron metabolic cooperation. *Cell Metab* **14**, 724-738, doi:10.1016/j.cmet.2011.08.016 (2011).

28 Herzig, S. *et al.* CREB regulates hepatic gluconeogenesis through the coactivator PGC1. *Nature* **413**, 179-183 (2001).

29 Grimes, C. A. & Jope, R. S. CREB DNA binding activity is inhibited by glycogen synthase kinase-3 beta and facilitated by lithium. *J Neurochem* **78**, 1219-1232 (2001).

30 Paramanik, V. & Thakur, M. K. Role of CREB signaling in aging brain. *Arch Ital Biol* **151**, 33-42, doi:10.4449/aib.v151i1.1461 (2013).

31 Gupta, V. K., You, Y., Gupta, V. B., Klistorner, A. & Graham, S. L. in *Int J Mol Sci* Vol. 14 10122-10142 (2013).

32 Minichiello, L. *et al.* Mechanism of TrkB-mediated hippocampal long-term potentiation. *Neuron* **36**, 121-137, doi:10.1016/s0896-6273(02)00942-x (2002).

33 Canto, C. & Auwerx, J. PGC1alpha, SIRT1 and AMPK, an energy sensing network that controls energy expenditure. *Curr Opin Lipidol* **20**, 98-105, doi:10.1097/MOL.0b013e328328d0a4 00041433-200904000-00004 [pii] (2009).

34 Itoh, Y. *et al.* Dichloroacetate effects on glucose and lactate oxidation by neurons and astroglia in vitro and on glucose utilization by brain in vivo. *Proc Natl Acad Sci U S A* **100**, 4879-4884, doi:10.1073/pnas.0831078100 (2003).

35 Shank, R. P., Bennett, G. S., Freytag, S. O. & Campbell, G. L. Pyruvate carboxylase: an astrocyte-specific enzyme implicated in the replenishment of amino acid neurotransmitter pools. *Brain Res* **329**, 364-367, doi:10.1016/0006-8993(85)90552-9 (1985).

36 McColl, G. *et al.* Pharmacogenetic analysis of lithium-induced delayed aging in Caenorhabditis elegans. *J Biol Chem* **283**, 350-357, doi:10.1074/jbc.M705028200 (2008).

37 Thomson, D. M. *et al.* AMP-activated protein kinase phosphorylates transcription factors of the CREB family. *J Appl Physiol (1985)* **104**, 429-438, doi:10.1152/japplphysiol.00900.2007 (2008).

Figure 4.1

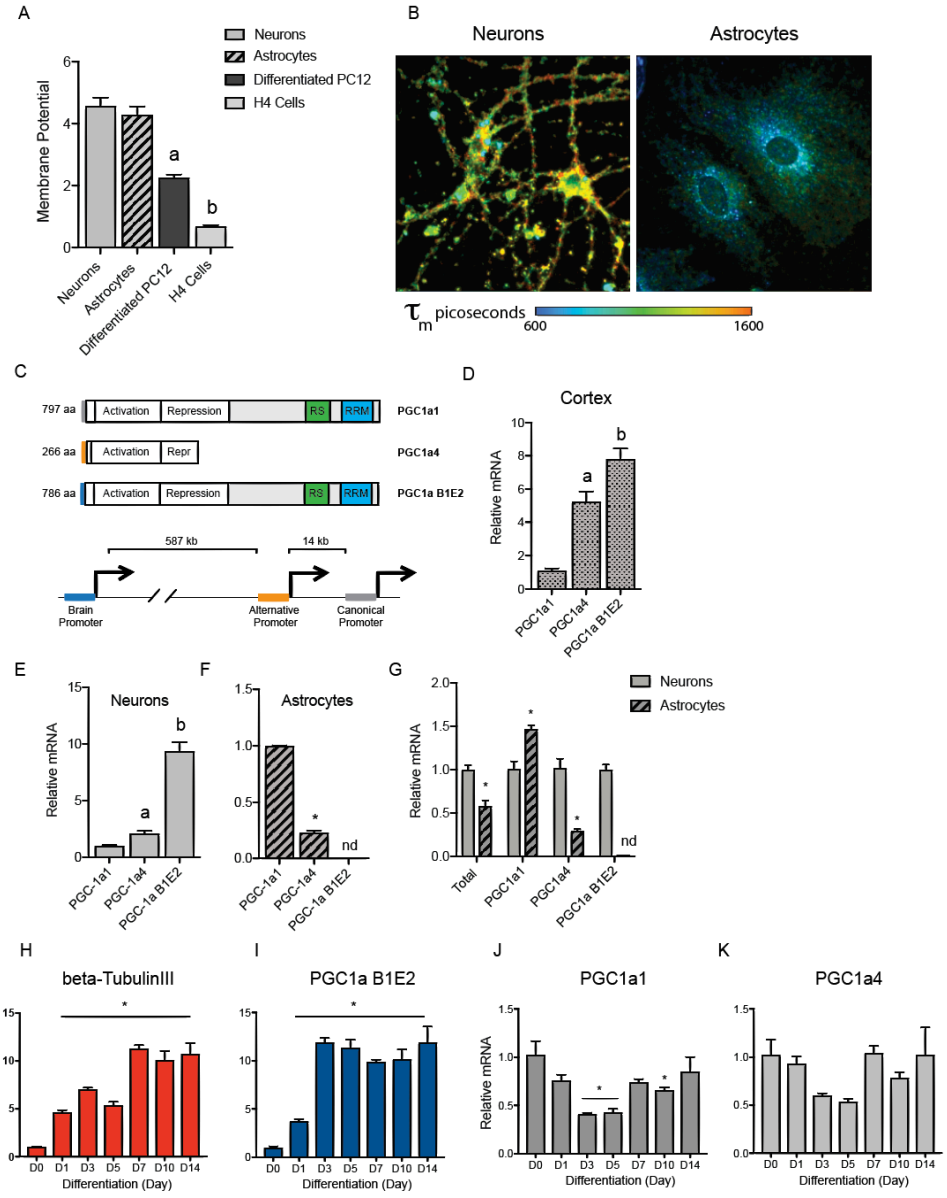

Figure 4.1. Neurons and astrocytes differ in metabolic phenotype and PGC1a expression. (A) JC-1 assay of mitochondrial membrane potential in primary neurons, astrocytes, differentiated PC12, and H4 neuroglioma. (B) Representative images showing NAD(P)H mean fluorescence lifetime (τ_m) between primary neurons and astrocytes (ex740nm). (C) Schematic of predicted functional domains within PGC1a isoforms. (D-F) Relative expression of PGC1a transcript variants in (D) mouse cortical homogenate (E) primary cultured neurons (DIV10) and (F) astrocytes. (G) Relative expression of individual PGC1a transcript variants between primary neurons and astrocytes. (H-K) Hippocampal neural stem cells (NSCs) differentiated over 14 days with quantification of (H) beta tubulin III (I) PGC1a B1E2 (J) PGC1a1 and (K) PGC1a4 transcripts.

n = 3-6 biological replicates per assay; data are shown as an average ± SEM; *p < 0.05 Student's t test, ANOVA.

Figure 4.2

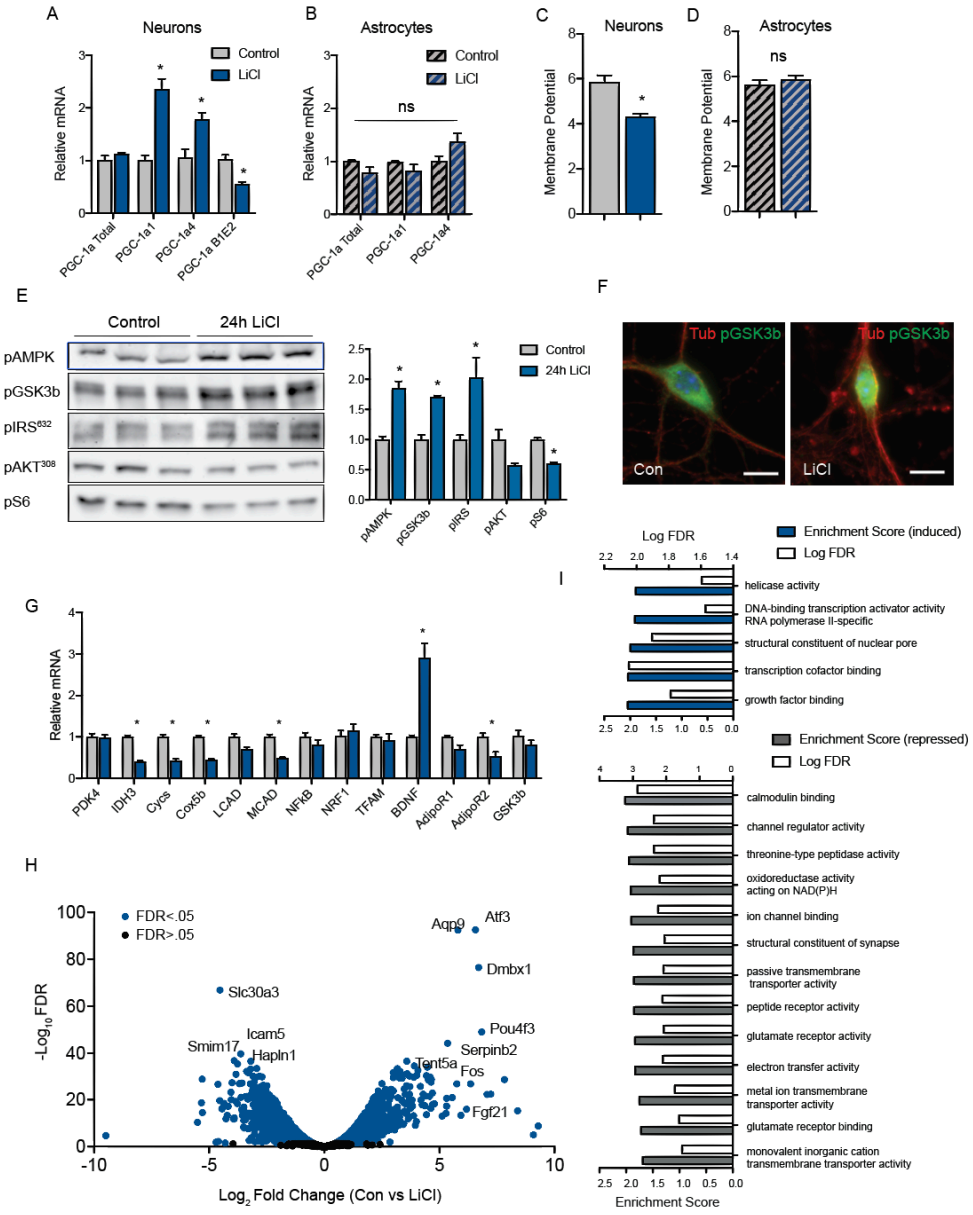

Figure 4.2. Neurons but not astrocytes are metabolically responsive to lithium treatment. (A-B) Quantification of PGC1a transcript variants in (A) neurons and (B) astrocytes following 24h LiCl [15mM] treatment. (C-D) JC-1 assay of mitochondrial membrane potential in (C) neurons and (D) astrocytes. (E) Western blot and quantitation of pAMPK[T172], pGSK3b[S9], pIRS[S632], pAKT[T308], and pS6[S240] in neurons. (F) Immunofluorescent stain of tubulin and pGSK3b[S9] in control and LiCl-treated neurons (100x). Scale bar = 10µm. (G) Quantification of PGC1a-target transcripts. (H) Volcano plot showing differentially expressed transcripts in LiCl-treated neurons. (I) Gene-set enrichment analysis (GSEA) of differentially expressed transcripts using gene ontology (GO) terms for molecular function.

n = 3-6 biological replicates per assay; data are shown as an average ± SEM; *p < 0.05 Student's t test.

Figure 4.3

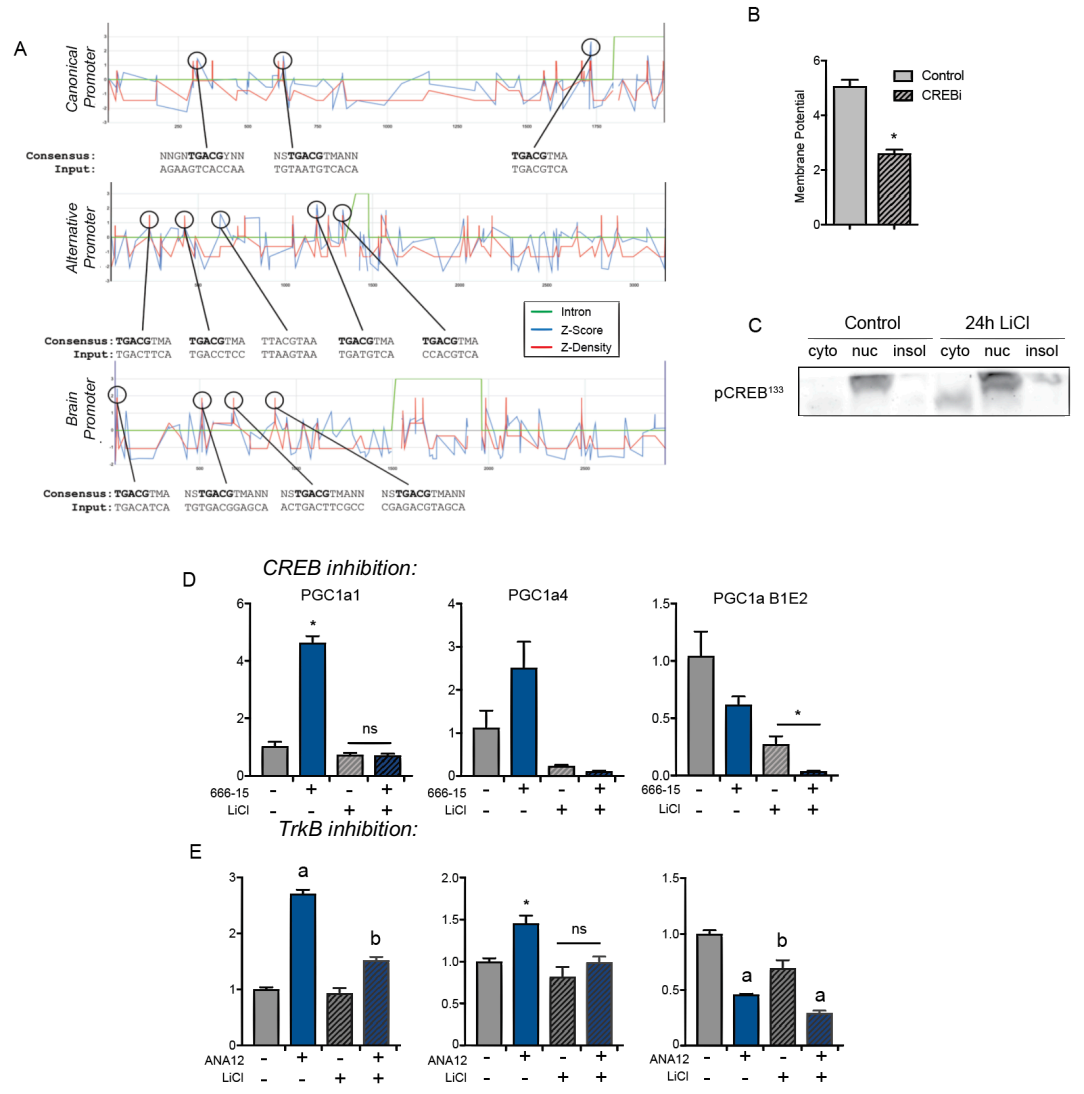

Figure 4.3. PGC1a transcript variants are CREB-responsive. (A) Schematic of predicted CREB-binding sites on PGC1a promoters. (B) JC-1 assay of mitochondrial membrane potential in neurons following 24h treatment with CREB inhibitor 666-15 [1uM]. (C) Western blot of pCREB[S133] in nuclear/cytosolic fractions of neurons following 24h treatment with LiCl. (D-E) Quantification of PGC1a transcript variants following 24h LiCl treatment in the presence or absence of (D) CREB inhibitor 666-15 or (E) ANA12 [20uM].

n = 3 biological replicates per assay (n=1 cytosolic/nuclear fractionation); data are shown as an average ± SEM; *p < 0.05 Student's t test.

Figure 4.4

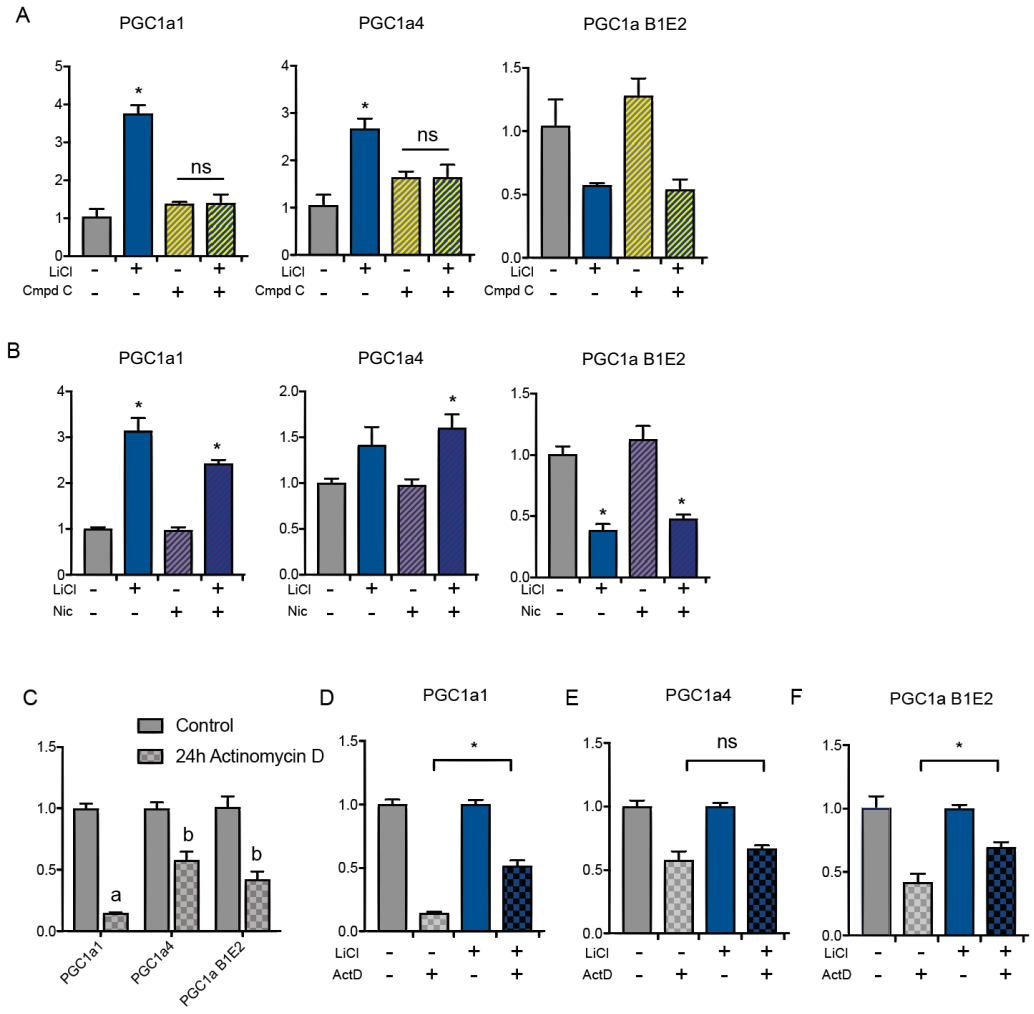

Figure 4.4. PGC1a transcript variants are responsive to AMPK, but not SIRT1. (A-B) Quantification of PGC1a transcript variants in neurons following 24h LiCl treatment in the presence or absence of (A) compound C or (B) nicotinamide. (C) Expression of PGC1a transcript variants at baseline and after 24h treatment with actinomycin D. (D-F) Pre-treatment of neurons with 24h LiCl followed by 24h actinomycin D and quantification of (A) PGC1a1 (B) PGC1a4 and (C) PGC1a B1E2 transcripts.

n = 3-6 biological replicates per assay; data are shown as an average ± SEM; *p < 0.05 Student's t test.

Table 4.1

PGC1a Primer Sequences		
Transcript Variant	Forward	Reverse
PGC1a (Total)	TGATGTGAATGACTTGGATACAGACA	GCTCATTGTTGTACTGGTTGGATATG
PGC1a1	GGACATGTGCAGCCAAGACTCT	CACTTCAATCCACCCAGAAAGCT
PGC1a4	TCACACCAAACCCACAGAAA	CTGGAAGATATGGCACAT
PGC1a B1E2	TACAACTACGGCTCCTCCTGG	TTCAGGAAGATCTGGGCAAAGA

Chapter 5: Metabolism, inflammation, and age in Alzheimer's disease pathology

The following chapter has been prepared for submission as a manuscript:

Metabolism, inflammation, and age in Alzheimer's disease pathology
Dylan C Souder, Isabelle A Dreischmeier, Alexandra Schroeder, Abdul Kader Sagar, Stephen A Martin, Rozalyn M Anderson

Isabelle Dreischmeier assisted in histological sectioning. Alexandra Schroeder and Abdul Kader Sagar advised in multiphoton data acquisition and interpretation. Stephen A Martin collected and processed APP/PSEN1 mouse brains. Dylan C Souder performed the remaining histology, imaging, and analysis.

ABSTRACT

Amyloid plaque formation is a defining feature in Alzheimer's disease (AD). Accumulating evidence implicates mitochondrial dysfunction in AD progression, but the impact of amyloid deposition on metabolism in the plaque microenvironment is not well defined. Our current understanding of plaque formation, clearance, and impact on the surrounding tissue is largely based on mouse models of amyloidosis; however, late-onset AD includes age as a major risk factor, and functional outcomes of AD pathology observed in humans are not recapitulated in mouse models. The purpose of this study is to determine if metabolism in the amyloid plaque microenvironment could explain differences in the impact of AD pathology. Here we use brain tissue from transgenic APP/PSEN1 mice, rhesus monkeys with age-related development of amyloid plaques, and human AD subjects with moderate to severe amyloid plaque load. Quantitative microscopy reveals altered energetics in the plaque microenvironment as a shared feature across species, including changes in mitochondrial distribution and enzymatic activity. Multiphoton imaging confirms a localized disturbance of metabolism in the immediate vicinity of plaques, with changes in intensity and chemical properties of redox cofactors NAD(P)H. Lipofuscin, cellular debris, was identified around amyloid plaques in all three species; however, a greater burden was detected in the brains from monkeys and humans of advanced age. Astrocyte activation was detected as increased abundance of glial fibrillary acidic protein (GFAP), indicative of localized astrogliosis. Amyloid plaque-induced inflammation was confirmed via Iba1 detection that revealed recruitment of activated microglia to the immediate area. These inflammatory signatures were shared among mice, monkeys, and humans; however, the area of the inflamed zone was considerably larger for monkeys and humans compared to mice, and the extent to which microglia were activated was greater in monkeys. Although it is possible that the greater response in the plaque microenvironment is due to species-specific differences, it seems likely that age is also a factor since both monkeys and humans spontaneously develop amyloid plaques later in life. Our studies suggest that animal models of AD that do not include an age-component may fail to recapitulate the amyloid plaque

microenvironment, hampering our understanding of how the pathology might contribute to functional loss.

INTRODUCTION

Alzheimer's disease (AD) is a progressive neurodegenerative condition that accounts for most cases of dementia in the United States[1]. AD manifests as either early-onset familial AD that has clear genetic underpinnings, or late-onset AD (LOAD) that is more prevalent, accounting for approximately 95% of occurrences[2]. Familial AD is the result of inherited mutations in the amyloid precursor protein (APP) and presenilins (PSEN1 and PSEN2)[3-5]; however, the cause of LOAD remains elusive. Genetic risk factors including APOE4 and TREM2 have been found to massively increase the risk of disease, but it is unclear how they are involved in AD pathogenesis and progression[6]. Environmental and lifestyle factor have also been linked to disease risk. Obesity, diabetes, and a sedentary lifestyle have all been shown to increase the risk and severity of AD, as well as the age of onset[7,8]. The diverse set of genetic and environmental risk factors in LOAD presents a challenge for researchers who attempt to model the condition. The majority of animal models for AD are transgenic mice expressing mutant versions of APP, presenilins, and human tau proteins; in general the goal is to drive accelerated plaque and tangle formation[9], however aged mice are seldom studied. Consequently, these models are better in recapitulating familial AD and fall short in producing many of the molecular phenotypes of LOAD. Importantly, therapeutics developed using these mouse models have consistently failed in clinical trials[10]. We propose that the translational failure of AD mouse models stems from two primary reasons; (1) Mice do not naturally develop plaques and tangles, and exhibit many intrinsic differences from humans in glial biology. (2) Age is the greatest determinant of AD, and most transgenic mouse models are early-onset. Moreover, many aspects of brain aging are unique within species so these factors likely conspire to produce AD vulnerability in humans. This introduction will elaborate on aspects of primate glial biology and brain aging that are most relevant to AD. The following study will describe these differences using the APP/PSEN1 mouse, aged rhesus macaques, and cortical tissue from human AD cases.

Astrocytes are critical in maintaining many aspects of neuronal homeostasis, including neurotransmitter recycling, nutrient delivery, and structural support[11]. These functional roles become impaired in AD, particularly surrounding neuritic plaques where astrocytes adopt a reactive phenotype. This population of astrocytes become hypertrophic and inflammatory through cross talk with microglia and neuronal populations[12]. Co-culture studies have established that astrocytes are vulnerable to metabolic dysfunction and mediate neurotoxicity in response to amyloid exposure[13,14]. However, astrocytes have also been shown to facilitate amyloid uptake and removal in animal models[15], suggesting that astrocyte integrity is important for AD resilience. Importantly, most of this evidence is founded in rodent models of amyloidosis or in primary cultures of astrocytes derived from these animals. Human astrocytes in contrast are far more complex and heterogenous in structure and function. Typical protoplasmic astrocytes in the human brain are larger, display 10-fold more processes, and are more numerous relative to neurons[16]. More rapid, and diverse patterns of calcium transients have also been recorded in human astrocytes, perhaps owing to their larger size and complexity[17]. Intriguingly, human astrocyte progenitor cells grafted into mouse brains retained properties of human astrocytes and enhanced synaptic plasticity and memory[18]. This study shows that human astrocytes contribute to higher order brain functions that could potentially have cognitive implications with aging and disease. Despite these differences, many similarities have also been noted between human and rodent astrocytes, specifically in regards to neurotransmitter recycling and metabolism[16]. Astrocyte activation is common to AD postmortem brains and AD mouse models; however, the equivalency of astrocyte activation between species is unclear.

Microglia are brain-resident macrophages that play diverse roles in clearing debris, pruning synapses, and mediating immune responses[19]. Beta amyloid triggers microglial activation similarly to astrocytes whereby microglia become hypertrophic and phagocytic[20]. In particular, the microglial receptor TREM2 is involved in amyloid clearance and has been shown to increase the risk of AD four-fold[21]. The TREM2 signaling pathway has recently been shown to interact with

APOE around neuritic plaques to produce a neurodegenerative phenotype[22]. Microglial activation is common to both animal models of AD and post-mortem AD brains[20]; however, TREM2 and APOE4 gene variants are uniquely human risk factors suggesting that microglial activity in AD mouse models does not fully recapitulate the disease state. Single-cell RNA sequencing has illuminated a wide array of microglial subtypes active across developmental stages, brain regions, and disease states[23,24]. Accumulating evidence suggests that these subtypes are dynamic and play key roles in shaping disease vulnerability and progression[24]. Despite this progress, it is unknown the extent to which the phenotypic variance in animal models overlaps with human biology. Very recent evidence suggests that there is at least some overlap between disease-associated microglial subtypes in mice and humans[25]; however, mouse derived samples fail to capture heterogeneity of human samples, and species-specific mechanisms of microglial activity are largely unknown.

Aging is the most significant risk factor for non-communicable disease, particularly AD, where the prevalence nearly doubles every five years after age sixety-five[26]. Even during normative aging the human brain atrophies and older individuals experience a gradual decline in cognitive function and sensory perception[27]. As discussed previously, brain energy metabolism declines with aging and we speculate that this is intrinsically linked to functional loss[28]. The functional connectivity of neuronal networks declines with age; reflecting impaired calcium homeostasis, neurotrophic signaling, and mitochondrial function[29,30]. Glial function is similarly perturbed during aging. Astrocyte size is reportedly increased in a region-dependent manner in the mouse brain, accompanied by elevated GFAP expression[31]. The mRNA levels of glial fibrillary acidic protein (GFAP) are similarly upregulated in aged rodent and human brain[32]; however, it is unclear whether these changes are uniform between glial subtypes and regions. Microglia adopt increasingly amoeboid morphologies during aging and release more pro-inflammatory cytokines[30]. Termed “microglial priming” this process has been speculated to modify the inflammatory response to amyloid plaques in a dysfunctional way[33]. Complement protein levels increase with age in the

mouse brain and blocking the complement pathway was shown to delay age-related cognitive decline[34]. Perhaps the most salient difference between rodent and human aging is the formation of amyloid plaques; in contrast to humans, APP-processing in rodents does not result in amyloid oligomerization or plaque formation[35]. Amyloidosis is a feature of normative aging in humans. Many of these individuals go on to develop full-blown AD, while others are resilient and never experience dementia[36]. Most AD mouse models involve early-onset pathologies with rapid appearance of plaques and tangles. In excluding the ways in which aging is intertwined with the emergence of AD pathology it is possible that these transgenic mouse models are missing an essential contribution in the aging brain environment as the backdrop for onset and progression of the most prevalent form of AD.

Non-human primate species closely recapitulate the progression, cognitive decline, and neuropathology observed in human brain aging[37]. The Wisconsin National Primate Research Center initiated adult-onset longitudinal studies to assess biology of aging and the impact of CR on health and longevity[38-40]. Rhesus macaques remarkably phenocopy human aging and respond to CR similarly to rodents, with longer lifespans and reduced incidence of age related disease[41]. Rhesus macaques display age-related accumulation of amyloid plaques similarly to humans, including vascular amyloid accumulation. Many of these plaques are immunoreactive for ApoE and physically resemble plaques found in AD patients[42]. Moreover, a recent study has demonstrated that macaques develop Braak state III/IV tau pathology[43], suggesting that they may be a suitable model for LOAD. Brain aging in rhesus macaques is remarkably similar to humans; microinjection of fibrillary amyloid beta into the aged macaque cortex results in neuronal loss, tau phosphorylation, and microglial proliferation. Similar neurotoxicity was not observed in young macaques, or in aged marmosets and aged rats[44]. Hippocampal amyloid content in the Wisconsin cohort of macaques was similar between control and CR animals; however, CR attenuated astrocyte activation[45]. In the following study we compare the microenvironment of neuritic plaques between the

APP/PSEN1 mouse model of AD, aged macaques, and humans with diagnosed AD. We investigate if the metabolic environment is altered by plaque formation across mouse, monkey and human brain specimens, and assess the inflammatory impact in terms of astroglial and microglial activation surrounding amyloid plaques.

RESULTS

Mitochondria accumulate around amyloid plaques

Mitochondrial dysfunction is increasingly being recognized as a key feature of AD pathology[46], and the impact of changes in mitochondrial activity on neuronal function is an active area of research. This multi-species study used brain tissues taken from male APP/PSEN1 mice (6-month; n=6), male and female rhesus monkeys (~31 years; n=5), and male and female human subjects (~86 years; n=10) (Table 5.1). Human tissue was acquired from the Wisconsin Registry of Alzheimer's Patients [47], and the study used specimens taken from the temporal cortex in subjects with confirmed, post-mortem diagnosis of AD. Monkey brain tissue was obtained from advanced-aged monkeys from the UW-Madison longitudinal study on aging and calorie restriction (CR), and the temporal cortex was sectioned to match the human analysis. Brain tissue was taken from APP/PSEN1 mice, and sections were generated using the somatosensory cortex. We used quantitative histological and immunodetection techniques on slices of cortical tissues from mice, monkeys, and humans to identify plaques and to investigate the localized impact on metabolic and inflammatory parameters.

Amyloid plaques were identified by thioflavin S (ThS) stain that binds to amyloid plaques and can be detected by blue/green fluorescence. Greater diversity in amyloid plaque morphology and size was observed in monkeys and humans relative to transgenic mice (Fig.5.1A-B). In cortical sections from APP/PSEN1 mice, 39 individual plaques from 5 mice were quantified. Mean plaque size in mouse cortex was 1129 μm^2 (Fig.5.1B). Mitochondria were detected using antibod-

ies against voltage dependent anion channel 1 (VDAC1), an abundant mitochondrial outer membrane transporter protein that reflects mitochondrial density. Here, enhanced mitochondrial density (red) was detected within the immediate plaque zone (Fig.5.1C). Simultaneous detection of amyloid plaques (green) confirmed mitochondrial accumulation in a zone completely surrounding the plaque. Using the same approach in cortical sections from rhesus monkeys, 69 individual plaques from 5 monkeys were quantified. Here, amyloid plaque size was more variable than in mice, and mean plaque size was significantly greater at 1957 μm^2. The same enhancement of mitochondrial density surrounding plaques was identified (Fig.5.1D). In humans, 294 individual plaques from 10 samples were quantified. Mean plaque size (2111 μm^2) was similar to what was observed in monkeys and significantly greater than mice. High autofluorescence in the brains from human subjects confounded fluorescent labeling of mitochondria (Fig.5.1E); however, immunohistochemical staining of VDAC1 revealed a similar increase in mitochondrial density surrounding plaques that closely paralleled the mitochondrial enrichment detected in mice and monkeys (Fig.5.1F).

The VDAC stain only detects the presence of mitochondrial and does not inform about activity. Formalin-based fixation of monkey and human cortical tissue prohibited enzyme activity-based quantitation; however, the mouse tissues were flash-frozen so it was possible to determine whether the plaque-associated population of mitochondria were functional. Histochemical detection of enzymatic activity of complex IV of the electron transport chain, cytochrome c oxidase, revealed that this population of mitochondria retains activity (Fig.5.1G-H). Complex IV activity was detected as a punctate staining pattern directly surrounding the plaque zone, mirroring the staining pattern for VDAC. The close proximity and staining pattern suggest that dystrophic neurites rather than glial populations are likely the source of mitochondrial enrichment. These data show that a distinct population of mitochondria accumulate near amyloid plaques, and that this phenomenon is conserved from mice, to monkeys, to humans.

Multiphoton imaging confirms plaque-associated localized metabolic disruption

Taking a broader view, we used multiphoton imaging to investigate the impact of amyloid plaques on factors involved in intermediary metabolism. Nicotinamide adenine dinucleotide (NAD) and nicotinamide adenine dinucleotide phosphate (NADP) are central co-factors in redox metabolism that autofluoresce in their reduced form NAD(P)H. As previously described, multiphoton imaging can be used to quantify the fluorescence intensity and fluorescence lifetime of NAD(P)H in cells or in tissue sections, and in vivo. Using near infra-red excitation, MPLSM non-invasively detects NAD(P)H autofluorescence and fluorescence lifetime imaging microscopy (FLIM) measures the latency between excitation and photon release. These measures are used to quantify NAD(P)H levels and the cellular environment of NAD(P)H respectively. Mean fluorescence lifetime (τ_m) describes a first order decay curve including a fast component (τ_1) and a slow component (τ_2) that correspond to free and protein-bound pools of NAD(P)H. Here, we imaged histological cortical sections from mice, monkeys, and human subjects to determine NAD(P)H cofactor status in regions impacted by amyloid plaques (Fig.5.2A-B). Amyloid plaques were identified by their autofluorescence in all three species, in each case with a level of intensity that was greater than the surrounding tissue (Fig.5.2C). To investigate whether the plaques themselves might be responsible for the autofluorescence signal, three adjacent APP/PSEN1 brain sections were respectively stained using antibodies against glial fibrillary acidic protein (GFAP - a marker of astrocytes that increases expression upon astrocyte activation), antibodies against beta amyloid, or unstained for MPLSM and FLIM (Fig.5.2D-G). The plaque-associated autofluorescence occupied a similar area to that detected with beta-amyloid specific antibodies, narrowing down possible sources of the signal. Second harmonic generation imaging is a multiphoton method for detecting complex protein structures, including fibrosis[48]. SHG imaging did not detect the plaques as features, ruling out the possibility that fibrotic content gave rise to the signal (data not shown). An additional possibility is a contribution from the clustering of mitochondria in the area adjacent to

the plaques, which as a major pool of cellular NAD(P)H, could reasonably give rise to the detected signal.

Brain tissues taken at older-age carry a greater burden of lipofuscin deposits

One of the advantages of the multiphoton imaging is the ability to detect lipofuscin particles. Lipofuscin is an autofluorescent deposit of oxidized lipids, proteins, and metal ions that increases with aging[49]. Impaired macroautophagy and mitochondrial turnover is thought to be a main driver in lipofuscin accumulation, resulting in cellular impairment[50,51]. Lipofuscin deposits are detected as high autofluorescence intensity foci by MPLSM and were detected throughout the cortex in mice, monkeys, and humans (Fig.5.3A). FLIM allows for separation of signals from lipofuscin deposits, as they exhibit a characteristic signature of very short fluorescence lifetime (τ_m) (Fig.5.3B). FLIM confirms the identity of the high intensity foci as lipofuscin particles, and allowed for quantitation of particle size. Lipofuscin particle size was significantly greater in brains from monkeys than brains from mice and greater still in brains from human subjects (Fig.5.3C). The total numbers of lipofuscin particles were similar among species (Fig.5.3D), but the accumulation of large particle sizes was unique to monkeys and humans suggesting that this is likely an age dependent trait. The data presented here suggest that levels of lipofuscin are elevated in human AD, and that aged monkeys more closely recapitulate this phenotype than mice.

Astrogliosis in response to beta-amyloid shows an age-component

Astrocyte reactivity is among the most definitive features of neuritic plaques and has been documented in several animal models of AD[31]. Consequently, astrocyte reactivity is a common outcome measure in studies that focus on sources of neurotoxicity due to plaques. Here we sought to compare astrocyte activation in the APP/PSEN1 mouse, aged monkeys with amyloid burden, and brain tissue from human subjects with AD. The presence of astrocytes in cortical tissue and the extent of their reactivity was quantified by immunofluorescent detection of GFAP.

Amyloid plaques were identified in parallel using thioflavin S (ThS). In monkeys and humans, cortical astrocytes were larger with more numerous processes compared to mice, consistent with prior reports[16] (Fig.5.4A). In cortical sections from APP/PSEN1 mice, activated astrocytes were clustered in the immediate area surrounding amyloid plaques (Fig5.4B). Similar to the mouse model, GFAP abundance was elevated in the amyloid plaque vicinity in monkeys (Fig.5.4C); however, the extent of astrocyte activation was significantly greater in monkeys than in mice, where GFAP fluorescence resolved to baseline at 36 μm from the edge of the plaque in mice, but resolved out to 60 μm in monkeys (Table 5.2).

Taking the same approach with cortical sections from human subjects with AD, basal and plaque-associated GFAP fluorescence were detected at increased levels, matching the data from monkeys (Fig.5.4D). In the vicinity of amyloid plaques, the presence activated astrocytes resolved at 56 μm from the plaque edge. A greater variability in plaque-associated astrocyte activation was observed in human cortex, with heterogeneity among individuals within this analysis. Specifically, some individuals displaying high baseline GFAP reactivity exhibited lower plaque-associated reactivity (Fig.S5.1A), indicative of a failure to activate in the plaque zone. Amyloid plaque load was the greatest in human tissue, and regions of the highest amyloid density displayed little plaque-associated astrocyte activation (Fig.S5.1B). These data demonstrate that astrocyte number, structure, and reactivity in transgenic mice is not equivalent to primates. Moreover, age and heterogeneity among individuals appears to be major factor contributing to astrogliosis that is not recapitulated by the mouse model.

Evidence for increased basal and plaque-associated inflammation in the aged primate brain

Having established differences in extent and location of astrocyte reactivity between species, we next evaluated the status of microglia using double immunofluorescent detection of beta amyloid and the microglial marker Iba1. Activation status can be inferred from microglial morphology[52]. Poised, but not activated microglia are ramified in shape with long branched processes and

a small cell body. In contrast, activated microglia are amoeboid and can be identified by large somas and attenuated process length. Although similar numbers of total microglia were detected in the cortical sections from mice and monkeys, microglial morphology was strikingly different between species. Monkeys displayed more heterogeneity in microglial structure, including poly-nucleated somas and more heterogeneity in cell size, matching reports of human microglial diversity[53]. In both mice and monkeys and enrichment of non-ramified microglia was identified in the immediate vicinity of amyloid plaques (Fig.5.5A-B). In mice, the activated microglial were limited to a small area directly surrounding the plaque (Fig 5.5A). In monkeys, a greater zone of microglial activation was detected. Unlike the uniform pattern of microglial recruitment and activation in mice, variability in microglial recruitment and morphology was evident both within each plaque and between plaques of the same individual (Fig 5.5B). In stratifications moving outward from the amyloid plaque a greater number of non-ramified microglia were observed in monkeys, suggesting amyloid-independent activation (Fig.5.5C). Collectively, these data highlight key differences in cellular composition of the amyloid plaque microenvironment between mice and monkeys. This comparison also demonstrates that there are differences in microglial structure and activation state between species.

DISCUSSION

The data in this study provide evidence for an interaction between age and amyloid pathology in contributing to inflammatory processes linked to neurodegeneration. We report differences in cellular composition, morphology, and metabolism in the immediate vicinity of amyloid plaques. Some features are shared among the three species under investigation but others appear only in the primate models and may explain why mouse AD models do not recapitulate the functional deficits associated with human disease. In this study, we show striking parallels in the localized impact of amyloid between the monkey model and the human disease.

The data presented here are consistent with a role for mitochondria in the neuritic plaque environment. Mitochondria were enriched in the immediate vicinity of amyloid plaques in APP/PSEN1 mice, monkeys, and human AD cortex. Elevated cytochrome c oxidase activity was detected in this population of mitochondria in mice, suggesting that that retain maximal activity; however, it is unclear how these mitochondria function *in-vivo.* Mitochondrial biogenesis could represent a compensatory response in dystrophic neurites to amyloid toxicity. Conversely, the clustered mitochondria could be maladaptive and contribute to elevated oxidative stress and metabolic insufficiency. The phenotype we describe is distinct from prior reports showing that mitochondrial dysfunction is a major feature of AD pathology. The "mitochondrial cascade hypothesis" has been proposed, which suggests that bioenergetic deficiency mediates AD neurotoxicity[46]. Mitochondria from AD neurons exhibit respiratory chain deficiencies, and beta amyloid has been shown to directly impair mitochondrial metabolism. Furthermore, mtDNA-depleted neuronal cell lines populated with mitochondria from AD patients display lower ATP production, respiratory chain function, and PGC1a expression, suggesting a primary deficiency of metabolism in AD[54]. The biology behind this clustering of mitochondria in the immediate area of the plaque, observed in mice, monkeys, and in humans, has yet to be defined.

A unique fluorescent signature was detected by MPLSM that appears to co-localize with the clustered mitochondria and the amyloid plaques themselves. This signature was conserved between all three species and is characterized by elevated fluorescence intensity and a mean fluorescence lifetime that was lower than the surrounding tissue. The observation of this same signature in monkey and human arterioles impacted by cerebral amyloid angiopathy (CAA) suggest that fibrillary beta amyloid at least partially responsible for this autofluorescence (data not shown); however, mitochondrial NADH also produces strong fluorescence at near-infrared excitation. The use of a genetically encoded NADH/NAD^+ biosensor with cellular resolution has been reported in brain slices[55]; such a probe would be useful in differentiating between plaque fluorescence and NADH *in-situ*.

Intraneuronal lipofuscin is striking feature of age that was captured in our study. Lipofuscin has been reported to increase with age in humans where it is speculated to represent dysfunctional autophagy in aged neurons[51,56]. Accumulation of lipofuscin has been implicated in the pathology of neurodegenerative diseases such as age-related macular degeneration[57], and involvement of lipofuscin in AD has recently been speculated[58]. Consistent with age-related accumulation, large intraneuronal deposits of lipofuscin were observed in monkey and human cortex, and were much smaller in young APP/PSEN1 mice. The data reported here suggest that lipofuscin accumulation begins early in life and that the size of the particles rather than the number of particles increase with age. The autofluorescent signature of these lipofuscin particles was similar between species, where they displayed high intensity relative to plaques and the surrounding cortex, and a short fluorescence lifetime. This similarity suggests at least some overlap in the biochemical composition of these deposits; however, differing biochemical properties of lipofuscins have been reported in cortical tissue over the course of aging[56]. Co-localization of intraneuronal beta amyloid with lipofuscin has also been reported in AD neurons[59]. In this study, we observed a trend towards increased lipofuscin particle number and size in the immediate vicinity of plaques. This same region displays an increase in VDAC fluorescence intensity in all three species, suggesting that perhaps neuritic mitochondria are physically associated with some lipofuscin deposits. Unfortunately, immunofluorescence of VDAC in brains from human AD subjects was confounded by co-localization with lipofuscin around plaques. It is tempting to speculate that plaque-associated lipofuscin accumulation is partially a result of mitochondrial autophagy in this region.

The activation of astrocytes and microglia surrounding neuritic plaques has been extensively documented in both animal models and postmortem AD brain[12]. The data presented here show that astrocytes in the aged monkey brain are more numerous, larger in size, and display greater number of processes than their young mouse counterparts. The response of astrocytes to amyloid plaques also differed between species. Immunofluorescent staining of GFAP showed

that plaque-associated astrocyte reactivity impacted a greater area in monkeys and humans than in mice. It is still unclear whether these differences in GFAP immunoreactivity are the result of differences in age or due to differences among species. As previously mentioned, GFAP expression increases with age in both rodents and primates[32]; however, astrocytes are also more densely populated in the primate cortex[16]. Higher astrocyte density could contribute to enhanced sensitivity to beta amyloid, perhaps resulting in a more robust state of activation. The large size and sophisticated morphologies of primate astrocytes may also relate to the area impacted by activation. It appears that astrocytes in the aged brain are more sensitized to activation, although little is known about how astrocytes age in either the rodent or human brain.

Accumulating evidence points to a central role for microglia in AD risk and severity[20]. In this study, the number of activated microglia surrounding plaques was similar between mice and monkeys. Microglial morphology and distribution in mice was uniform around each plaque and limited to the immediate plaque vicinity. Previous studies in APP/PSEN1 mice have demonstrated that this constitutes an acute-phase response of healthy microglia which form a protective barrier around plaques, limiting plaque expansion and neurotoxicity[60]. The uniformity of the microglial barrier in mice of this study is consistent with barrier formation. The same was not true in monkeys, where microglia surrounding plaques adopted a spectrum of morphologies. These microglia were often polynucleated and were variable in size and ramification. The morphological diversity of the amyloid-proximal microglial population in monkeys may correspond to subpopulations that differ in activation state. Alternatively, the heterogeneity of microglia in the monkey brain could represent dystrophy and senescence of the plaque-associated population. Similar abnormalities in microglial structure have been reported in post-mortem AD brains[53]. Unfortunately, lipofuscin autofluorescence confounded microglial immunostaining in the human cortex this study, but greater numbers of amoeboid microglia were observed in stratifications further away from plaques in monkeys, suggesting amyloid-independent activation. The data presented here are consistent

with microglial priming in monkeys as a function of age, although species dependent differences cannot be ruled out.

The clinical definition of AD covers a spectrum of individuals with differing risk factors, rates of progression, and co-morbitities such as vascular disease or cerebral amyloid angiopathy (CAA). Perhaps most striking in this study was the heterogeneity among individual monkeys and humans in the extent of glial reactivity and amyloid plaque load. Astrocytes in particular displayed a high degree of variance. Some individuals had very low baseline GFAP expression with robust activation of astrocytes around neuritic plaques. In contrast, other individuals displayed high basal GFAP expression and comparatively low plaque-associated reactivity. In a few of the human specimens, the superficial cortical layers were almost completely inundated with mildly ThS-reactive plaques. Astrocytes in these regions retained their territorial domains and displayed uniform reactivity that was not associated with individual plaques. Monkeys and mice did not exhibit amyloid density to this extent; however, vascular amyloid accumulation was observed to varying degrees in individual monkeys. One individual displayed vascular amyloid accumulation almost exclusively, and developed small perivascular amyloid deposits (data not shown). Astrocytes were only mildly reactive to amyloid deposits in this animal. Isolated plaques in deeper cortical layers and in individuals with lower amyloid plaque load tended to exhibit more robust activation of surrounding astrocytes. Amyloid density, along with the rate of amyloidogenesis likely has a unique influence on astrocyte activation. APP/PSEN1 mice develop significant amyloid plaque loads within a few months, while the same process requires years in monkeys and humans[45,61]. GFAP immunoreactivity was used in this study as an index of astrocyte activation; however, this is not a binary state and represents a continuum of phenotypes that are context-dependent. Hypertrophic astrocytes with different profiles of marker expression have been observed surrounding plaques and in plaque-free areas of the human AD brain[62]. Accumulating evidence suggests that mild astrogliosis can be beneficial in protecting neuronal health, while chronic, unresolved astrogliosis can

result in detrimental effects such as glial scar formation[63]. These results suggest that the trajectories of amyloidosis and glial reactivity differ between individual monkeys and humans, reflecting the complexity of the disease and the important role that brain aging has on disease pathogenesis.

Although there is likely a species component to these differences in the amyloid plaque microenvironment reported here, it seems likely that the age of the animals in sporadic plaque development is a significant contributor. Most AD mouse models are early-onset with a rapid emergence of pathology that is transgenically driven. The data presented here suggest that the development of a late-onset AD mouse model with a later emergence of AD pathology could be more physiologically relevant to LOAD. This strategy, however, would not overcome species differences in microglial status and reactivity. Given the clear parallels in the local impact of amyloid plaques between monkeys and humans we suggest that interventions that are successful in monkeys are likely to translate to the human disease and clinical efficacy.

METHODS

Animals

Mice

Male C57BL/6J (APP/PSEN1) mice (n=6) were obtained from Jackson Laboratories at 4 months of age (Bar Harbor, ME, USA) and housed under controlled pathogen-free conditions in accordance with the recommendations of the University of Wisconsin Institutional Animal Care and Use Committee. Mice were fed 87 kcal week of control diet (F05312, Bio-Serv, Flemington, NJ, USA) and were individually housed with ad libitum access to water. Mice were euthanized at 6 months of age. Brains were isolated, bisected, embedded in OCT, frozen in liquid nitrogen, and stored at −80°C until further processing.

Rhesus Macaques

Male and female rhesus monkeys (n=5) between 29 and 35 years of age (average age = 31.1 years at necropsy) were included in this study. The animals were part of the Aging and Caloric Restriction longitudinal study conducted at the Wisconsin National Primate Research Center. Details of housing and husbandry have been previously decribed[40,64]. Upon death, brains were harvested, sectioned according to a standard necropsy protocol, fixed overnight in 10% neutral-buffered formalin, and paraffin-embedded.

Histochemistry and Immunodetection

For APP/PSEN1 mouse and AD cortical tissue, serial cryostat sections 10 μm in thickness were cut at -15°C with a Leica Cryostat (Fisher Supply, Waltham, MA, USA), defrosted and air dried, and used for histological staining. For rhesus cortical tissue, serial microtome sections 5 μm in thickness were cut with a Leica Microtome (Fisher Supply) and sections were deparaffinized prior to histological staining. Cytochrome c oxidase activity staining was performed on mouse sections as previously decribed[65]. For immunodetection, sections were defrosted and air dried, fixed for 15 minutes in 10% neutral buffered formalin, permeabilized, and blocked for 30 minutes in Superblock buffer containing 0.3% Triton-X. Tissue sections were incubated with primary antibodies overnight at 4°C in a humidified slide chamber. Thioflavin S staining was performed subsequent to immunostaining by incubating slides in 0.02% aqueous Thioflavin S solution, followed by clearing in 50% ethanol for 5 minutes. Antibodies and reagents used are as follows: AlexaFluor 488 anti-rabbit or mouse IgG, AlexaFluor 594 anti-rabbit or mouse IgG (Invitrogen), biotinylated anti-mouse or rabbit IgG (Vector Labs, Burlingame, CA, USA), peroxidase-labeled avidin biotin complex (ABC) solution (Vector labs), ImmPACT NovaRED reagent (Vector Labs), GFAP (ab7260; Abcam), Iba1 (019-19741; Wako), VDAC (ab154856; Abcam), beta-amyloid (NBP2-13075; Novus Biologicals), Thioflavin S (T1892; Sigma-Aldrich).

Image Capture and Analysis

Slides were imaged with a Leica (Buffalo Grove, IL, USA) DM4000B microscope and photographed with a Retiga 4000R digital camera (QImaging Systems, Surrey, BC, Canada). Camera settings were optimized for each stain; for uniformity, all images for a give stain were taken on the same day with identical settings, fixed light levels, and fixed shutter speed optimized at each magnification. Digital images were converted to grayscale prior to image analysis and image analysis was performed using FIJI software[66]. Analysis of GFAP and VDAC fluorescence in the vicinity of plaques was performed as follows: Plaque ROIs were manually created based on Thioflavin S or beta-amyloid immunofluorescence. Stratifications of set distances from the edge of the plaque were defined out to 40 μm or 60 μm using the ROI manager. Prior to stain quantification, a uniform intensity threshold was applied to eliminate fluorescence equivalent to unstained areas of the slide. The same threshold was applied to all images from the same imaging session. To preserve differences in fluorescence intensity within each image, no background subtraction was applied. Baseline fluorescence intensity of each target was defined by the fluorescence intensity at 60 μm from the edge of each plaque. Plaques with overlapping ROIs were included in the analysis. For analysis of microglia, plaque ROIs were generated using anti-beta amyloid immunostaining. Three stratifications of 20 μm intervals were defined and microglia within each stratification were manually counted. Non-ramified microglia were identified by soma enlargement and retraction of processes.

Multiphoton laser scanning microscopy

One day prior to multiphoton imaging, cryostat or deparaffinized sections were dried onto glass coverslips and mounted using Cytoseal 80 mounting solution (Richard Allen). The instrument response function of the optical system was calibrated before each imaging session and sections were imaged at 20x magnification. Data were collected using an excitation wavelength of 740 nm, and emission was filtered at 457 ± 50 nm, the spectral peak for NADH/NADPH. The data collection

time was 240 s using a pixel frame size of 256 × 256. The system has multiple detectors including a 16 channel combined spectral lifetime detector (utilizes a Hamamatsu PML-16 PMT), detection range 350 to 720 nm, and a H7422P GaAsP photon counting PMT (Hamamatsu) for intensity and lifetime imaging. Acquisition was performed with WiscScan, a LOCI developed acquisition package software. Autofluorescence intensity and fluorescence lifetime data were analyzed in SPCImage (Becker & Hickl, v.3.9.7, Berlin, Germany) where a Levenberg–Marquardt routine for nonlinear fitting was used to fit the fluorescence decay curve collected for each pixel in the 256 × 256 frame to a model multi-exponential decay function. Data were assessed by the minimized chi-square value generated during the fit so that analysis was unbiased. To eliminate background fluorescence a threshold for analysis was applied based on photon counts. Additionally, pixels were assigned a bin of 3 for optimal fitting of the data. Autofluorescence intensity data were analyzed using FIJI (NIH, Wayne Rasband; https://imagej.nih.gov/ij/). ROIs for amyloid plaques lipofuscin particles were defined based on autofluorescence intensity and used for subsequent analysis.

Statistical Analysis

Mean stain intensity for GFAP, VDAC, and cytochrome c oxidase activity assays was quantified in each stratification from the plaque and normalized to “baseline” stain intensity at 60 μm from the plaque edge. Means were pooled between images and samples, and multiple t-tests were performed to test whether mean stain intensity at each stratification was different from zero (baseline). Statistical analysis for differences in GFAP and VDAC stain intensity between species was performed using linear mixed models (LMM) to account for the dependency among plaque measurements per animal. The LMMs include full factorial with Type 3 tests of the main effect of species within each stratification in addition to individual comparisons between species. For quantification of activated microglia, individual students’ t-tests were performed on each stratification from the

edge of plaques using pooled averages of samples within each species. Lipofuscin particles detected using MPLSM were defined based on autofluorescence intensity and quantified in FIJI. Mean values for lipofuscin particle size and number were averaged between samples within each species and evaluated using an ANOVA with post hoc analyses.

REFERENCES

1 Association, A. s. 2019 Alzheimer's disease facts and figures. *Alzheimer's & Dementia* **15**, 321-387, doi:10.1016/j.jalz.2019.01.010 (2019).

2 Harman, D. Alzheimer's disease pathogenesis: role of aging. *Ann N Y Acad Sci* **1067**, 454-460, doi:10.1196/annals.1354.065 (2006).

3 Sherrington, R. *et al.* Cloning of a gene bearing missense mutations in early-onset familial Alzheimer's disease. *Nature* **375**, 754-760, doi:10.1038/375754a0 (1995).

4 Levy-Lahad, E. *et al.* A familial Alzheimer's disease locus on chromosome 1. *Science* **269**, 970-973, doi:10.1126/science.7638621 (1995).

5 Scheuner, D. *et al.* Secreted amyloid beta-protein similar to that in the senile plaques of Alzheimer's disease is increased in vivo by the presenilin 1 and 2 and APP mutations linked to familial Alzheimer's disease. *Nat Med* **2**, 864-870, doi:10.1038/nm0896-864 (1996).

6 Karch, C. M. & Goate, A. M. Alzheimer's disease risk genes and mechanisms of disease pathogenesis. *Biol Psychiatry* **77**, 43-51, doi:10.1016/j.biopsych.2014.05.006 (2015).

7 Whitmer, R. A. *et al.* Central obesity and increased risk of dementia more than three decades later. *Neurology* **71**, 1057-1064, doi:10.1212/01.wnl.0000306313.89165.ef (2008).

8 Brown, B. M., Peiffer, J. J. & Martins, R. N. Multiple effects of physical activity on molecular and cognitive signs of brain aging: can exercise slow neurodegeneration and delay Alzheimer's disease? *Mol Psychiatry* **18**, 864-874, doi:10.1038/mp.2012.162 (2013).

9 Duff, K. Transgenic mouse models of Alzheimer's disease: phenotype and mechanisms of pathogenesis. *Biochem Soc Symp*, 195-202, doi:10.1042/bss0670195 (2001).

10 Drummond, E. & Wisniewski, T. Alzheimer's Disease: Experimental Models and Reality. *Acta Neuropathol* **133**, 155-175, doi:10.1007/s00401-016-1662-x (2017).

11 Kimelberg, H. K. & Nedergaard, M. in *Neurotherapeutics* Vol. 7 338-353 (2010).

12 De Strooper, B. & Karran, E. The Cellular Phase of Alzheimer's Disease. *Cell* **164**, 603-615, doi:10.1016/j.cell.2015.12.056 (2016).

13 Allaman, I. *et al.* Amyloid-beta aggregates cause alterations of astrocytic metabolic phenotype: impact on neuronal viability. *J Neurosci* **30**, 3326-3338, doi:10.1523/jneurosci.5098-09.2010 (2010).

14 Abeti, R., Abramov, A. Y. & Duchen, M. R. Beta-amyloid activates PARP causing astrocytic metabolic failure and neuronal death. *Brain* **134**, 1658-1672, doi:10.1093/brain/awr104 (2011).

15 Xiao, Q. *et al.* Enhancing astrocytic lysosome biogenesis facilitates Abeta clearance and attenuates amyloid plaque pathogenesis. *J Neurosci* **34**, 9607-9620, doi:10.1523/jneurosci.3788-13.2014 (2014).

16 Vasile, F., Dossi, E. & Rouach, N. Human astrocytes: structure and functions in the healthy brain. *Brain Struct Funct* **222**, 2017-2029, doi:10.1007/s00429-017-1383-5 (2017).

17 Oberheim, N. A. *et al.* in *J Neurosci* Vol. 29 3276-3287 (2009).

18 Han, X. *et al.* Forebrain engraftment by human glial progenitor cells enhances synaptic plasticity and learning in adult mice. *Cell Stem Cell* **12**, 342-353, doi:10.1016/j.stem.2012.12.015 (2013).

19 Butovsky, O. & Weiner, H. L. Microglial signatures and their role in health and disease. *Nat Rev Neurosci* **19**, 622-635, doi:10.1038/s41583-018-0057-5 (2018).

20 Colonna, M. & Butovsky, O. Microglia Function in the Central Nervous System During Health and Neurodegeneration. *Annu Rev Immunol* **35**, 441-468, doi:10.1146/annurev-immunol-051116-052358 (2017).

21 Gratuze, M., Leyns, C. E. G. & Holtzman, D. M. in *Mol Neurodegener* Vol. 13 (2018).

22 Krasemann, S. *et al.* The TREM2-APOE Pathway Drives the Transcriptional Phenotype of Dysfunctional Microglia in Neurodegenerative Diseases. *Immunity* **47**, 566-581.e569, doi:10.1016/j.immuni.2017.08.008 (2017).

23 Li, Q. *et al.* Developmental Heterogeneity of Microglia and Brain Myeloid Cells Revealed by Deep Single-Cell RNA Sequencing. *Neuron* **101**, 207-223.e210, doi:10.1016/j.neuron.2018.12.006 (2019).

24 Mathys, H. *et al.* Temporal Tracking of Microglia Activation in Neurodegeneration at Single-Cell Resolution. *Cell Rep* **21**, 366-380, doi:10.1016/j.celrep.2017.09.039 (2017).

25 Masuda, T. *et al.* Spatial and temporal heterogeneity of mouse and human microglia at single-cell resolution. *Nature* **566**, 388-392, doi:10.1038/s41586-019-0924-x (2019).

26 Qiu, C., Kivipelto, M. & von Strauss, E. Epidemiology of Alzheimer's disease: occurrence, determinants, and strategies toward intervention. *Dialogues Clin Neurosci* **11**, 111-128 (2009).

27 Alexander, G. E. *et al.* Characterizing cognitive aging in humans with links to animal models. *Front Aging Neurosci* **4**, 21, doi:10.3389/fnagi.2012.00021 (2012).

28 Goyal, M. S. *et al.* Loss of brain aerobic glycolysis in normal human aging. *Cell Metab* **26**, 353-360 e353, doi:10.1016/j.cmet.2017.07.010 (2017).

29 Leal, S. L. & Yassa, M. A. Perturbations of neural circuitry in aging, mild cognitive impairment, and Alzheimer's disease. *Ageing Res Rev* **12**, 823-831, doi:10.1016/j.arr.2013.01.006 (2013).

30 Mattson, M. P. & Arumugam, T. V. Hallmarks of Brain Aging: Adaptive and Pathological Modification by Metabolic States. *Cell Metab* **27**, 1176-1199, doi:10.1016/j.cmet.2018.05.011 (2018).

31 Rodriguez-Arellano, J. J., Parpura, V., Zorec, R. & Verkhratsky, A. Astrocytes in physiological aging and Alzheimer's disease. *Neuroscience* **323**, 170-182, doi:10.1016/j.neuroscience.2015.01.007 (2016).

32 Nichols, N. R., Day, J. R., Laping, N. J., Johnson, S. A. & Finch, C. E. GFAP mRNA increases with age in rat and human brain. *Neurobiol Aging* **14**, 421-429, doi:10.1016/0197-4580(93)90100-p (1993).

33 Perry, V. H. & Holmes, C. Microglial priming in neurodegenerative disease. *Nat Rev Neurol* **10**, 217-224, doi:10.1038/nrneurol.2014.38 (2014).

34 Stephan, A. H. *et al.* A dramatic increase of C1q protein in the CNS during normal aging. *J Neurosci* **33**, 13460-13474, doi:10.1523/jneurosci.1333-13.2013 (2013).

35 Dyrks, T., Dyrks, E., Masters, C. L. & Beyreuther, K. Amyloidogenicity of rodent and human beta A4 sequences. *FEBS Lett* **324**, 231-236, doi:10.1016/0014-5793(93)81399-k (1993).

36 Rodrigue, K. M., Kennedy, K. M. & Park, D. C. Beta-amyloid deposition and the aging brain. *Neuropsychol Rev* **19**, 436-450, doi:10.1007/s11065-009-9118-x (2009).

37 Price, D. L. *et al.* Aged non-human primates: an animal model of age-associated neurodegenerative disease. *Brain Pathol* **1**, 287-296 (1991).

38 Mattison, J. A. *et al.* Caloric restriction improves health and survival of rhesus monkeys. *Nat Commun* **8**, 14063, doi:10.1038/ncomms14063 (2017).

39 Colman, R. J. *et al.* Caloric restriction reduces age-related and all-cause mortality in rhesus monkeys. *Nat Commun* **5**, 3557, doi:10.1038/ncomms4557 (2014).

40 Colman, R. J. *et al.* Caloric restriction delays disease onset and mortality in rhesus monkeys. *Science* **325**, 201-204, doi:325/5937/201 [pii] 10.1126/science.1173635 (2009).

41 Balasubramanian, P., Mattison, J. A. & Anderson, R. M. Nutrition, metabolism, and targeting aging in nonhuman primates. *Ageing Res Rev*, doi:10.1016/j.arr.2017.02.002 (2017).

42 Poduri, A. *et al.* Apolipoprotein E4 and beta amyloid in senile plaques and cerebral blood vessels of aged rhesus monkeys. *Am J Pathol* **144**, 1183-1187 (1994).

43 Paspalas, C. D. *et al.* The aged rhesus macaque manifests Braak stage III/IV Alzheimer's-like pathology. *Alzheimers Dement* **14**, 680-691, doi:10.1016/j.jalz.2017.11.005 (2018).

44 Geula, C. *et al.* Aging renders the brain vulnerable to amyloid beta-protein neurotoxicity. *Nat Med* **4**, 827-831, doi:10.1038/nm0798-827 (1998).

45 Sridharan, A. *et al.* Calorie restriction attenuates astrogliosis but not amyloid plaque load in aged rhesus macaques: a preliminary quantitative imaging study. *Brain Res* **1508**, 1-8, doi:10.1016/j.brainres.2013.02.046 (2013).

46 Swerdlow, R. H., Burns, J. M. & Khan, S. M. The Alzheimer's Disease Mitochondrial Cascade Hypothesis: Progress and Perspectives. *Biochim Biophys Acta* **1842**, 1219-1231, doi:10.1016/j.bbadis.2013.09.010 (2014).

47 SC, J. *et al.* The Wisconsin Registry for Alzheimer's Prevention: A review of findings and current directions. *Alzheimer's & dementia (Amsterdam, Netherlands)* **10**, doi:10.1016/j.dadm.2017.11.007 (2017).

48 Keikhosravi, A., Bredfeldt, J. S., Sagar, A. K. & Eliceiri, K. W. Second-harmonic generation imaging of cancer. *Methods Cell Biol* **123**, 531-546, doi:10.1016/b978-0-12-420138-5.00028-8 (2014).

49 Moreno-Garcia, A., Kun, A., Calero, O., Medina, M. & Calero, M. An Overview of the Role of Lipofuscin in Age-Related Neurodegeneration. *Front Neurosci* **12**, 464, doi:10.3389/fnins.2018.00464 (2018).

50 Brunk, U. T. & Terman, A. Lipofuscin: mechanisms of age-related accumulation and influence on cell function. *Free Radic Biol Med* **33**, 611-619, doi:10.1016/s0891-5849(02)00959-0 (2002).

51 Moreira, P. I., Carvalho, C., Zhu, X., Smith, M. A. & Perry, G. Mitochondrial dysfunction is a trigger of Alzheimer's disease pathophysiology. *Biochim Biophys Acta* **1802**, 2-10, doi:10.1016/j.bbadis.2009.10.006 (2010).

52 Davis, E. J., Foster, T. D. & Thomas, W. E. Cellular forms and functions of brain microglia. *Brain Res Bull* **34**, 73-78 (1994).

53 Streit, W. J., Khoshbouei, H. & Bechmann, I. Dystrophic microglia in late-onset Alzheimer's disease. *Glia* **68**, 845-854, doi:10.1002/glia.23782 (2020).

54 Silva, D. F. *et al.* Bioenergetic flux, mitochondrial mass and mitochondrial morphology dynamics in AD and MCI cybrid cell lines. *Hum Mol Genet* **22**, 3931-3946, doi:10.1093/hmg/ddt247 (2013).

55 Mongeon, R., Venkatachalam, V. & Yellen, G. Cytosolic NADH-NAD(+) Redox Visualized in Brain Slices by Two-Photon Fluorescence Lifetime Biosensor Imaging. *Antioxid Redox Signal* **25**, 553-563, doi:10.1089/ars.2015.6593 (2016).

56 Benavides, S. H., Monserrat, A. J., Farina, S. & Porta, E. A. Sequential histochemical studies of neuronal lipofuscin in human cerebral cortex from the first to the ninth decade of life. *Arch Gerontol Geriatr* **34**, 219-231, doi:10.1016/s0167-4943(01)00223-0 (2002).

57 Nowak, J. Z. Age-related macular degeneration (AMD): pathogenesis and therapy. *Pharmacol Rep* **58**, 353-363 (2006).

58 Giaccone, G., Orsi, L., Cupidi, C. & Tagliavini, F. in *Dement Geriatr Cogn Dis Extra* Vol. 1 292-296 (2011).

59 Gomez-Ramos, P. & Asuncion Moran, M. Ultrastructural localization of intraneuronal Abeta-peptide in Alzheimer disease brains. *J Alzheimers Dis* **11**, 53-59, doi:10.3233/jad-2007-11109 (2007).

60 Condello, C., Yuan, P., Schain, A. & Grutzendler, J. Microglia constitute a barrier that prevents neurotoxic protofibrillar Abeta42 hotspots around plaques. *Nat Commun* **6**, 6176, doi:10.1038/ncomms7176 (2015).

61 Reiserer, R. S., Harrison, F. E., Syverud, D. C. & McDonald, M. P. Impaired spatial learning in the APPSwe + PSEN1DeltaE9 bigenic mouse model of Alzheimer's disease. *Genes Brain Behav* **6**, 54-65, doi:10.1111/j.1601-183X.2006.00221.x (2007).

62 Simpson, J. E. *et al.* Astrocyte phenotype in relation to Alzheimer-type pathology in the ageing brain. *Neurobiol Aging* **31**, 578-590, doi:10.1016/j.neurobiolaging.2008.05.015 (2010).
63 Sofroniew, M. V. Molecular dissection of reactive astrogliosis and glial scar formation. *Trends Neurosci* **32**, 638-647, doi:10.1016/j.tins.2009.08.002 (2009).
64 Ramsey, J. J. *et al.* Dietary restriction and aging in rhesus monkeys: the University of Wisconsin study. *Exp Gerontol* **35**, 1131-1149 (2000).
65 Pugh, T. D. *et al.* A shift in energy metabolism anticipates the onset of sarcopenia in rhesus monkeys. *Aging Cell* **12**, 672-681, doi:10.1111/acel.12091 (2013).
66 Schindelin, J. *et al.* Fiji: an open-source platform for biological-image analysis. *Nat Methods* **9**, 676-682, doi:10.1038/nmeth.2019 (2012).

Figure 5.1

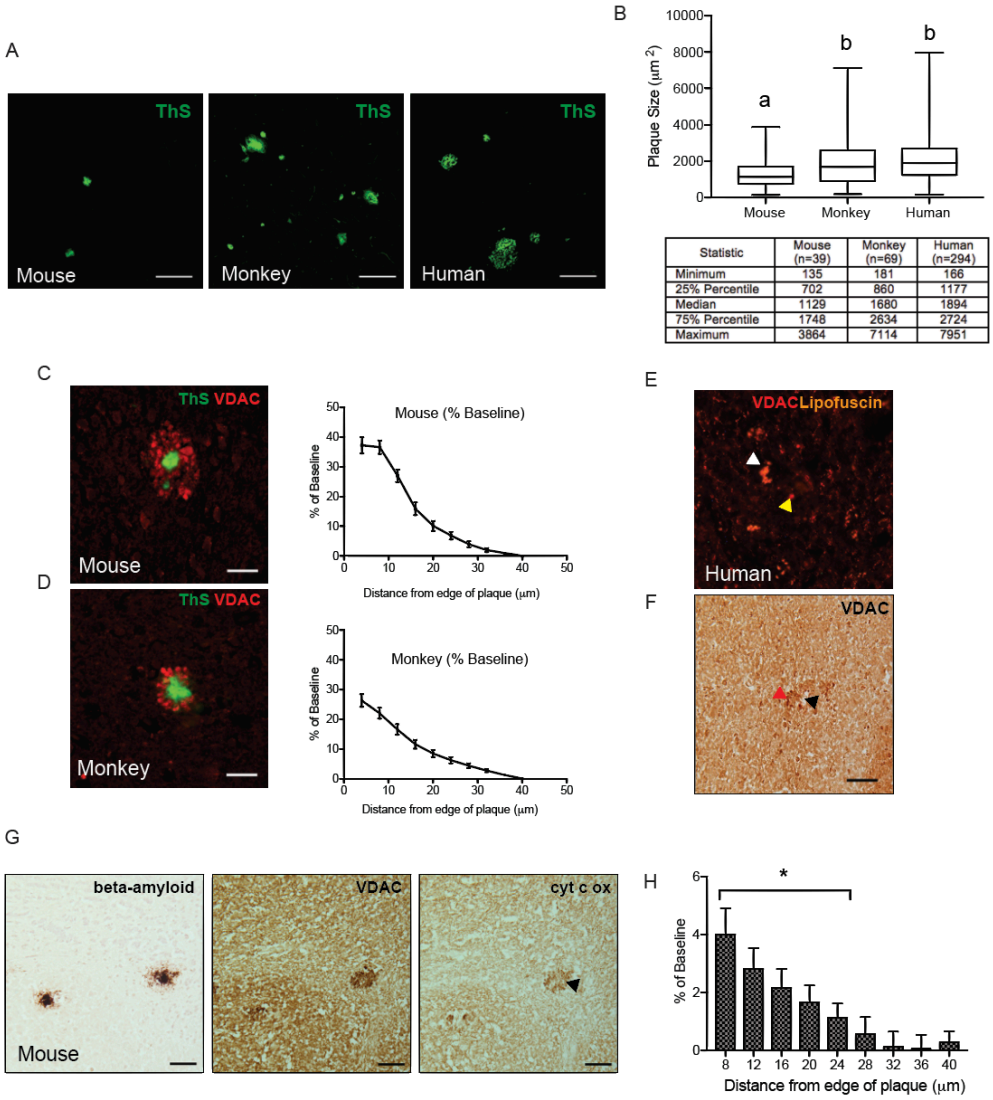

Figure 5.1. Mitochondria accumulate around amyloid plaques. (A) Thioflavin S (ThS) staining of dense-core amyloid plaques in mice, monkey, and human AD cortex. Scale Bar = 40μm. (B) Box and Whisker plots of median plaque size, IQR, and range between species. (C-D) Immunofluorescent labeling of mitochondria (VDAC) and amyloid plaques (ThS) in cortical tissue of (C) mice and (D) rhesus monkeys (40x). (E) Immunofluorescent labeling of mitochondria (red) and autofluorescent lipofuscin (orange) in human AD cortex with respective yellow and white arrows (F) Immunohistochemical detection of mitochondria in human AD cortex. Red arrow corresponds to plaque-associated mitochondria. Black arrow indicates the dense-core of a neuritic plaque. (G) Adjacent cryosections of mouse cortex immunostained for beta-amyloid, VDAC, and cytochrome c oxidase enzyme activity with (H) quantification of cytochrome c oxidase activity in 4μm increments from the edge of amyloid plaques. Scale bar = 20μm.

Mouse (n = 5-6); Monkey (n=5); Human (n=10) biological replicates with [n=28-294 plaque ROIs quantified within species]; data are shown as an average ± SEM; *p < 0.05 Multiple t-tests.

Figure 5.2

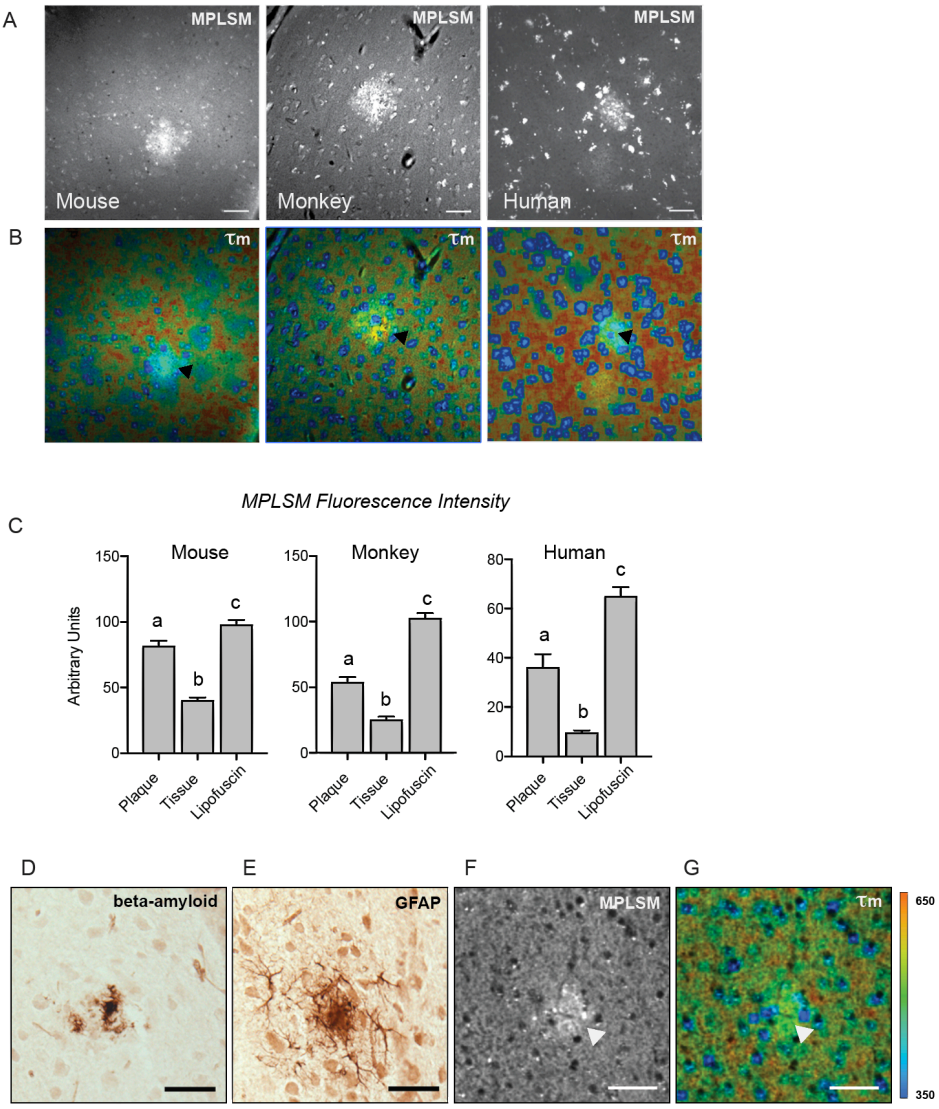

Figure 5.2. Multiphoton imaging confirms plaque-associated localized metabolic disruption. (A) Representative two-photon fluorescence intensity (ex.740nm) images of APP/PSEN1 mouse, monkey, and human AD cortical tissue (20x). Scale bar = 20µm. (B) Corresponding images of mean fluorescence lifetime (τ_m). (C) Two-photon fluorescence intensity of plaques, tissue, and lipofuscin particles between species (D-G) Adjacent cryosections of APP/PSEN1 mouse cortex immunostained for (E) beta-amyloid (F) and GFAP. (G) Fluorescence intensity (ex.740nm) (H) and lifetime τ_m images of a single amyloid plaque. Scale bar = 20µm.

Mouse (n=5); Monkey (n=3); Human (n=5) biological replicates with [n=11-15 plaque ROIs quantified within species] data are shown as an average ± SEM; *p < 0.05 ANOVA

Figure 5.3

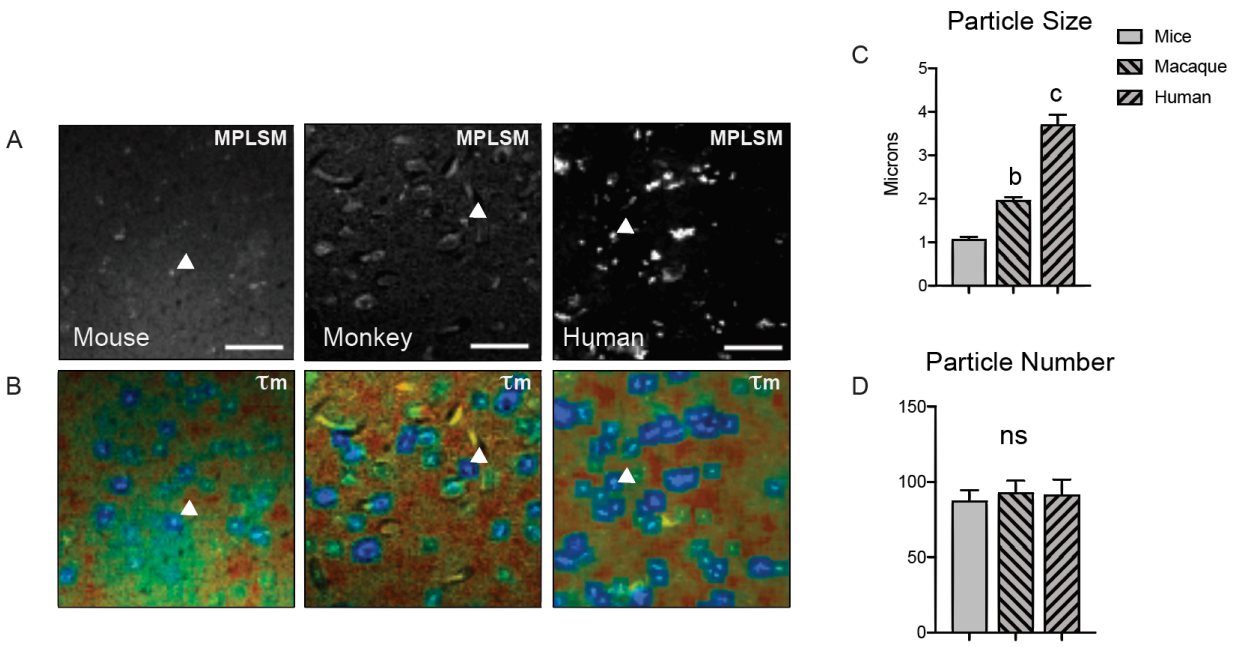

Figure 5.3. Brain tissues taken at older-age carry a greater burden of lipofuscin deposits. (A) Representative two-photon fluorescence intensity (ex.740nm) images of APP/PSEN1 mouse, monkey, and human AD cortical tissue. Scale bar = 10µm. (B) Corresponding images of mean fluorescence lifetime (τ_m). (C) Quantitation of lipofuscin particle (D) size and (E) number between mouse, monkey, and human samples.

Mouse (n=5); Monkey (n=3); Human (n=5) biological replicates with [n=11-15 plaque ROIs quantified within species] data are shown as an average ± SEM; *$p < 0.05$ ANOVA

Figure 5.4

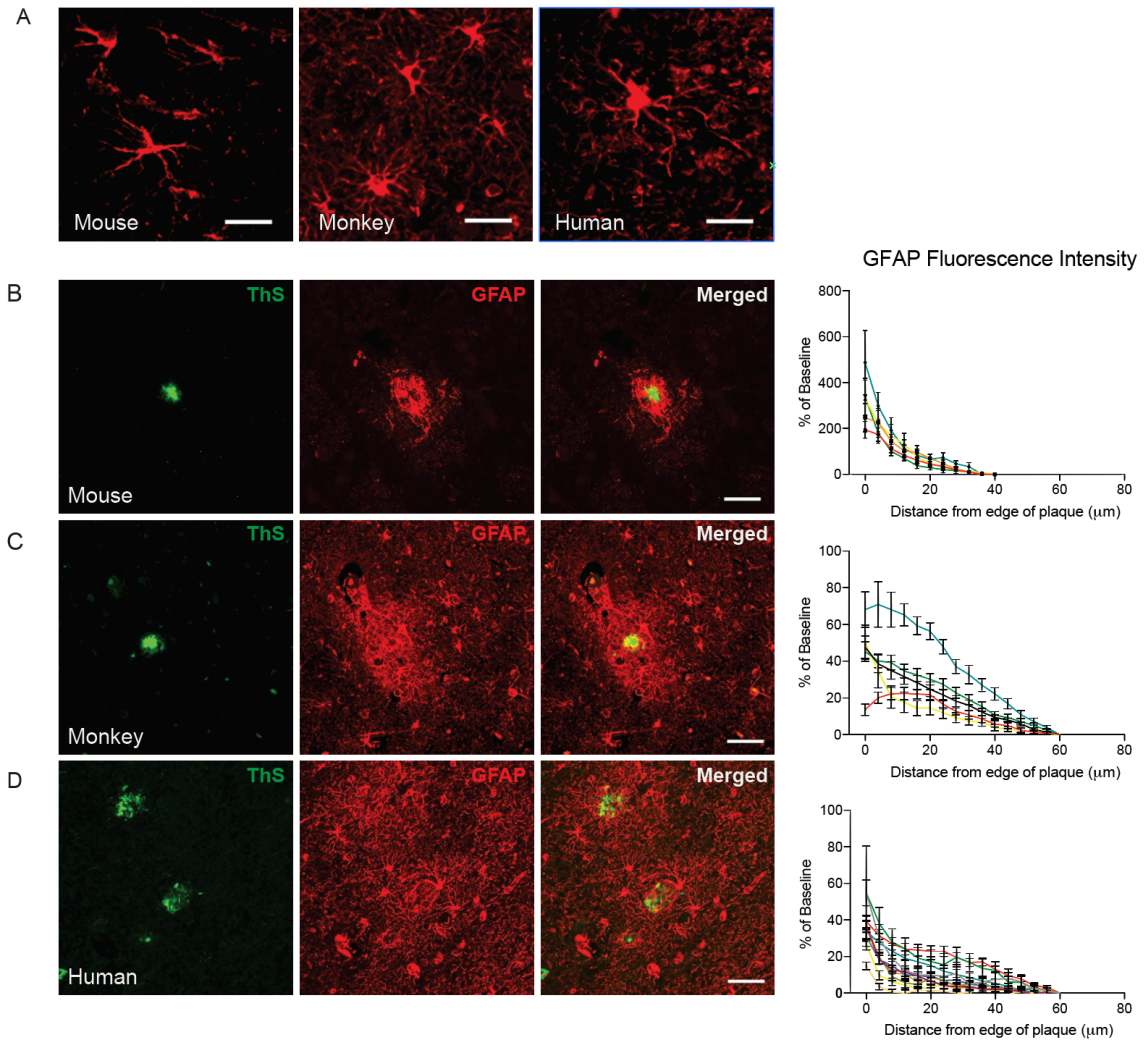

Figure 5.4. Astrogliosis in response to beta-amyloid shows an age-component. (A) Immunofluorescent labeling of astrocytes (GFAP) distal to amyloid plaques in APP/PSEN1 mouse, aged monkey, and human AD cortex (40x). Scale bar = 10µm. (B-D) Immunofluorescent labeling of astrocytes and amyloid plaques (Thioflavin S) in cortical tissue of (B) mice (C) monkeys (D) and AD cortex (20x), with quantification of GFAP fluorescence intensity of individual samples. Scale bar = 40µm.

Mouse (n = 6); Monkey (n=5); Human (n=10) biological replicates with [n=28-210 plaque ROIs quantified within species]; data are shown as an average ± SEM for each individual animal

Figure 5.5

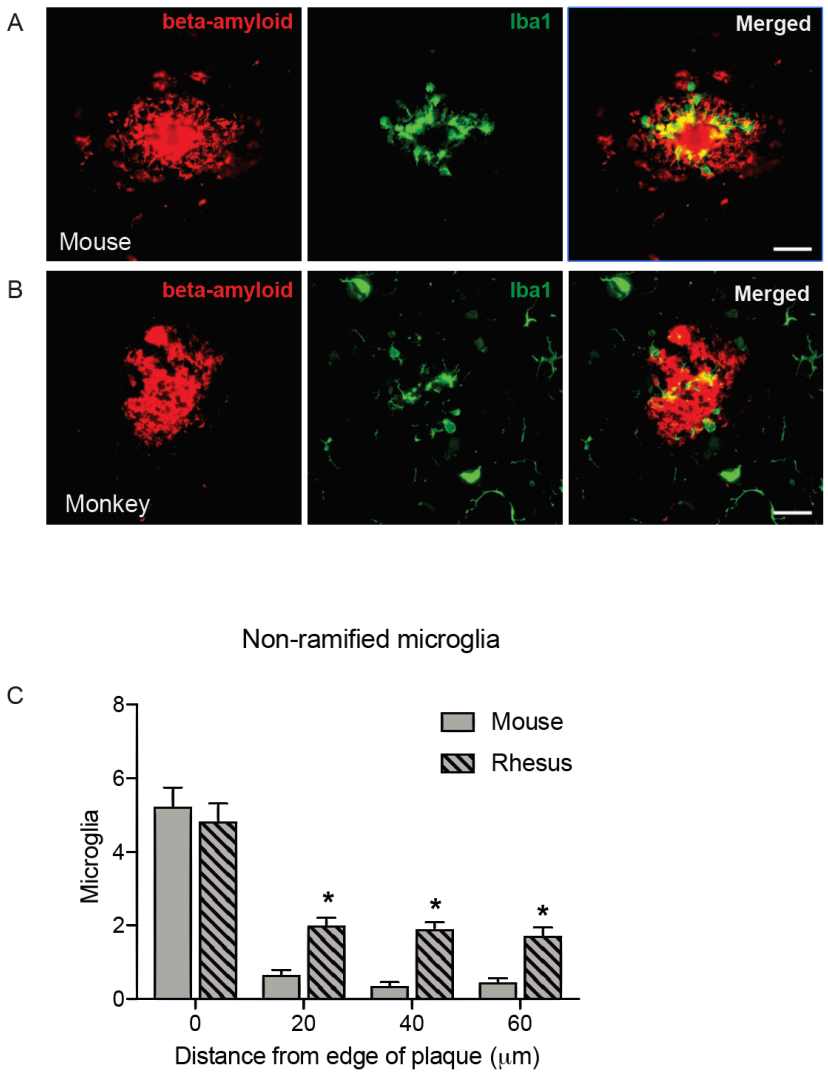

Figure 5.5. Evidence for increased basal and plaque-associated inflammation in the aged primate brain. (A-C) Immunofluorescent labeling of microglia (iba1) and amyloid plaques in cortical tissue of (A) APP/PSEN1 mice (B) aged rhesus monkeys (40x). Scale bar=20µm. (C) Numbers of non-ramified microglia in 20µm stratifications from the edge of amyloid plaques.

Mouse (n = 5-6); Monkey (n=5); Human (n=10) biological replicates with [n=28-294 plaque ROIs quantified within species]; data are shown as an average ± SEM; *p < 0.05 Multiple t-tests.

Figure 5.1S

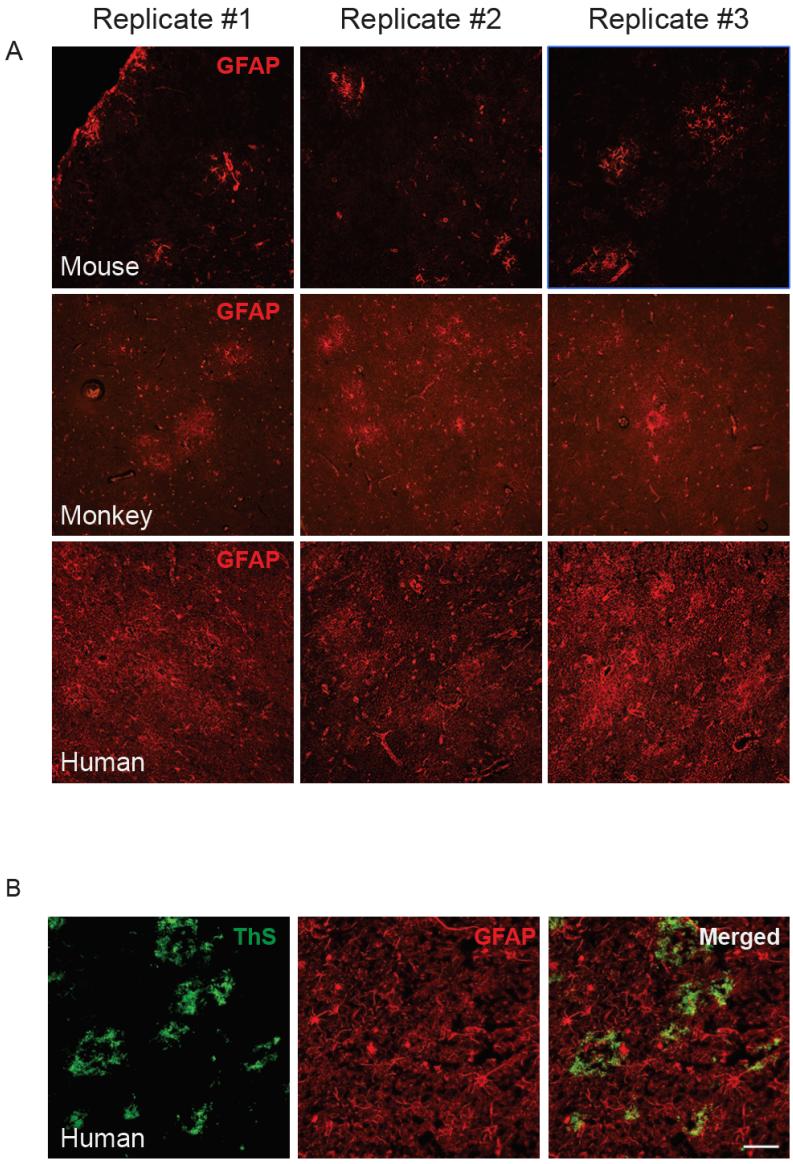

Figure S5.1. Astrocyte quantity and reactivity differs between species. (A) Immunofluorescent labeling of astrocytes (GFAP) in APP/PSEN1 mice, aged rhesus monkeys, and human AD cortex (10x) between three replicates. (B) Immunofluorescent labeling of astrocytes and thioflavin S (ThS) staining of amyloid plaques in superficial cortical layer of human AD brain (20x). Scale bar = 20µm.

Table 5.1

Sample	Sex (M/F)	Age	Sample Region
B6.Cg-Tg(APPswe,PSEN1dE9) (n=6)	M	6 mo	somatosensory cortex
	M	6 mo	
	M	6 mo	
	M	6 mo	
	M	6 mo	
	M	6 mo	
Rhesus Macaque (n=5)	M	30.4	temporal cortex
	M	30	
	M	31.1	
	M	29.3	
	F	34.8	
Human AD (n=10)	M	72	middle temporal gyrus
	M	82	post. middle temporal gyrus
	M	84	middle temporal gyrus
	M	95	middle temporal gyrus
	M	96	middle temporal gyrus
	F	72	middle temporal gyrus
	F	86	middle temporal gyrus
	F	87	post. middle temporal gyrus
	F	95	post. middle temporal gyrus
	F	96	post. middle temporal gyrus

Table 5.2

Distance (μm)	Species	p-value	Distance (μm)	Species	p-value
0	Mouse	***	32	Mouse	**
	Rhesus	***		Rhesus	***
	Human	***		Human	***
4	Mouse	***	36	Mouse	ns
	Rhesus	***		Rhesus	***
	Human	***		Human	***
8	Mouse	***	40	Mouse	ns
	Rhesus	***		Rhesus	***
	Human	***		Human	***
12	Mouse	***	44	Mouse	ns
	Rhesus	***		Rhesus	***
	Human	***		Human	***
16	Mouse	***	48	Mouse	ns
	Rhesus	***		Rhesus	***
	Human	***		Human	***
20	Mouse	***	52	Mouse	ns
	Rhesus	***		Rhesus	***
	Human	***		Human	**
24	Mouse	***	56	Mouse	ns
	Rhesus	***		Rhesus	***
	Human	***		Human	ns
28	Mouse	***	60	Mouse	baseline
	Rhesus	***		Rhesus	
	Human	***		Human	